

Alma Mater Studiorum – Università di Bologna

DOTTORATO DI RICERCA IN

Fisica

Ciclo XXVI

**Settore Concorsuale di afferenza: 02/A1**

**Settore Scientifico disciplinare: FIS/04**

**Search for the MSSM Neutral Higgs Boson  
in the  $\mu^+\mu^-$  final state  
with the CMS experiment at LHC**

**Presentata da: Federica Primavera**

**Coordinatore Dottorato**

**Relatore**

**Prof. Fabio Ortolani**

**Prof. Francesco Luigi Navarra**



# Contents

<b>Introduction</b>	<b>1</b>
<b>1 The SM Higgs and the new physics beyond it</b>	<b>3</b>
1.1 Phenomenology of the Standard Model . . . . .	3
1.2 The Higgs mechanism . . . . .	5
1.3 Theoretical constraints on the Higgs mass . . . . .	9
1.4 The Higgs direct search . . . . .	12
1.4.1 The Higgs at LHC . . . . .	13
1.5 Supersymmetry . . . . .	19
1.5.1 Structure of the MSSM . . . . .	20
<b>2 The CMS Experiment at the LHC</b>	<b>25</b>
2.1 The Large Hadron Collider . . . . .	25
2.1.1 The accelerator . . . . .	27
2.1.2 Luminosity . . . . .	28
2.1.3 LHC operations . . . . .	29
2.1.4 Proton-proton collision at LHC . . . . .	32
2.1.5 The LHC data management . . . . .	33
2.2 The CMS experiment . . . . .	36
2.2.1 CMS Coordinate system . . . . .	38
2.2.2 Inner Tracking System . . . . .	40
2.2.3 The Eletromagnetic Calorimeter . . . . .	43
2.2.4 The Hadronic Calorimeter . . . . .	46
2.2.5 The Muon System . . . . .	48
2.2.6 CMS Trigger System . . . . .	54

<b>3</b>	<b>The CMS software</b>	<b>57</b>
3.1	Event Generation . . . . .	58
3.2	Simulation . . . . .	59
3.3	Reconstruction . . . . .	59
3.3.1	Iterative Tracking reconstruction . . . . .	60
3.3.2	Primary Vertex Reconstruction . . . . .	66
3.3.3	Muon reconstruction . . . . .	70
3.3.4	Jet reconstruction . . . . .	79
3.3.5	Missing Transverse Energy reconstruction . . . . .	83
3.3.6	Particle Flow algorithm . . . . .	83
3.3.7	Link algorithm . . . . .	84
3.3.8	Particle reconstruction and identification . . . . .	85
3.3.9	Particle Flow Jets . . . . .	87
3.3.10	b-tagging Algorithm . . . . .	87
3.3.11	PF Missing Transverse Energy . . . . .	88
<b>4</b>	<b>The MSSM <math>H \rightarrow \mu^+ \mu^-</math> search at CMS</b>	<b>91</b>
4.1	Benchmark scenarios . . . . .	91
4.1.1	The $m_h^{\max}$ scenario . . . . .	92
4.1.2	The $m_h^{\text{mod}}$ scenario . . . . .	94
4.2	Production and decays of the MSSM Neutral Higgs boson at LHC . . . . .	95
<b>5</b>	<b>Event selection</b>	<b>99</b>
5.1	Data and Simulated Samples . . . . .	100
5.2	Event selection . . . . .	104
5.2.1	Trigger on-line selection . . . . .	105
5.2.2	Monte Carlo pile-up re-weighting . . . . .	105
5.2.3	Primary vertex selection . . . . .	106
5.2.4	Selection of $\mu^+ \mu^-$ pairs . . . . .	106
5.2.5	Missing transverse energy selection . . . . .	110
5.2.6	$b$ -jets selection . . . . .	111
5.2.7	Dimuon spectrum . . . . .	114

<b>6</b>	<b>Results</b>	<b>119</b>
6.1	Signal efficiency . . . . .	120
6.2	Systematic uncertainties . . . . .	124
6.3	FeynHiggs calculation of cross sections, masses and widths . . . . .	126
6.4	Fitting procedure . . . . .	127
6.4.1	Signal description . . . . .	128
6.4.2	Background description . . . . .	129
6.4.3	Signal plus background description . . . . .	131
6.4.4	Systematic uncertainty of fit function . . . . .	131
6.5	Limits calculation . . . . .	132
6.5.1	Combined results within the $m_h^{\max}$ scenario . . . . .	135
6.5.2	Combined results within $m_h^{\text{mod}}$ scenarios . . . . .	138
6.6	Checks on the fit procedure . . . . .	138
6.7	Comparison with published results . . . . .	144
	<b>Conclusions</b>	<b>147</b>



# Introduction

The Standard Model (SM) of particle physics is a theory aimed to describe the elementary constituents of matter and their interactions. The theory has been soundly confirmed by a variety of direct and indirect measurements performed by several experiments, like those performed at Large Electron-Positron collider (LEP), Stanford Linear Collider (SLC), Tevatron and recently at Large Hadron Collider (LHC). The recent discovery of the last missing piece of the SM, the Higgs boson, announced at CERN on 4th of July 2012, completes the model prediction to give mass to the elementary particles.

Anyway many theoretical limitations of the SM let physicists think that a more fundamental theory should exist. In fact search for new phenomena beyond the SM constitutes the main goals of the experiments at LHC.

Supersymmetry is one of the most attractive theories beyond the Standard Model. It foresees the existence of many new particles, and it introduces a larger Higgs sector with respect to the one of the SM. In its minimal formulation, the Minimal Supersymmetric Standard Model (MSSM) extension, five Higgs bosons are required: two neutral scalar particles  $h$  and  $H$ , one neutral pseudo-scalar  $A$  and two charged particles  $H^\pm$ . The MSSM is still described by a large number of free parameters, but only a subset of them affects the Higgs sector. This allows experimental searches to be performed within well defined scenarios described only by a restricted number of free parameters.

In this thesis, my work in the Compact Muon Solenoid (CMS) experiment on the search for the neutral MSSM Higgs bosons decaying into two muons is presented. The search is performed on the full data collected by CMS in proton-proton collisions at the LHC. The MSSM free parameter space is explored within the most conservative benchmark scenario,  $m_h^{max}$ , and within its modified versions,  $m_h^{mod+}$  and  $m_h^{mod-}$ .

The MSSM neutral Higgs boson production at the LHC mainly occurs via gluon-gluon fusion and  $b\bar{b}$ -associated processes. The dimuon final state is characterized by a very clean signature, and it is not so difficult to separate it from the background, exploiting the CMS high efficiency on muon identification. Unfortunately the branching ratio of the Higgs into two muons is very small. So to study this channel it is needed to keep the maximum number of events along the selection steps. This is achieved performing an events categorization based on the presence or the absence of a jet coming from b-quark, which enhances the sensitivity in case of b-associated production and gluon fusion respectively. Furthermore this channel benefits of the full reconstruction of the final states. This allows to define the Higgs mass with higher precision than what is achievable in the other available channels, such as the  $b\bar{b}$  and  $\tau\tau$ , especially thanks to the good muon momentum resolution of CMS.

All the steps of this search are discussed in details in next chapters, where the first three are meant to give a theoretical and technical description, while the following three contains the description of the work done.

In the first chapter the SM and the physics beyond it is introduced in order to focus on the theoretical aspects which underlie this search. The second chapter is dedicated to a general description of the experimental apparatus, comprising the LHC accelerator and the CMS experiment. A third chapter is dedicated to the CMS software used to reconstruct the data coming from LHC collisions, and to generate the simulated-samples according to the theoretical expectations.

The fourth chapter starts describing the MSSM benchmark scenarios within which the search is performed, in order to give a complete picture of the expected signal and background. The fifth chapter is dedicated to the event selection, and explains all the steps from initial samples to the final dimuon invariant mass distributions. The sixth chapter is dedicated to the statistical treatment of the data, and reports the results of the search.

# Chapter 1

## The Higgs boson in the Standard Model and the new physics beyond it

During the last decades, the experiments in particle physics proceeded to verify the Standard Model (SM) expectations. The SM is a theory which well describes the phenomenology of fundamental constituents of matter and their interactions. The recent discovery of a resonance with a mass of approximately 125 GeV, compatible with the SM Higgs boson, completes the puzzle as described by SM, that however leaves many unanswered questions in the survey on the structure of the universe. This chapter provides a theoretical introduction to the SM and its open questions. The description of one of the extensions of the theory candidate to answer to some of these questions, the Minimal Supersymmetric Standard Model (MSSM), completes the chapter.

### 1.1 Phenomenology of the Standard Model

The Standard Model is a Lorentz invariant renormalisable quantum field theory which combines the Quantum Chromo Dynamics (QCD) with the Glashow-Salam-Weinberg electroweak theory. It is a Gauge theory where the particles are mathematically described as fields and classified according to their spin  $S$  into: fermions, with half-integer spin that are properly the matter particles, and bosons, with integer spins, that are the mediators of the interactions. The SM does not include the gravitational interaction, which is not described by a quantum field

## 1. The SM Higgs and the new physics beyond it

---

theory, and is also negligible in the description of phenomena between elementary particles at the energy scale achieved so far.

This Gauge theory is based on the free Dirac Lagrangian:

$$\mathcal{L} = \bar{\Psi}(i\gamma^\mu\partial_\mu - m)\Psi \quad (1.1)$$

that describes the evolution of non-interacting particles:  $\Psi$  is the field with mass  $m$  that evolves according to the  $i\gamma^\mu\partial_\mu$  term. The eq. 1.1 is invariant for a group of *global* transformations. In order to maintain the same invariance also under *local* transformations we need to mathematically introduce the so called Gauge fields, that physically are the particles that mediate the interactions.

In this sense the SM is a  $SU(3)_C \times SU(2)_L \times U(1)_Y$  theory, where the electroweak interaction comes from the local invariance under the  $SU(2)_L \times U(1)_Y$  transformations, while the strong interaction comes from the local invariance under the  $SU(3)_C$  transformations.

The Gauge fields introduced in the first case are the vector bosons  $W_\nu^a$  ( $a = 1, 2, 3$ ) for  $SU(2)_L$  and  $B_\mu$  for  $U(1)_Y$ . They are not physical state because they do not have a diagonal mass matrix, but from their linear combination we can obtain the physical bosons known as  $W^+$ ,  $W^-$  and  $Z^0$  for the weak interaction, and  $\gamma$  for the electromagnetic one. In the same way for the strong interaction the eight gluons are obtained by an appropriate linear combination of the  $SU(3)_C$  Gauge bosons.

Concerning the fermions, they are divided into quarks and leptons. The latter are subject only to electroweak interaction, while the quarks are subject also to the color force.

The quarks are six, have a fractional electric charge<sup>1</sup>  $Q$ , and are classified according to the flavour quantum number as: up ( $u$ ), charm ( $c$ ), top ( $t$ ) with  $Q = +\frac{2}{3}|e|$ , and down ( $d$ ), strange ( $s$ ), bottom ( $b$ ) with  $Q = -\frac{1}{3}|e|$ . They are the only fermions with a color quantum number: blue, red and green. These are the charges of the strong interaction, and are observable only as neutral color combinations named *hadrons*. This is known as the *color confinement* and it is equivalent to say that in nature free quarks do not exist. There are two kinds of hadrons, or in other words two ways to achieve the color neutrality: the *mesons* composed by a quark and an antiquark which carry opposite sign of the same

---

<sup>1</sup>with respect to the electron charge, taken as unity

color, and the *barions* composed by a triplet where each quark has a different color. An exception is the *t* quark, with a too short lifetime to make a bound state.

Also the leptons are six:  $e, \mu, \tau$  carry electric charge and have both electromagnetic and weak interactions, while  $\nu_e, \nu_\mu, \nu_\tau$  are neutral and are only sensitive to the weak interaction.

Corresponding to every fermion, there is an associated anti-fermion with the same mass and spin, but opposite electric charge, and, in case of the quarks, also with opposite colour charge.

For the fermions the baryon and lepton quantum numbers are also defined. The quarks have leptonic number  $L=0$ , but they carry baryonic number  $B = \frac{1}{3}$ , the antiquarks  $B = -\frac{1}{3}$ . As consequence the baryons have  $B = 1$ , while the mesons  $B = 0$ . The leptons, on the contrary, have  $L = 1$ , the antileptons  $L = -1$ , whereas for them  $B=0$ . In addition to the lepton number, lepton family numbers are also defined,  $L_e, L_\mu$  and  $L_\tau$ , with the same assigning scheme: +1 for particles of the corresponding family, -1 for the antiparticles, and 0 for leptons of other families or non-leptonic particles.

Leptons and quarks can be grouped in generations, each containing two quarks, one with electric charge  $+\frac{2}{3}|e|$  and the other with electric charge  $-\frac{1}{3}|e|$ , and two leptons, one charged and the other neutral. The generations observed so far are three, differing only in mass that progressively grows from the first to the third generation. Ordinary matter is formed only by the constituents of the first generation:  $u, d, e, \nu_e$ .

Within the SM there are 61 fundamental particles: 24 fermions and respectively 24 antifermions, 12 vector boson and just one scalar boson, the Higgs boson.

## 1.2 The Higgs mechanism

Until recently one of the most important open questions of the Standard Model was the origin of mass of the fundamental particles. The SM Lagrangian, as written in eq. (1.2) below, summarises in an elegant formalism the dynamic of the fundamental constituents and their interactions, but it does not predict the mass of the fermions and the bosons. This has been for many years the most important missing aspect of the SM theory.

## 1. The SM Higgs and the new physics beyond it

---

A Gauge theory does not contain the mass terms of the bosons. The SM is a Gauge theory invariant under  $SU(3)_C \times SU(2)_L \times U(1)_Y$  symmetry group. Its most general form involving these fields is:

$$\begin{aligned} \mathcal{L} = & -\frac{1}{4}G_{\mu\nu}^\alpha G^{\alpha\mu\nu} - \frac{1}{4}W^{\alpha\mu\nu}G_{\mu\nu}^\alpha - \frac{1}{4}B_{\mu\nu}B^{\mu\nu} \\ & - \frac{1}{2}\bar{L}_m\gamma^\mu D_\mu L_m - \frac{1}{2}\bar{E}_m\gamma^\mu D_\mu E_m - \frac{1}{2}\bar{Q}_m\gamma^\mu D_\mu Q_m \\ & - \frac{1}{2}\bar{D}_m\gamma^\mu D_\mu D_m - \frac{1}{2}\bar{U}_m\gamma^\mu D_\mu U_m, \end{aligned} \quad (1.2)$$

where:

- $Q, L, E, U, D$  are the leptons and hadrons for each family order (the index  $m$  runs over the three families of fermions);
- $G_\mu^\alpha$  with  $\alpha = 1, \dots, 8$  represents the gluons fields coming from the invariance under  $SU(3)_C$ ;
- $W_\mu^\alpha$  with  $\alpha = 1, 2, 3$  are the fields coming from the invariance under  $SU(2)_L$ ;
- and  $B_\mu$  is the field coming from the invariance under  $U(1)_Y$ .

The quantum number related to these transformations are respectively colour, isospin and hypercharge.

The covariant derivative is:

$$D_\mu = \partial_\mu - ig_1 Y B_\mu - ig_2 \frac{\tau^\alpha}{2} W_\mu^\alpha - ig_3 \frac{\lambda^b}{2} G_\mu^b, \quad (1.3)$$

where  $g_{1,2,3}$ , and  $Y, \tau, \lambda$  are the coupling strengths and the operators in the time-space of the electromagnetic, weak and strong force respectively.

This Lagrangian well describes the interactions of matter and radiation, but it does not include any mass term for the introduced bosons, while the fermions mass are put by hand, as written in the (1.1). These terms should have a form:  $m_f \bar{\Psi}\Psi$ ,  $m_B^2 B_\mu B^\mu$ ,  $m_W^2 W_\mu W^\mu$  and  $m_G^2 G_\mu G^\mu$ .

The presence of mass terms would break the  $SU(3)_C \times SU(2)_L \times U(1)_Y$  symmetry and would violate the Gauge invariance of the Lagrangian. According to experimental observations, while the gluons are massless and the  $SU(3)_C$  Gauge invariance of the strong interaction can be conserved, the Z and W bosons are

massive. So the symmetry  $SU(2)_L \times U(1)_Y$ , which describes the unified electroweak interaction has to be broken to give mass to the  $Z$  and  $W$  bosons. This is known as the mechanism of Spontaneous Symmetry Breaking (SSB). The same mechanism also introduces the masses of quarks and charged leptons.

The term “spontaneous” means that the symmetry is not explicitly broken by the interaction, as it is done introducing the interacting terms in the free Dirac’s Lagrangian (eq. 1.1). In this case a new artificial field is introduced in the theory and the symmetry is broken by its state of lowest energy, referred as the vacuum of the quantum field theory.

The simplest way to implement the SSB in the electroweak theory is achieved by adding a single complex scalar doublet with four degrees of freedom, called the Higgs field:

$$\varphi = \begin{pmatrix} \varphi^+ \\ \varphi^0 \end{pmatrix}. \quad (1.4)$$

This adds to the Lagrangian the term  $\mathcal{L}_{SSB}$ :

$$\mathcal{L}_{SSB} = (\mathcal{D}_\mu \varphi)^\dagger (\mathcal{D}^\mu \varphi) - V(\varphi^\dagger \varphi), \quad (1.5)$$

where the covariant derivative must be

$$\mathcal{D}_\mu = \partial_\mu - ig^2 \frac{\tau^{(i)}}{2} W_\mu^{(i)} - ig^1 B_\mu, \quad (1.6)$$

and the potential that breaks the symmetry is

$$V = -\mu^2 \varphi^\dagger \varphi + \lambda (\varphi^\dagger \varphi)^2. \quad (1.7)$$

The symmetry is broken because the minimum of this potential is not a single value but a degenerate spectrum of values (fig. 1.1):

$$\langle \varphi^\dagger \varphi \rangle_0 = \mu^2 / \lambda. \quad (1.8)$$

Choosing as vacuum expectation value

$$\langle \varphi \rangle_0 = \frac{1}{\sqrt{2}} \begin{pmatrix} 0 \\ v \end{pmatrix}, \quad (1.9)$$

with  $v = \mu / \sqrt{\lambda}$ , we break both the  $SU(2)_L$  and the  $U(1)_Y$ , preserving the  $U(1)_{EM}$  symmetry of the electric charge operator.

## 1. The SM Higgs and the new physics beyond it

---

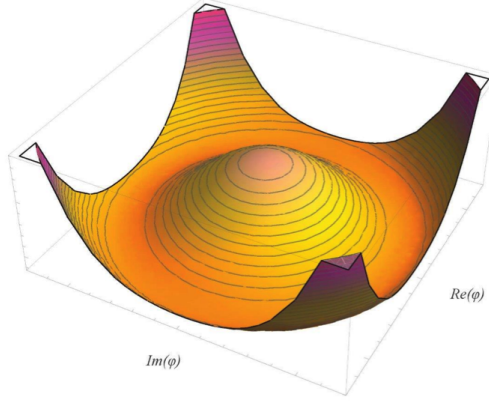


Figure 1.1: *Illustration of the Higgs potential that gives rise to spontaneous symmetry breaking. The Higgs potential is symmetric with a local maximum in the centre. The energy state in the centre is symmetric, however it is an excited state and therefore unstable. Because of the form of the potential, the stable final state at the minimum, the vacuum state, is not symmetric any more and it breaks the symmetry.*

Now we manage a re-parametrization of the four degree of freedom of the field  $\varphi$  in terms of one scalar boson  $H$  and three Goldstone boson  $\xi^{(i)}$  ( $i = 1,2,3$ )

$$\varphi = \exp \frac{i\sigma^{(i)} \xi^{(i)}}{2} \frac{1}{\sqrt{2}} \begin{pmatrix} 0 \\ v + H \end{pmatrix}. \quad (1.10)$$

Exploiting the Gauge invariance we make a unitary transformation, named unitary-Gauge (U-Gauge):

$$\varphi \rightarrow \varphi' = \exp^{-\frac{i\sigma^{(i)} \xi^{(i)}}{2}} \varphi = \frac{1}{\sqrt{2}} \begin{pmatrix} 0 \\ v + H \end{pmatrix}. \quad (1.11)$$

As a consequence the three massless Goldstone bosons disappear and a single massive scalar boson remains. The latter is called Higgs boson and has mass  $m_H = \sqrt{2}\mu$ .

Now the (1.2) contains the mass terms for the Gauge fields  $W_\mu^\alpha$  and  $B_\mu$ . To give rise to the mass of the fermions we have to introduce a further term in the Lagrangian. It is called Yukawa term and it describes the coupling between the

Higgs and the fermions:

$$\mathcal{L}_{Yukawa} = -G_e(\bar{R}(\Psi^\dagger L) + (\bar{L}\Psi)R). \quad (1.12)$$

With this term, where  $\Psi$  represents a generic fermion field, after applying the reparametrization as in the (1.10) and the U-Gauge (1.11), the  $\mathcal{L}_{SSB}$  contains the mass terms of the fermions, quadratic in the fermion fields, and the coupling terms to the Higgs:

$$\mathcal{L}_{Yukawa} = -\frac{v+H}{\sqrt{2}}(f_m\bar{E}_mE^m + g_m\bar{U}_mU^m + h_m\bar{D}_mD^m), \quad (1.13)$$

where  $E, U, D$  are again the leptons and hadrons for each family order (the index  $m$  runs over the three families of fermions). It is worth noticing that there is one independent Yukawa coupling parameter  $f_n$  for every mass,  $m_n$ . The conclusion is that the heavier the particle, the stronger the coupling to the Higgs boson. Therefore the Higgs prefers to decay into the heaviest kinematically allowed particles pair.

### 1.3 Theoretical constraints on the Higgs mass

In the SM, the Higgs boson mass is given by

$$m_H = \sqrt{\frac{\lambda}{2}}v, \quad (1.14)$$

where  $\lambda$  is the Higgs self-coupling parameter and  $v$  is the vacuum expectation value of the Higgs field. The Fermi coupling  $G_F = \frac{\sqrt{2}}{2v}$  is determined with precision of 0.6 ppm from muon decay measurements and it determines the value  $v = 246$  GeV. Since  $\lambda$  is unknown, the value of the SM Higgs boson mass  $m_H$  cannot be predicted.

The first theoretical constraint to the Higgs boson mass comes from the requirements of partial-wave unitarity of the longitudinal gauge boson scattering at tree-level [1]. A way to see this is to consider the  $W_L^+W_L^- \rightarrow W_L^+W_L^-$  case. The s-partial wave of this scattering amplitude can be written as:

$$\alpha_0(W_L^+W_L^- \rightarrow W_L^+W_L^-) = \frac{-G_F m_H^2}{8\pi\sqrt{2}} \left[ 2 + \frac{m_H^2}{s - m_H^2} - \frac{m_H^2}{s} \ln \left( 1 + \frac{s}{m_H^2} \right) \right], \quad (1.15)$$

## 1. The SM Higgs and the new physics beyond it

---

where  $\sqrt{s}$  is the center of mass energy. The unitarity condition for this reaction is:

$$|\alpha_0(W_L^+W_L^- \rightarrow W_L^+W_L^-)| \leq 1. \quad (1.16)$$

At the high energy limit where  $s \gg m_H^2$  the  $\alpha_0$  amplitude approaches the constant

$$\alpha_0(W_L^+W_L^- \rightarrow W_L^+W_L^-) \rightarrow \frac{-G_F m_H^2}{4\pi\sqrt{2}}. \quad (1.17)$$

Consequently, in order for the tree approximation to respect the unitarity bound at high energies, the Higgs boson mass must satisfy:

$$m_H^2 \leq \frac{4\pi\sqrt{2}}{G_F}. \quad (1.18)$$

If we consider the requirements of partial waves unitarity on the system of four scattering channels  $W_L^+W_L^-$ ,  $Z_L Z_L$ ,  $HH$  and  $HZ_L$ , then a  $4 \times 4$  matrix  $t_0$  is formed:

$$t_0 \rightarrow \frac{-G_F m_H^2}{4\pi\sqrt{2}} \begin{bmatrix} 1 & \frac{1}{\sqrt{8}} & \frac{1}{\sqrt{8}} & 0 \\ \frac{1}{\sqrt{8}} & \frac{3}{4} & \frac{1}{4} & 0 \\ \frac{1}{\sqrt{8}} & \frac{1}{4} & \frac{3}{4} & 0 \\ 0 & 0 & 0 & \frac{1}{2} \end{bmatrix}. \quad (1.19)$$

The most stringent unitary bound is derived from the requirement that the magnitude of the largest eigenvalue has to be less than one. The Higgs mass in this case has to satisfy:

$$m_H^2 \leq \frac{8\pi\sqrt{2}}{3G_F} \simeq (1\text{TeV}/c^2)^2. \quad (1.20)$$

Besides the upper bound on the Higgs boson mass from unitarity constraints, additional theoretical arguments place approximate upper and lower bounds on  $m_H$  [2, 3]. An upper bound comes from the perturbativity of the theory up to the scale  $\Lambda$ , at which the SM breaks down, and a lower bound derived from the stability of the Higgs potential (Fig.1.3). The masses of all fermions are a consequence of the SSB at electroweak energy scale, since the SM Higgs doublet is postulated to couple to the fermions through Yukawa interactions. However the validity of the SM as an effective theory describing physics up to the Planck scale is questionable, because of the following *naturalness* argument. All fermion masses and dimensionless couplings are logarithmically sensitive to the scale  $\Lambda$  at which new

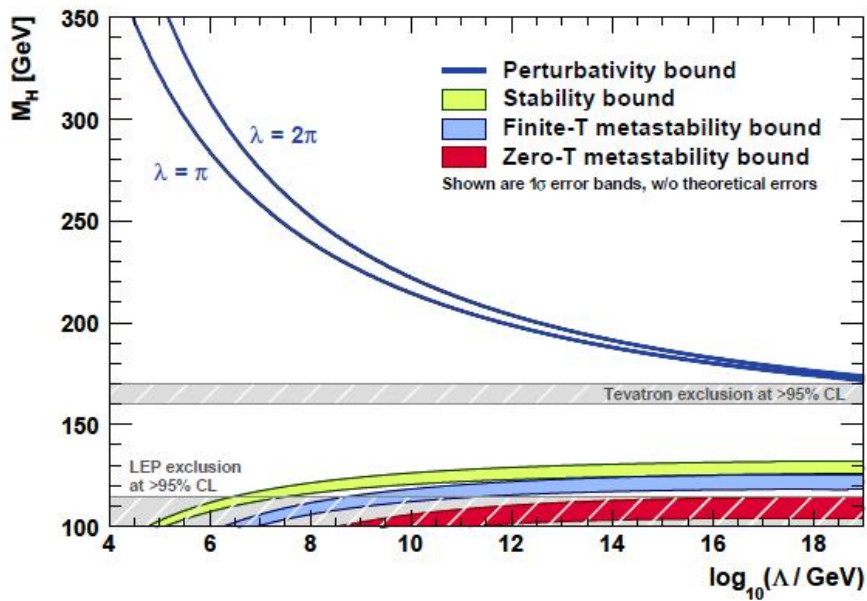


Figure 1.2: *Plots of the Higgs mass close to the LEP lower limit as a function of the energy scale of processes. The green area shows the lower bound and it is not a narrow line because of uncertainties in the calculation. The blue and red areas are more stringent bounds below which metastability occurs. At high Higgs masses, instead, two different blue lines mark the fuzzy boundary of the region where perturbative calculations are enabled or prevented by the size of the Higgs boson self-coupling. In grey the direct search limits are also shown.*

## 1. The SM Higgs and the new physics beyond it

---

physics becomes relevant. On the other hand scalar squared masses are quadratically sensitive to  $\Lambda$ . The observable SM Higgs mass has the following form:

$$m_H^2 = m_{H_0}^2 + \frac{k g^2 \Lambda^2}{16\pi^2}, \quad (1.21)$$

where  $m_{H_0}$  is a fundamental parameter of the theory. The second term is a one-loop correction in which  $g$  is the electroweak coupling and  $k$  is a constant, that is calculable within the low-energy effective theory. The two contributions arise from independent sources and one would not expect the observable Higgs boson mass to be significantly smaller than either of the two terms.

Hence, if the scale of new physics  $\Lambda$  is much larger than the electroweak scale, unnatural cancellations must occur to remove the quadratic dependence of the Higgs boson mass on this large energy scale.

If the Higgs boson mass  $m_H$  is below 180 GeV, all fields remain weakly interacting up to the Planck scale.

In addition, if  $m_H$  is too large, then according to the (1.14) the Higgs self-coupling,  $\lambda$ , diverges at some scale  $\Lambda$  below the Planck scale. A Higgs boson mass of the order of the electroweak scale is required from unitarity constraints and preferred by precision measurements of electroweak observables.

Most relevantly, recent results from direct Higgs searches at the LHC observes a SM Higgs boson with a mass of  $125.9 \pm 0.4$  GeV [4], in excellent agreement with the indirect predictions from electroweak precision data. Thus, the SM is expected to be embedded in a more fundamental theory which will stabilize the hierarchy between the electroweak scale and the Planck scale in a natural way.

### 1.4 The Higgs direct search

The SM theory does not predict a specific mass for the Higgs boson, however the properties of the Higgs boson and the techniques to detect it depend strongly on its mass.

Below  $m_H = 600$  GeV, previous direct Higgs searches at the Large Electron Positron collider (LEP), the Tevatron and the Large Hadron Collider (LHC) were unable to exclude mass regions between 114 and 130 GeV [5, 6, 7].

The amount of data produced in the LHC collisions up to December 2011 let the two main experiments, CMS and ATLAS (A Toroidal LHC Apparatus), to

report an excess of events near a mass of 125 GeV [8, 9]. Afterwards also at the Tevatron, CDF and D0 collaborations reported an excess of events in the range from 120 to 135 GeV [10]. After half a year of data taking, in July 2012, with more statistic accumulated at LHC, CMS and ATLAS announced the discovery of a new boson with a mass of 125 GeV, and, during the following months, a much larger statistics allows to conclude that it is consistent with the expectation for a SM Higgs boson [11].

### 1.4.1 The Higgs at LHC

In a proton-proton accelerator as LHC, characterised by a very large QCD background, the relevance of Higgs production processes are evaluated not only according to the size of the production cross section, but also according to the significance (signal over squared root of background) that can be obtained. It means that some production processes, even with a large cross section, could not be suitable to obtain a sufficient significance for some decay channels.

According to their production rate the main processes are ordered as: the gluon fusion (gg), the vector boson fusion (VBF) originating from  $qq$  or  $q\bar{q}$  collision, the Higgs boson production in association with a vector boson  $W^\pm H$  or  $ZH$  or with a top-quark pair  $t\bar{t}H$ . Their Feynmann diagrams are shown in figure 1.3, while their dependence with respect to the Higgs mass is shown in figure 1.4.

Concerning the Higgs decays, its branching fraction into the different decay channels strongly depends on its mass, as shown in figure (1.5). A light Higgs  $m_{H0} < 150 \text{ GeV}/c^2$  mainly decays in the  $b\bar{b}$  pair and, to a lesser extent, in  $\tau^+\tau^-$ ,  $\gamma\gamma$  and  $\mu^+\mu^-$ . At higher Higgs masses the cross section of these processes rapidly decreases while decays in  $W^+W^-$  and  $ZZ$  become dominant.

The SM Higgs decay modes mainly studied at LHC are  $H \rightarrow \gamma\gamma$ ,  $H \rightarrow ZZ$ ,  $H \rightarrow W^+W^-$ ,  $H \rightarrow \tau^+\tau^-$  and  $H \rightarrow b\bar{b}$ , and their branching ratio is shown in figure 1.5. The first three processes are of comparable sensitivity in the search for a Higgs boson with a mass around 125 GeV and are more sensitive than the  $b\bar{b}$  and  $\tau^+\tau^-$ . In particular the  $\gamma\gamma$  and  $ZZ$ , provide precise measurements of the parent particle mass. Both are defined the Higgs golden channels because of clear signature of final state and a relatively low background.

In the case  $H \rightarrow \gamma\gamma$ , even if the BR of SM Higgs into two photons is only

## 1. The SM Higgs and the new physics beyond it

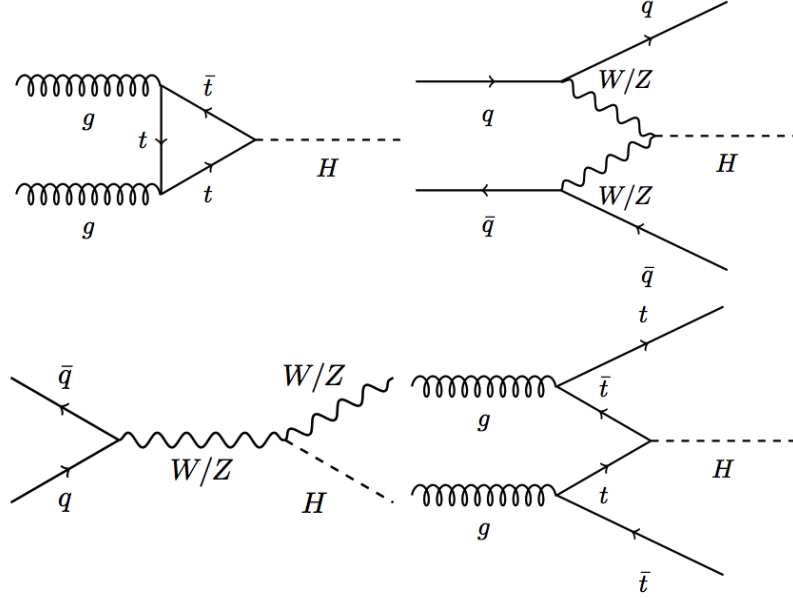


Figure 1.3: *Higgs production processes at LHC: gluon fusion  $gg \rightarrow H$  (top left), vector boson fusion  $qq \rightarrow H$  or  $q\bar{q} \rightarrow H$  (top right), associated production a vector boson  $q\bar{q} \rightarrow W^\pm H$  or  $ZH$  (bottom left) or with a top-quark pair  $gg \rightarrow t\bar{t}H$  (bottom right).*

about 0.3%, both photons can be measured very accurately by electromagnetic calorimeters and the background can be precisely estimated.

The other golden channel at LHC is the  $H \rightarrow ZZ$ , where each  $Z$  decays in electron or muon pairs. The branching ratio  $\text{BR}(H \rightarrow ZZ)$  is about one order of magnitude larger than  $\text{BR}(H \rightarrow \gamma\gamma)$  for  $m_{H0} \simeq 125 \text{ GeV}$ . Since  $m_{Z0} = 91 \text{ GeV}$ , at least one of the  $Z$  bosons has to be off mass shell. The  $Z$  decays into lepton or quark pairs but the final states of electron and/or muons pairs are considered because of the smaller QCD background. There are several SM processes (not including Higgs boson decays) that can lead to the same final states. They include direct  $ZZ$  production from quark-antiquark annihilation and gluon-gluon fusion, as well as processes involving a single  $Z$  boson produced with an associated heavy-quark jet and top-antitop pair-production. Apart from the rate of direct  $ZZ$  production, which we can determine accurately from simulation, the rates of

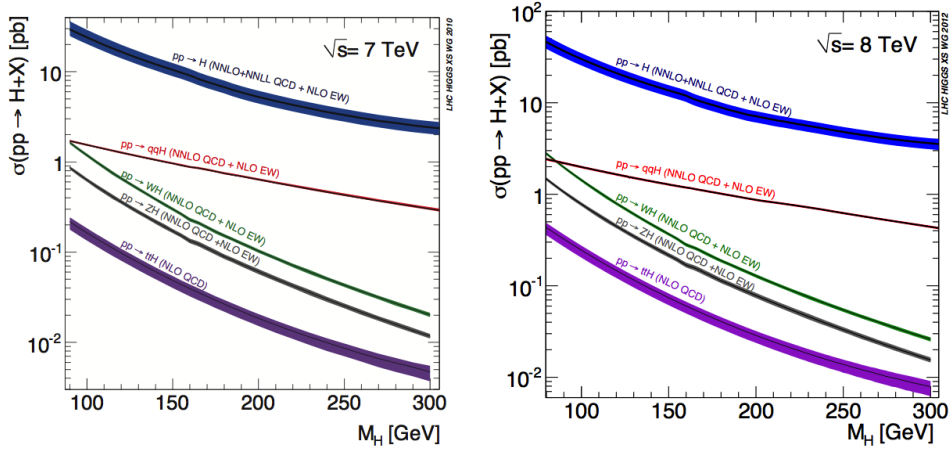


Figure 1.4: *Standard Model Higgs boson production cross sections at centre of mass energy 7 TeV (left) and 8 TeV (right). Source: [12].*

other backgrounds are extracted from data. So the strength of this channel at ATLAS and in particular at CMS is that the invariant mass of the  $ZZ$  system can be measured with good accuracy exploiting the four-lepton momenta, reconstructed with percent precision. The presence of a Higgs boson in the data should manifest itself as a peak in the  $ZZ$  invariant mass spectrum in the presence of a small continuum background.

The existence of a SM Higgs boson has been confirmed by ATLAS and CMS, and the discovery has first occurred in the two golden channels.

Figure 1.6(a) shows the di-photon invariant mass spectrum from data collected by CMS during 2011 and 2012, where an excess was observed at 125 GeV on an otherwise smoothly falling background spectrum. The reconstructed invariant mass in figure 1.6(b) shows the  $Z$  mass peak at 91 GeV resulting from decays of a  $Z$  boson into two leptons and an energetic virtual photon that materializes through a second dilepton pair. This peak, near 125 GeV, is in the same region as that found in the diphoton decay mode 1.6(b). The observed excess is consistent in shape and size with that expected for diphoton and  $ZZ$  decays of SM Higgs boson [13, 14].

Apart from the  $\gamma\gamma$  and  $ZZ$ , that now are not only the golden but the discovery channels for the SM Higgs, other relevant decay channels at LHC are studied

## 1. The SM Higgs and the new physics beyond it

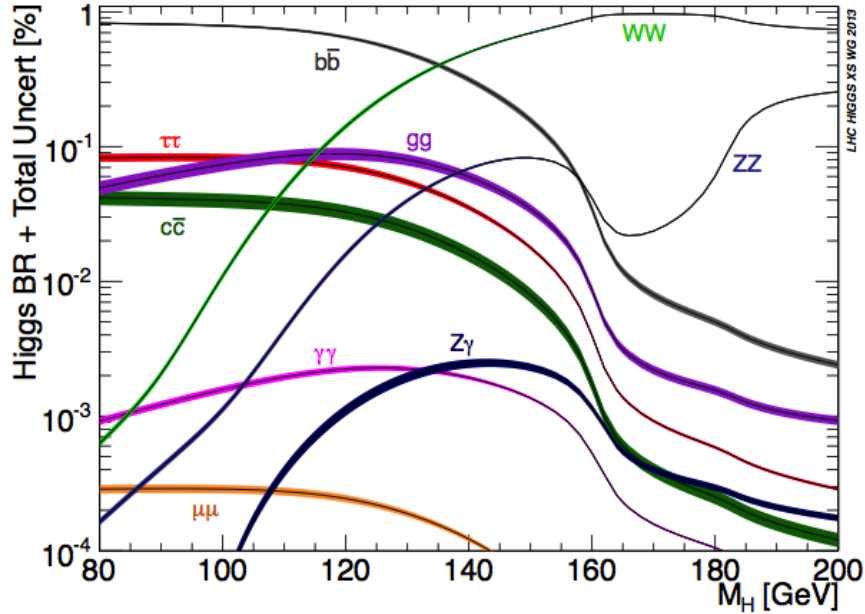


Figure 1.5: *Standard Model Higgs boson decay branching ratios and total width.*  
 Source: [12].

mainly to investigate the Higgs properties. One of them is the decay into two W bosons. This final state must contain two opposite-sign leptons (either electrons or muons) and significant missing transverse momentum, resulting from the undetected neutrinos from W decays. It implies that the invariant mass of the two W bosons cannot be precisely reconstructed. In fact the results of this analysis (fig. 1.7) show a broad excess of events over the expected background and not a narrow peak, consistent with the presence of a new particle at a mass near 125 GeV.

It is also explored whether this new particle decays into fermion pairs, as it would be expected to if the associated field gives mass to the fermions in addition to the W and Z bosons, by looking for instance where the particle decays into heavy fermions. The heaviest fermions into which a light SM Higgs boson can decay are the  $\tau$  leptons and the b quarks.

The detection of  $\tau$  leptons is challenging because they are unstable and decay less than 1ps after production, either into a lighter charged lepton (electron

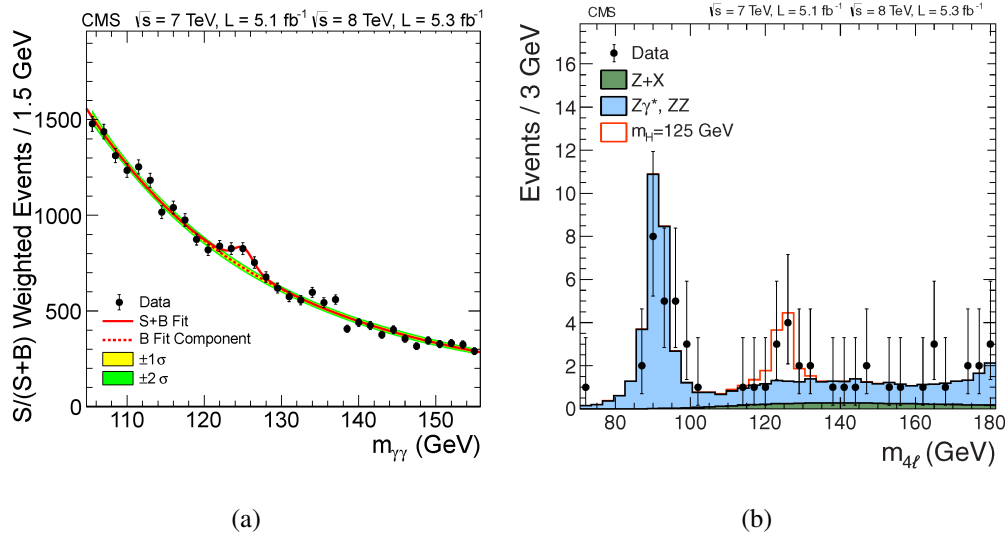


Figure 1.6: *Distributions of the reconstructed invariant Higgs mass. The plot (1.6(a)) shows the diphoton invariant mass distribution. The lines represent the fitted background and signal, and the coloured bands represent the  $\pm 1$  and  $\pm 2$  standard deviation uncertainties in the background estimate. The plot (1.6(b)) shows the four-lepton invariant mass for the  $H \rightarrow ZZ \rightarrow 4l$  analysis: the points represent the data, the filled histograms represent the background, and the open histogram shows the signal expectation for a Higgs boson of mass  $m_H = 125$  GeV, added to the background expectation.*

or muon) and neutrinos or into a neutrino and either one or three charged pions, possibly accompanied by neutral pions. As in the case of the WW decay mode, the presence of neutrinos in the decay products prevents a full event reconstruction, and, instead of a resonance peak, a broad enhancement over background is expected. We have not yet found such an enhancement (fig.1.7b), but the current sensitivity to this channel does not exclude the presence of the SM Higgs boson.

The SM Higgs boson is expected to be strongly coupled to the b quarks. In fact at low mass (below about 135 GeV), the decay in  $b\bar{b}$  pair has the largest BR of the five search modes reported above. This signal is, however, overwhelmed by a large background from SM b quark production, making the search less sensitive. To have a more favourable signal-to-background ratio, we searched for this signal in the (rarer) associated production process involving a W or Z boson, which can

## 1. The SM Higgs and the new physics beyond it

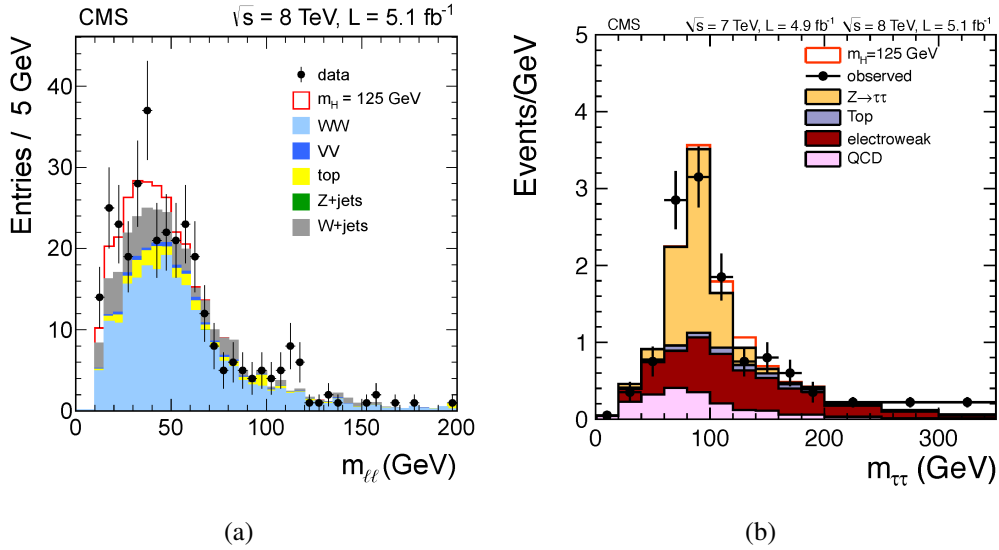


Figure 1.7: Distribution of  $m_{ll}$  for the  $H \rightarrow W^+W^-$  search at 8 TeV 1.7(a). The points are the data while the coloured histograms represent each component of the background. The signal expected from a Higgs boson with a mass  $m_H = 125$  GeV is shown in the open red histogram added to the background. Distribution of  $m_{\tau\tau}$  in the combined 7 and 8 TeV data sets for the VBF category of the  $H \rightarrow \tau\tau$  search as defined in [15]. The signal expected from a SM Higgs boson is added to the background 1.7(b).

be detected from their leptonic decays. The final state of each b quark consists in a jet that is recognized in the analysis as originating from b quarks. The energy of the original b quark is estimated from the energies of all the particles in its jet and has a large uncertainty. So also for this channel the reconstructed mass of dijets shows a small excess above the background-only expectation over a large mass range (fig 1.8). The sensitivity of this analysis is actually lower than required for concluding whether a signal is present (as expected from SM prediction) or if the coupling to b quarks is different from what we would expect.

In conclusion, neither fermion decay mode shows, at present, a statistically significant enhancement over the background-only expectation. Nevertheless, at the present level of sensitivity the results in these channels are consistent with the production of the SM Higgs boson, in agreement with observations in the other three (diboson) decay modes.

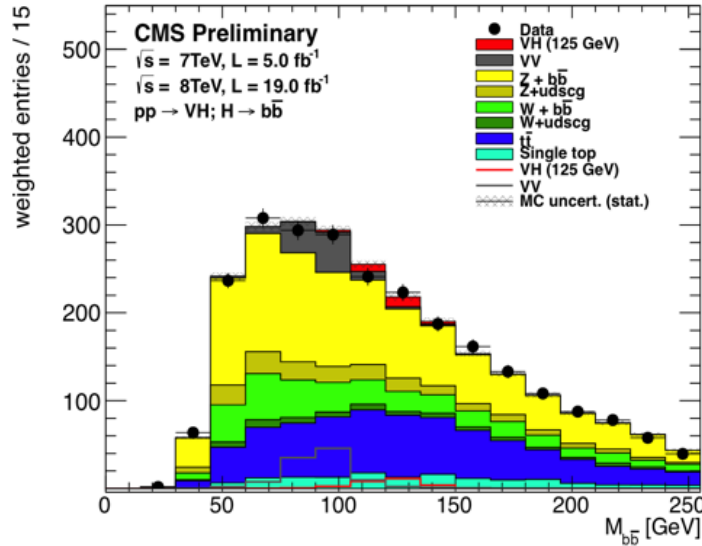


Figure 1.8: *Dijet invariant mass distribution, combined for all channels. The points are the data while the coloured histograms represent the expected signal and background. The signal used corresponds to the production of a Higgs boson with a mass of 125 GeV.*

## 1.5 Supersymmetry

Despite its success the SM is considered an incomplete theory. A number of questions remain: Why would the mass of the Higgs boson be only 125 GeV? What is dark matter? How does the matter-antimatter asymmetry arise? How is gravity to be included? Physics beyond the SM has been much discussed over the past few decades, and such physics might manifest itself via the production of exotic particles such as superparticles from a new symmetry, called Supersymmetry, heavy Z-like bosons in grand unified theories, or theories with extra space-time dimensions. In this thesis I will focus on the Supersymmetry (SUSY), omitting the discussion of the other possible theories beyond the Standard Model.

Supersymmetry is a generalization of the space-time symmetries of quantum field theory that transforms fermions into bosons and vice versa. It gives to each particle its superpartner which differ in spin by half a unit.

Supersymmetry provides a framework for the unification of particle physics

## 1. The SM Higgs and the new physics beyond it

---

and gravity [16, 17, 18, 19, 20] which is governed by the Planck energy scale,  $M_P \sim 10^{19}$  GeV, where the gravitational interactions become comparable in strength to the gauge interactions. It can provide a solution to the *hierarchy* problem and explain the smallness of the electroweak scale compared with the Planck scale. This is one of the problems of the SM where it is not possible to maintain the stability of the Gauge hierarchy in the presence of radiative quantum corrections. If SUSY were an exact symmetry of nature, then particles and their superpartners would be degenerate in mass. Since superpartners have not (yet) been observed, SUSY must be a broken symmetry. Nevertheless, the stability of the Gauge hierarchy can still be maintained if the breaking is soft [21, 22]. That means that the supersymmetry-breaking masses cannot be larger than a few TeV. The most interesting theories of this type are theories of *low-energy* (or *weak-scale*) supersymmetry, where the effective scale of SUSY breaking is tied to the scale of electroweak symmetry breaking [23, 24, 25, 26].

SUSY also allows the grand unification of the electromagnetic, weak and strong gauge interactions in a consistent way, as it is strongly supported by the prediction of the electroweak mixing angle at low energy scales, with an accuracy at the percent level.

A fundamental theory of supersymmetry breaking is unknown at this time. Nevertheless, one can parameterize the low-energy theory in terms of the most general set of soft SUSY-breaking normalisable operators. It is done by the so called Minimal Supersymmetric extension of the Standard Model (MSSM) [27] which associates a supersymmetric partner to each Gauge boson and chiral fermion of the SM, and provides a realistic model of physics at the weak scale.

### 1.5.1 Structure of the MSSM

The minimal supersymmetric extension of the Standard Model consists of taking the fields of the two-Higgs-doublet extension of the Standard Model and adding the corresponding supersymmetric partners [28, 29].

The corresponding field content of the MSSM and its Gauge quantum numbers are shown in figure (1.9). The Gauge super-multiplets consist of the gluons and their gluino fermionic superpartners, and the  $SU(2)_L \times U(1)_Y$  Gauge bosons and their gaugino fermionic superpartners. The Higgs multiplets consist

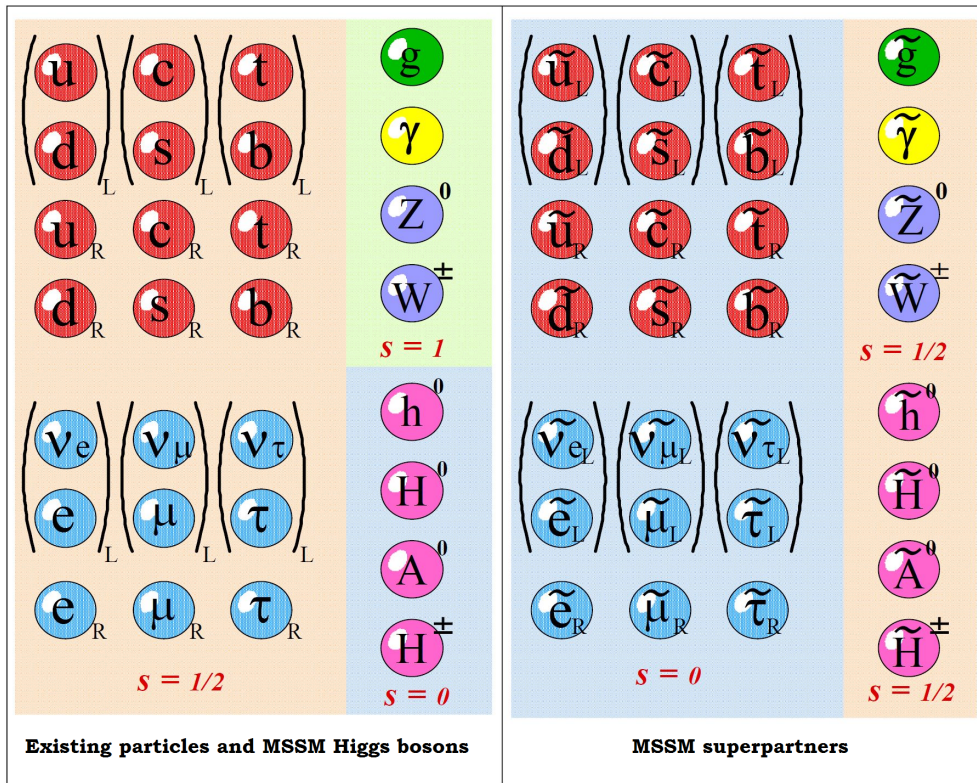


Figure 1.9: Particles predicted by the MSSM. In the left rectangle there are the particles existing in the SM and further four new Higgs bosons predicted by MSSM. In the right rectangle there are all the superpartners named as the conjugated particle with the addition, in case of fermions, of prefix s-, and in case of bosons whit suffix -ino.

of two complex doublets of Higgs fields, their higgsino fermionic superpartners, and the corresponding antiparticle fields. The matter super-multiplets consist of three generations of left-handed and right-handed quarks and lepton fields, their scalar superpartners (squark and slepton fields), and the corresponding antiparticle fields.

The MSSM Lagrangian is constructed by including all possible supersymmetric interaction terms (of dimension four or less) that satisfy  $SU(3)_C \times SU(2)_L \times U(1)_Y$  Gauge invariance and B-L conservation. As a consequence of B-L invariance, the MSSM fulfils a multiplicative R-parity invariance, where the quantum

## 1. The SM Higgs and the new physics beyond it

---

number is  $R = (-1)^{3(B-L)+2S}$  for a particle of spin  $S$  [30]. This implies that all the ordinary Standard Model particles have even  $R$  parity, whereas the corresponding supersymmetric partners have odd  $R$  parity.

The enlarged Higgs sector of the MSSM constitutes the minimal structure needed to guarantee the cancellation of anomalies from the introduction of the higgsino superpartners, and generate mass for both up-type and down-type quarks (and charged leptons) in a way consistent with the supersymmetry [31, 32, 33]. However more than 100 new parameters are introduced. Fortunately, only a subset of these parameters affect the Higgs phenomenology through tree-level and quantum effects.

The two complex scalar Higgs doublet with eight degrees of freedom are:

$$\Phi_d = \begin{pmatrix} \Phi_d^0 \\ \Phi_d^- \end{pmatrix}, \Phi_u = \begin{pmatrix} \Phi_u^+ \\ \Phi_u^0 \end{pmatrix} \quad (1.22)$$

where the  $\Phi_d$  couples exclusively to down-type fermion pairs while  $\Phi_u$  to up-type. When the Higgs potential is minimised, the neutral Higgs fields acquire vacuum expectation values:

$$\varphi_d = \frac{1}{\sqrt{2}}v_d. \quad (1.23)$$

A parameter  $\tan \beta$  is defined as the ratio between the vacuum expectation value of Higgs doublets:

$$\tan \beta \equiv \frac{v_u}{v_d} \quad (1.24)$$

where the normalization is chosen such that

$$v^2 \equiv v_u^2 + v_d^2 = (246 \text{ GeV})^2 \quad (1.25)$$

After electroweak symmetry breaking three of the eight degrees of freedom result in three Goldstone bosons, which are absorbed to give mass to vector bosons  $W^\pm$  and  $Z$ , and five Higgs bosons remain. They are the CP-odd neutral scalar  $A^0$ , the two charged scalars  $H^\pm$  and the two CP-even neutral scalars  $h^0$  and  $H^0$ . Among them, the neutral bosons will be called  $A$ ,  $H$ ,  $h$  or more generically  $\Phi$  in this thesis, where  $\Phi = h^0, A^0, H^0$  unless explicitly specified. The CP-even Higgs squared mass matrix is:

$$\mathcal{M}_{H,h}^2 = \begin{pmatrix} m_A^2 \sin^2 \beta + m_Z^2 \cos^2 \beta & -(m_A^2 + m_Z^2) \sin \beta \cos \beta \\ -(m_A^2 + m_Z^2) \sin \beta \cos \beta & m_A^2 \sin^2 \beta + m_Z^2 \cos^2 \beta \end{pmatrix} \quad (1.26)$$

It is interesting to note from the (1.26) that at tree level we can express the MSSM bosons masses in terms of just two parameters: the mass of the neutral scalar  $A$   $m_A$  and  $\tan \beta$ . The mass of charged Higgs bosons  $H_m$  is

$$m_{H^\pm}^2 = m_W^2 + m_A^2 \quad (1.27)$$

$$m_h^2 = \frac{1}{2} \left( m_A^2 + m_Z^2 - [(m_A^2 + m_Z^2)^2 - 4m_A^2 m_Z^2 \cos^2 2\beta]^{1/2} \right) \quad (1.28)$$

$$m_H^2 = \frac{1}{2} \left( m_A^2 + m_Z^2 + [(m_A^2 + m_Z^2)^2 - 4m_A^2 m_Z^2 \cos^2 2\beta]^{1/2} \right) \quad (1.29)$$

where  $m_W$  and  $m_Z$  are the masses of the  $W^\pm$  and  $Z$  bosons. It implies some constraints the Higgs self-interaction terms, that are related to the electroweak Gauge coupling constants. A significant consequence of it is a tree-level upper bound to the mass of the light CP-even Higgs boson,  $h$ , deriving from the equation (1.28):

$$m_h \leq m_Z + \cos^2 2\beta \quad (1.30)$$

This is an important difference between the MSSM and the SM, where the Higgs mass  $m_{HSM}^2 = \frac{1}{2} \lambda v^2$  is proportional to the Higgs self-coupling  $\lambda$ , which is a free parameter. On the other hand, all Higgs self-coupling parameters of the MSSM are related to the squares of the electroweak Gauge couplings.



## Chapter 2

# The CMS Experiment at the LHC

### 2.1 The Large Hadron Collider

The LHC is the world's largest and highest-energy particle accelerator and it is situated 100 m underground beneath the Franco-Swiss border near Geneva, Switzerland. The LHC is the latest and most advanced accelerating machine built by the European Organization for Nuclear Research (CERN).

The CERN is an international organization founded on 29 September 1954, its main function is to provide the particle accelerators and other infrastructure needed for high-energy physics research.

The LHC project [34] was approved by the Cern Council on 16 December 1994 and the actual construction started in 2001. The decision was to construct a proton collider to study the Standard Model physics at the TeV energy scale, in particular the Higgs mechanism, and to investigate a wide range of possible scenarios beyond the SM.

The design choice to collide proton-proton beams has several advantages. The loss of energy due to synchrotron radiation in case of circular motion of charged particles is proportional to the inverse of the fourth power of the particle mass. So using the proton, which has a mass about 2000 times the one of the electron, it has been possible to reuse the same tunnel of the CERN Large Electron-Positron Collider (LEP [35]) and to design a machine that will be able to reach a beam energy of 7 TeV (with respect to the 100 GeV of LEP).

Moreover protons are not elementary particles, hence, in hard collisions, the

## 2. The CMS Experiment at the LHC

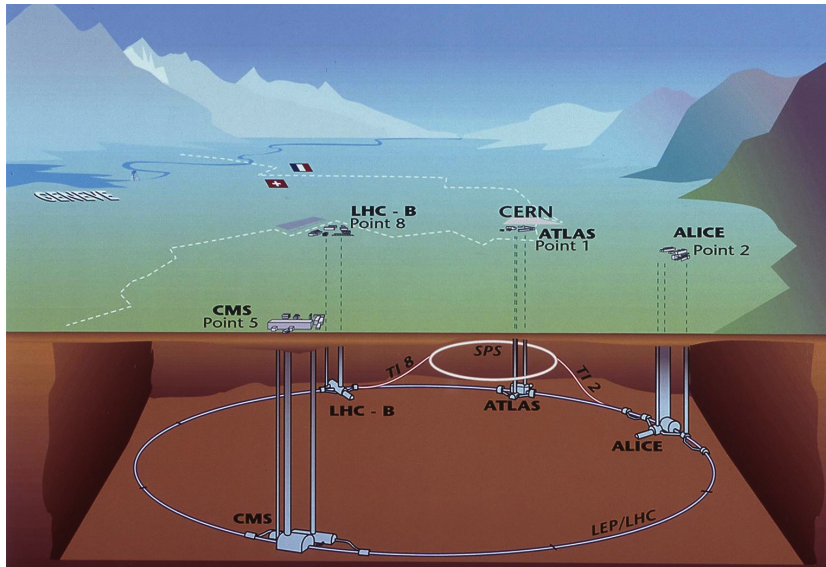


Figure 2.1: *Map of the LHC Accelerator and the four main experimental detectors.*

$pp$  interaction involves the particle constituents, which do not carry a fixed fraction of the hadron energy. So at a fixed energy of the beams it's possible to explore phenomena in a wide range of energies, key feature for a discovery machine. With respect to the Tevatron accelerator at FermiLab, which collides protons with anti-protons, it was also decided to use only protons for different reasons. In fact, the difference  $pp$  and  $p\bar{p}$  total cross sections becomes very small at high energies, and the proton production is faster and more efficient with respect to the antiproton one, thus allowing to reach higher luminosity and keep beam stability. LHC is also able to accelerate heavy ions up to lead with unprecedented energy, up to 1148 TeV in the center of mass, opening a new frontier in the study of Quark-Gluon Plasma, which existed in the early universe.

The LHC beams cross at four interaction points, as shown in Fig. 2.1, where four detectors are placed. ATLAS (A Toroidal LHC Apparatus) and CMS (Compact Muon Solenoid) are general purpose detectors devoted to the study of Standard Model and to the search of new physics beyond it. ALICE (A Large Ion Collider Experiment) is especially designed for the heavy ions collisions focusing on the study of the Quark-Gluon Plasma and LHCb (LHC beauty experiment) will perform precise measurements of CP violation in the b-hadron sector. Two further

experiments, TOTEM and LHCf, are much smaller in size. They are designed to focus on forward physics in order to study the total proton cross section, elastic scattering and diffraction dissociation. They are positioned respectively near the CMS and ATLAS detectors.

### 2.1.1 The accelerator

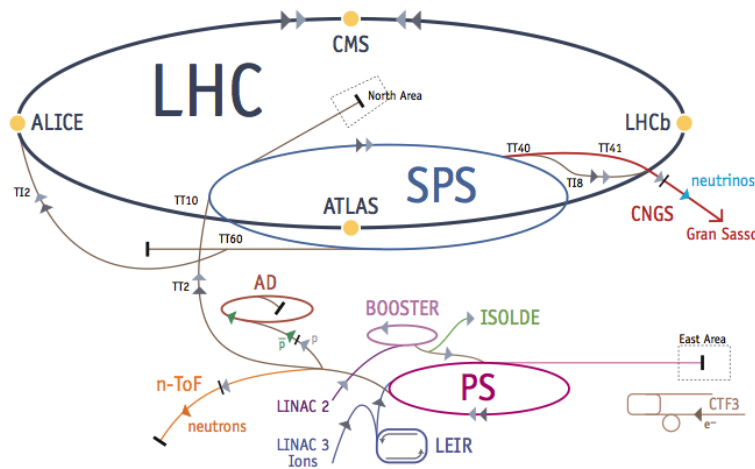


Figure 2.2: *The CERN accelerator complex.*

The LHC accelerator takes advantage of a series of pre-existing CERN accelerators (shown in Fig. 2.2) in order to obtain an injection energy of 450 GeV per beam. In the first step the protons are produced by hydrogen ionization and then accelerated to the energy of 50 MeV by a linear accelerator (LINAC). Protons are then injected into the Proton Synchrotron Booster (PSB), where the energy reaches 1.4 GeV and subsequently the Proton Synchrotron (PS) accelerates them to 25 GeV. The last step of acceleration is made by the 6.9 Km Super Proton Synchrotron (SPS) where the beams reach the injection energy of 450 GeV. They are then transferred to the 27 Km LHC ring. Here the proton bunches are accumulated, accelerated to their peak energy, and finally circulated for 10 to 24 hours while collisions occur at the four intersection points.

When LHC operates as a heavy ion accelerator, lead ions are first accelerated by the linear accelerator LINAC 3, and the Low-Energy Ion Ring (LEIR) is used

## 2. The CMS Experiment at the LHC

as an ion storage and cooler unit. The ions then are further accelerated by the PS and SPS before being injected into LHC ring, where they will reach an energy of 2.76 TeV per nucleon (or 575 TeV per ion).

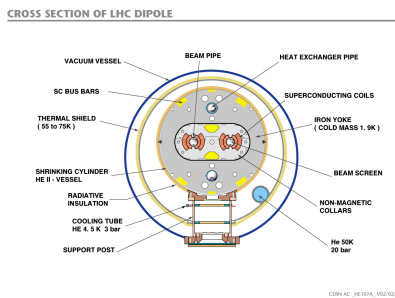


Figure 2.3: Section of a LHC dipole

Machine Parameter	Value
Circumference [Km]	26.659
Beam Radius at interaction point [ $\mu\text{m}$ ]	15
Number of dipoles	1232
Length of dipoles [m]	14.3
Field of dipoles at injection [T]	0.535
Field of dipoles for 7 TeV beams [T]	8.33
Number of quadrupoles	520

Figure 2.4: LHC technical parameters.

Accelerating two beams of same charge requires two separate acceleration cavities with two different magnetic field configurations. The bending power needed to keep the beam circulating is the limiting factor to the achievable centre of mass energy. In case of LHC it's supplied by about 1200 superconducting dipoles (Fig. 2.3), able to reach a stable 8.3 T field. 392 quadrupole magnets are used to keep the beams focused, in order to maximize the chances of interaction between the particles in the four intersection points. In total, over 1,600 superconducting magnets are installed, with most weighing over 27 tonnes. Approximately 96 tonnes of liquid helium are needed to keep the magnets, at their operating temperature of 1.9 K, making the LHC the largest cryogenic facility in the world at superfluid helium temperature.

### 2.1.2 Luminosity

A key parameter for the discovery potential of experiments at LHC is the machine luminosity ( $\mathcal{L}$ ). In the general case of two colliding beams, the luminosity

writes:

$$\mathcal{L} = f_{rev} n_b \frac{N_1 N_2}{A} \quad (2.1)$$

where  $f_{rev}$  is the revolution frequency,  $n_b$  is the number of bunches per beam,  $N_1$  and  $N_2$  are the number of particles in the bunches of each colliding beam, and  $A$  is the cross section of the beams. At LHC, the bunches are filled with roughly the same number of protons so  $N_1 = N_2 = N_b$ . The cross section of the beam writes:

$$A = 4\pi\epsilon_n \frac{\beta^*}{\gamma_r} \quad (2.2)$$

where  $\epsilon_n$  is the normalized transverse beam emittance (which measures the extent occupied by the particles of the beam in position and momentum phase space), and  $\beta^*$  is the beta function at collision point, which measures the beam focalization. That is then corrected by the relativistic gamma factor  $\gamma_r$ . Finally, the expression in 2.1 has to be corrected by a geometric luminosity reduction factor,  $F$ , due to the crossing angle at the interaction point. Hence, the final expression of the luminosity writes:

$$\mathcal{L} = \frac{f_{rev} n_b N_b^2 \gamma_r}{4\pi\epsilon_n \beta^*} F \quad (2.3)$$

The CMS and ATLAS experiments are designed to take advantage of the high luminosity deliverable by LHC. The design values for the collision at their interaction points are reported in Table 2.1. LHCb target luminosity is of the order of  $10^{32} \text{cm}^{-2} \text{s}^{-1}$ . The luminosity is even lower for ALICE which is designed for the Pb-Pb collisions (Alice design luminosity is  $2 \cdot 10^{27} \text{cm}^{-2} \text{s}^{-1}$ ).

### 2.1.3 LHC operations

Beams were circulated for the first time in LHC on 10 September 2008, but just 8 days after, a major technical incident forced a long stop. Investigations showed that cause of the incident was a faulty electrical connection between two of the accelerator's magnets. This fault resulted in mechanical damage and release of helium for the cooling of the magnet cold mass into the tunnel. The repairs and the deployment of a better protection system took more than one year, nevertheless, in order to operate the accelerator safely, it was decided to limit the maximum beam energy to 4 TeV. Higher energies would be achieved after a long

## 2. The CMS Experiment at the LHC

Parameter	Value
Luminosity ( $\mathcal{L}$ )	$10^{34} \text{cm}^{-2} \text{s}^{-1}$
Number of particles per bunch ( $N_b$ )	$1.1 \cdot 10^{11}$
Number of bunches ( $n_b$ )	2808
Beta function at impact point ( $\beta^*$ )	0.55 m
Normalized transverse beam emittance ( $\epsilon_n$ )	$3.75 \mu\text{m}$
Relativistic gamma $\gamma_r$	479.6
Geometric luminosity reduction factor $F$	0.836
Luminosity lifetime	10 h
Time between collisions	24.96 ns
Bunch crossing rate	40.08 MHz
Stored energy in the beams	362 MJ
Circulating beam current	0.582 A

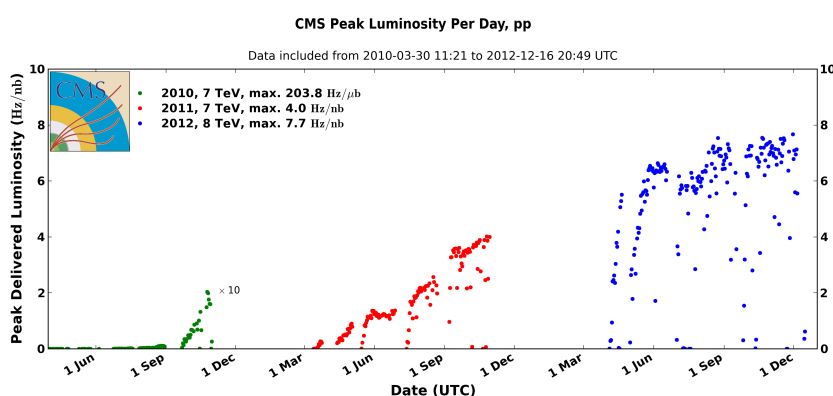
Table 2.1: *LHC design parameter for collisions at ATLAS and CMS.*

shut down scheduled for 2013, when extensive intervention would be performed on the machine.

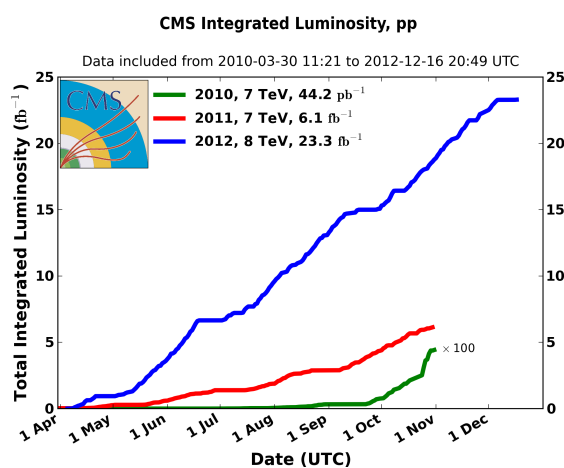
On 23 November 2009 the accelerator produced the first proton-proton collision. After a few pilot runs at energies of 450 GeV and 1.18 TeV per beam, the energy was ramped up to 3.5 TeV, reaching the first collision at a centre-of-mass energy of 7 TeV on 30th March 2010, the highest ever reached at a particle collider. With respect to the design parameters of Table 2.1 the luminosity has been gradually increased up to  $2 \cdot 10^{32} \text{cm}^{-2} \text{s}^{-1}$  with a maximum of 400 bunches spaced down to 150 ns. The proton-proton operation continued smoothly also in 2011 when a record instantaneous luminosity of  $3.6 \cdot 10^{33} \text{cm}^{-2} \text{s}^{-1}$  was reached, with up to 1380 bunches of  $1.4 \cdot 10^{11}$  protons spaced down to 50 ns. By the end of the 2011 run, more than  $5 \text{fb}^{-1}$  of integrated luminosity has been delivered to CMS and ATLAS. During the first two years of operation 2010 and 2011, the centre of mass energy was 7 TeV and was increased to 8 TeV in 2012. Also the bunch spacing changed during the years of running of the LHC: it was reduced gradually from 150 ns in 2010 to 50 ns in 2012. In 2012 there were 1368 bunches per beam and the intensity was  $1.6$  to  $1.7 \times 10^{11}$  protons per bunch, delivering a total integrated luminosity in collision at 8 TeV of about  $20 \text{fb}^{-1}$ . In Fig 2.5 the

evolution of instantaneous and integrated luminosity during the three years of data taking is shown.

Some tests of proton-proton collisions took place with the nominal bunch spacing of 25 ns. The nominal centre of mass energy of 14 TeV is going to be achieved after the Long Shutdown 1 (LS1), most probably in 2015.



(a)



(b)

Figure 2.5: LHC maximum instantaneous luminosity (a) and delivered integrated luminosity (b) to the CMS experiment during the three years of proton-proton run.

### 2.1.4 Proton-proton collision at LHC

The event rate of a process with cross section  $\sigma$  at a certain instantaneous luminosity (Equation 2.3) is given by

$$R = \mathcal{L} \cdot \sigma \quad (2.4)$$

The total inelastic cross section for proton-proton collision was expected to be  $\sigma_{pp} = 80$  mb at design condition, and was measured by the various experiment. The TOTEM [36] experiment, specifically designed for this kind of measurement, quoted the values of  $\sigma_{inel} = 73.5 \pm 1.3$  mb [37] and  $\sigma_{inel} = 74.7 \pm 1.7$  mb [38] for proton-proton collisions at 7 and 8 TeV respectively (see Fig. 2.6).

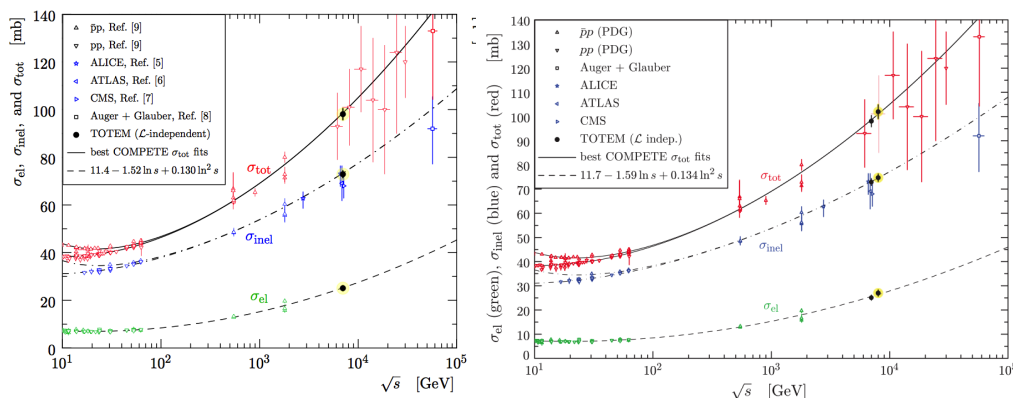


Figure 2.6: *Dependence of the cross sections  $\sigma_{tot}$ ,  $\sigma_{inel}$  and  $\sigma_{el}$  on the centre of mass energy. The continuous lines are best fits to  $\sigma_{tot}$  by the COMPETE collaboration, the dashed line is a fit to elastic-scattering data and the dash dotted line  $\sigma_{inel}$  is obtained from the difference between the continuous and dashed fits. On the left are shown the results of the TOTEM Collaboration for 7 TeV, and on the right for collisions at 8 TeV.*

The inelastic cross section includes two classes of interactions. In the first the two incoming protons can just transfer a small momentum at large distance (called soft collisions). In this case particle scattering at large angle is suppressed and most of the final state particles escape down the beam pipe.

In the second type of interaction, since protons are not elementary particles, collisions occur between two of their constituents (partons, i.e quarks and gluons),

and this results in a high transferred momentum in the direction transverse to the beam direction ( $p_T$ ). These are called hard collisions and usually contain the most interesting physics events.

The rate of hard collisions is many orders of magnitude lower than that of soft interactions so, even if particles produced in soft collisions are mostly distributed in the forward region, the residual tail at high  $p_T$  is competitive with the hard interaction rate, and constitutes a background to high  $p_T$  signal events.

In hard interactions the effective centre-of-mass energy  $\sqrt{\hat{s}}$  is given by the centre-of-mass energy of the two partons, and it's proportional to the fraction of energy carried by the two partons. The distribution of the fractional momentum of partons inside protons is called *parton distribution function* (PDF). These distributions are different for each parton and are functions of the exchanged momentum  $Q^2$ . At high  $Q^2$  the contribution of gluons and sea quarks increases with respect to that of valence quarks.

Due to the high luminosity of the machine at the design condition, the collision rate (Equation 2.4) would be of the order of  $10^9$  Hz, which would result in about 25 collisions every bunch crossing. The presence of more than one collision event per bunch crossing is usually referred as *pile-up* (PU), and only ATLAS and CMS experiment have been designed to take data in a high pile-up environment. The PU has been almost negligible in the 2010 run, but already in 2011 the average collision in a bunch crossing has been about ten to become of the order of twenty collisions in the 2012. The inconvenience of PU is needed in order to achieve a sufficient rate for very rare processes with small cross section. Cross sections and events rates for the main processes produced at the LHC are reported in Fig. 2.7 as a function of centre-of-mass energy.

### 2.1.5 The LHC data management

One of the main challenges of the experiments at LHC will be the management of the huge amount of data that will be recorded. At design condition the Large Hadron Collider will produce annually roughly 15 petabytes of data, that have to be accessible to thousands of scientists around the world. In order to cope with this need CERN is collaborating with institutions in 34 different countries to operate a distributed computing and data storage infrastructure: the Worldwide

## 2. The CMS Experiment at the LHC

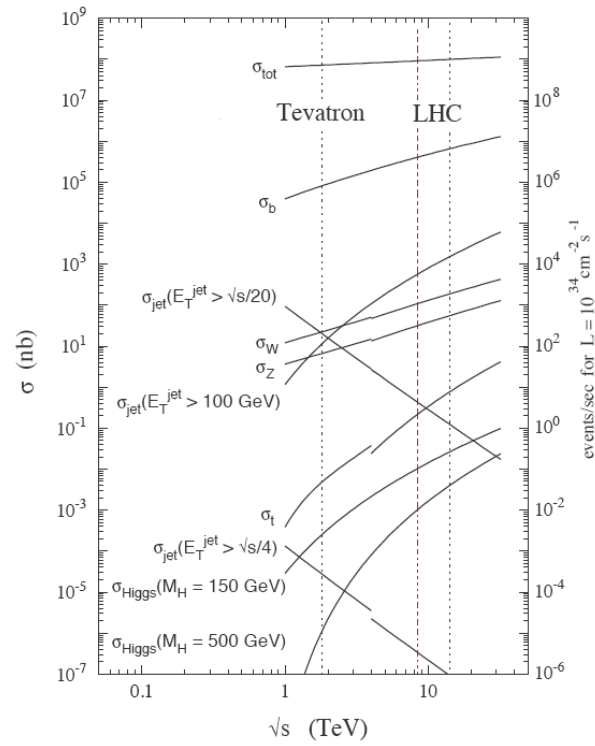


Figure 2.7: Cross Section and event rates of several processes as a functions of the centre-of-mass energy of  $p$ - $p$  collisions. For LHC are considered the design energy (black) and the actual one (around 7-8 TeV, in red).

LHC Computing Grid (WLCG [39]). The GRID is structured in several layers, called Tiers, as shown in Fig.2.8.

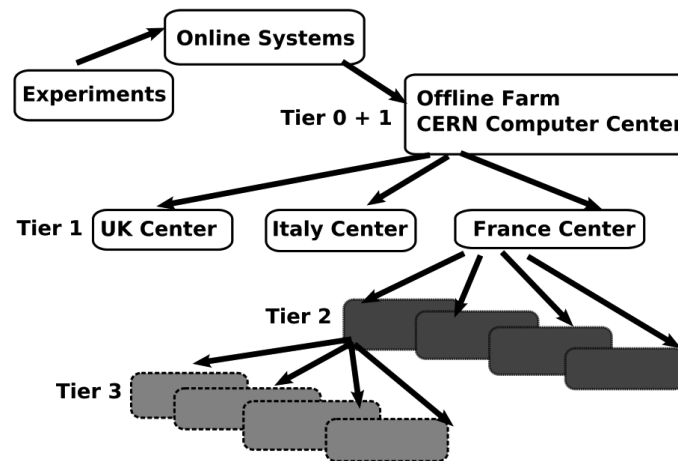


Figure 2.8: *Schematic structure of the LHC Computing Grid Tier system [40].*

The original raw data emerging from the data acquisition systems will be recorded at the Tier-0 centre at CERN. The first-pass reconstruction will take place at the Tier-0, where a copy of the reconstructed data will be stored. The Tier-0 will then distribute this data across the Tier-1 centres (large computer centres - in Canada, France, Germany, Italy, the Netherlands, the Nordic countries, Spain, Taipei, the UK, and two sites in the USA) where sufficient storage capacity is available for a large fraction of the data, and with round-the-clock support for the computing grid. These so-called Tier-1 centres make the data available to over 200 Tier-2 centres for specific analysis tasks. Individual scientists can then access the LHC data from their home country, using local computer clusters (Tier-3 or even individual PCs). This new type of globally distributed model for data storage and analysis - a computing Grid - was chosen instead of a centralized one because it provides several key benefits. In particular:

- the significant costs of maintaining and upgrading the necessary resources for such a computing challenge are more easily handled in a distributed environment, where individual institutes and participating national organizations can fund local computing resources and retain responsibility for these,

while still contributing to the global goal.

- in a distributed system there are no single points of failure. Multiple copies of data and automatic reassigning of computational tasks to available resources ensure load balancing of resources and facilitate access to the data for all the scientists involved, independently of geographical location. Spanning all time zones also facilitates round-the-clock monitoring and support.

## 2.2 The CMS experiment

The Compact Muon Solenoid [41] is one of the two general purpose detectors at the Large Hadron Collider. Its aim is to study a large spectrum of physical phenomena, starting from the completion of the Standard Model predictions looking for the Higgs Boson and up to the search for new physics beyond the Standard Model at the TeV scale. In Fig. 2.9 an expanded section of the CMS detector is shown, with highlighted the main sub-detectors. The experiment is located in an underground cavern at LHC experimental point number five, near the french town of Cessy. The main characteristic of the detector is a strong super-conductive solenoidal magnet, which can reach a 4 T field and dictates the cylindrical shape of the experiment. Another characteristic of CMS is its modularity. This had made it possible to build CMS on surface, while the experimental cavern was being excavated, and it was lowered one section at the time in 2007. The magnet occupies the central region of the detector, called *barrel*, which is externally subdivided in 5 wheels. The wheels compose the iron yoke for the return of the magnetic fields, and contain the chambers for the detection of muons. The central wheel (designated wheel 0) is also the structural support for the magnet to which it is connected (see Fig. 2.10(a)). The *barrel* region is closed on both ends by three instrumented iron disks called *endcaps* (see Fig. 2.10(b)). Once closed, the detector is quite compact (at least with respect to ATLAS), being a cilinder 21.6 m long and with a diameter of 14.6 m. Its total mass is of about 14500 t.

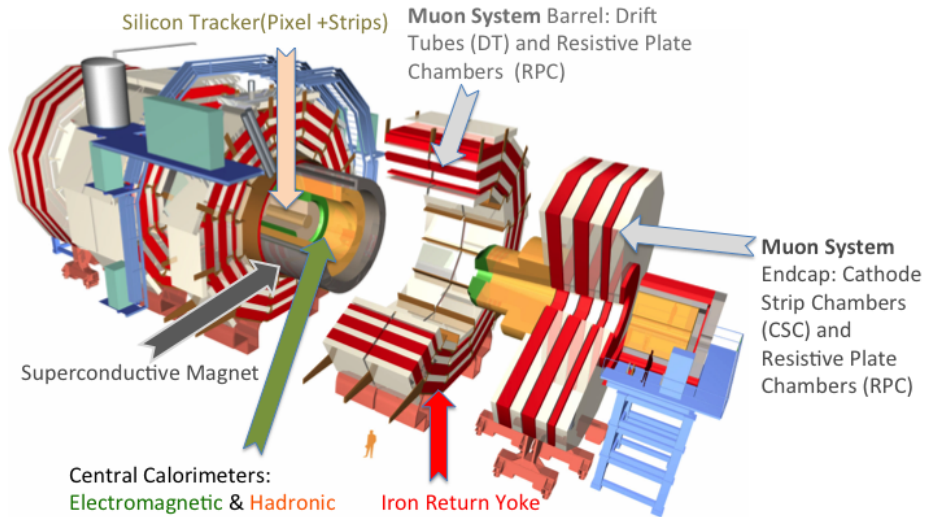
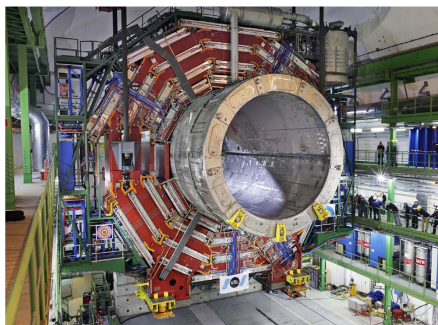


Figure 2.9: *Section view of the CMS detector.*



(a)



(b)

Figure 2.10: *Lowering in the experimental cavern of the central barrel wheel and magnet (a) and of two endcaps disks (b) at the beginning of 2007.*

### 2.2.1 CMS Coordinate system

The CMS coordinate system used to describe the detector is a right-handed Cartesian frame, centred in the interaction point and with the  $z$  axis along the beam line (this direction is referred to as *longitudinal*) from the LHC point 5 to the mount of Jura. The  $x$  axis is chosen to be horizontal and pointing towards the centre of the LHC ring, and the  $y$  axis is vertical and pointing upwards. The  $x$ - $y$  plane is called *transverse* plane.

Given the cylindrical symmetry of the CMS design, usually a  $(\phi, \theta)$  cylindrical coordinate system is used in the reconstruction of the tracks of particles.  $\phi$  is the polar angle, laying in the  $x$ - $y$  plane, measured from the  $x$ -axis in mathematical positive direction (i.e. the  $y$ -axis is at  $\phi = 90^\circ$ ). The azimuthal angle  $\theta$  is measured from the  $z$ -axis towards the  $x$ - $y$  plane. The angle  $\theta$  can be translated into the pseudo-rapidity  $\eta$  by

$$\eta = -\ln \left( \tan \frac{\theta}{2} \right) \quad (2.5)$$

The actual value of  $\eta$  can be seen in the longitudinal view of the detector in Fig. 2.11(b). Using these parameters, the distance between two particles can be defined as

$$\Delta R = \sqrt{\Delta\phi^2 + \Delta\eta^2} \quad (2.6)$$

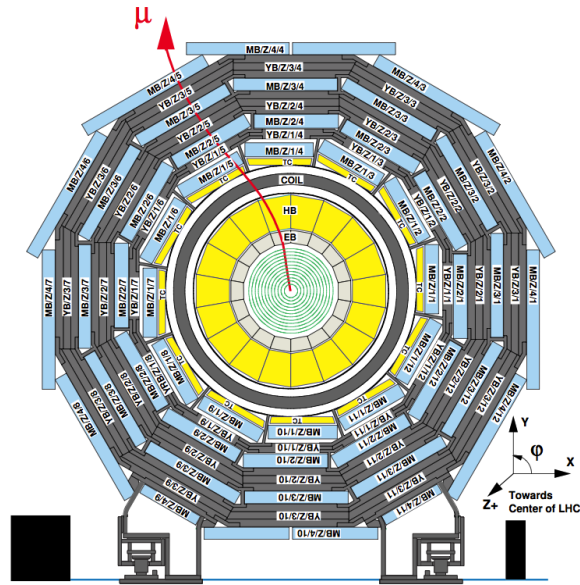
Referring to the Cartesian system, the momentum of a particle can be divided in two components: the *longitudinal momentum*  $p_z$  and the *transverse momentum*  $p_T$ , defined as:

$$p_T = \sqrt{p_z^2 + p_y^2} \quad (2.7)$$

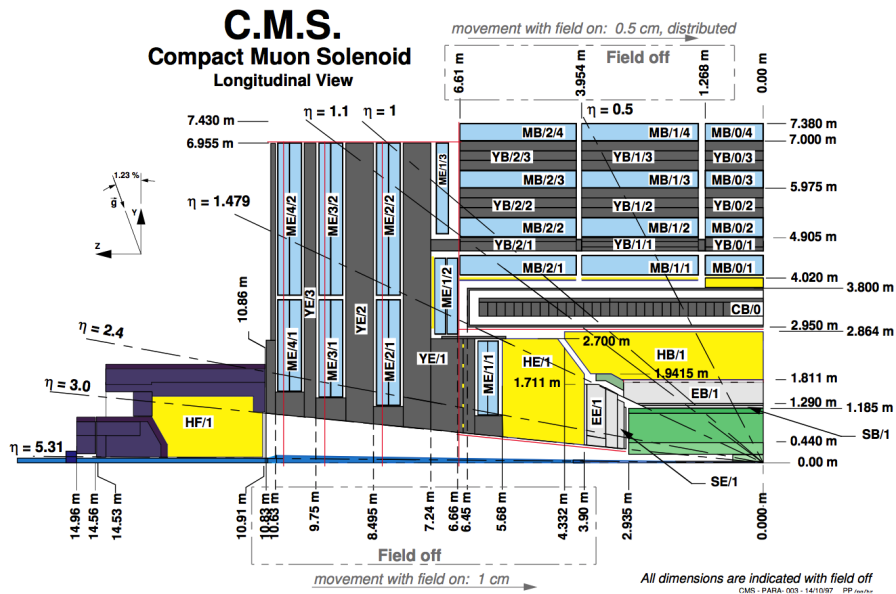
The magnet bends charged tracks on the  $\phi$  plane, so what is effectively measured is the  $p_T$  of the particles. For a particle of energy  $E$ , the variable *rapidity* ( $y$ ) is also introduced, defined as

$$y = \operatorname{arctanh} \frac{|\vec{p}|c}{E} = \frac{1}{2} \ln \left( \frac{E + p_z c}{E - p_z c} \right) \quad (2.8)$$

For high energy particles rapidity can be approximated by pseudorapidity. Both rapidity and  $p_T$  are used because parton collision (see Section 2.1.4) can have the center-of-mass of the interaction boosted along the  $z$  direction; both these quantities have invariance properties under this kind of boost.



(a)



(b)

Figure 2.11: On (a) a transverse view of CMS in the barrel region. On (b) a longitudinal view of one quarter of the detector.

## 2.2.2 Inner Tracking System

Outside the beam pipe, the first sub-detector found by particles coming from the interaction point is the inner tracking system ("Tracker"), a system of silicon sensors designed to provide a precise and efficient measurement of the trajectories of charged particles. The Tracker consists of two major parts, an internal silicon pixel detector and an outer silicon strip detector. The overall length of the Tracker is 5.4 m with an outer diameter of 2.4 m.

### The Pixel Detector

The pixel detector [42] consists of three cylindrical layers of hybrid pixel modules surrounding the interaction point at radii of 4.4, 7.3 and 10.2 cm. Two disks of pixel modules on each side complement the pixel detector, as shown in Fig. 2.12(a). It is built to ensure precise 3D vertex reconstruction to allow efficient  $\tau$  and  $b$  jets identification and covers a pseudorapidity range up to  $|\eta| < 2.5$  (see Fig. 2.12(b), 2.12(c)).

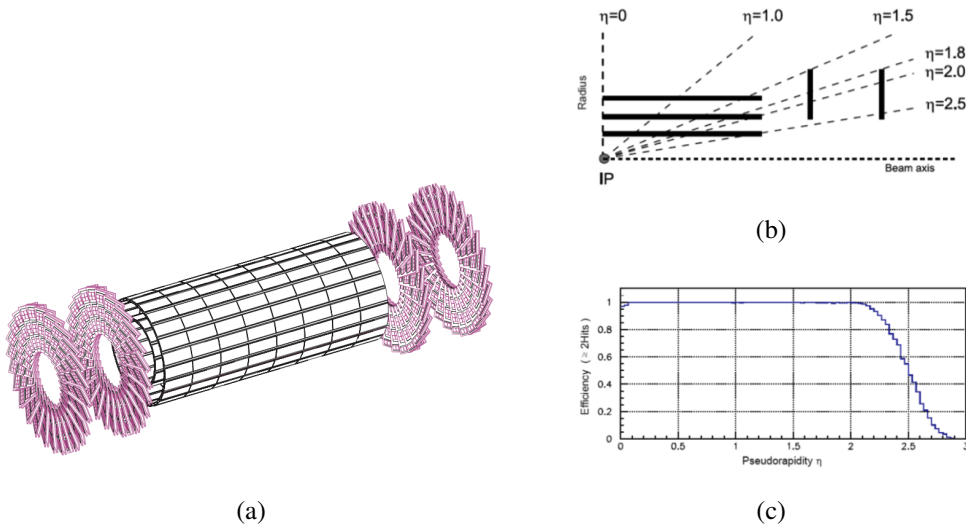


Figure 2.12: Overview of the pixel detector layout (a); longitudinal view of one quarter of the pixel detector (b) and its hit coverage as a function of  $\hat{I}$  (c).

The 66 million active silicon sensors are realized on high-resistance n-substrate, with an implanted pn-junction and a pixel cell size of  $100 \times 150 \mu\text{m}^2$ . The minimal pixel cell area is dictated by the readout circuit surface required for each pixel and

the small pixel size allows to keep single channel occupancy per bunch crossing around  $10^{-4}$  even in the future high flux scenario ( $10^7$  particles/s at 10 cm).

In localizing secondary decay vertices, both transverse and longitudinal coordinates are important and a nearly square pixel shape is adopted. Indium bumps are deposited onto the sensors for subsequent connection to the readout electronics. Movable electrons and holes are created in silicon by ionisation, if a charged particle traverses it. Applying high voltage, these movable charge carriers can be separated and measured as a current, as illustrated in Fig. 2.13(a).

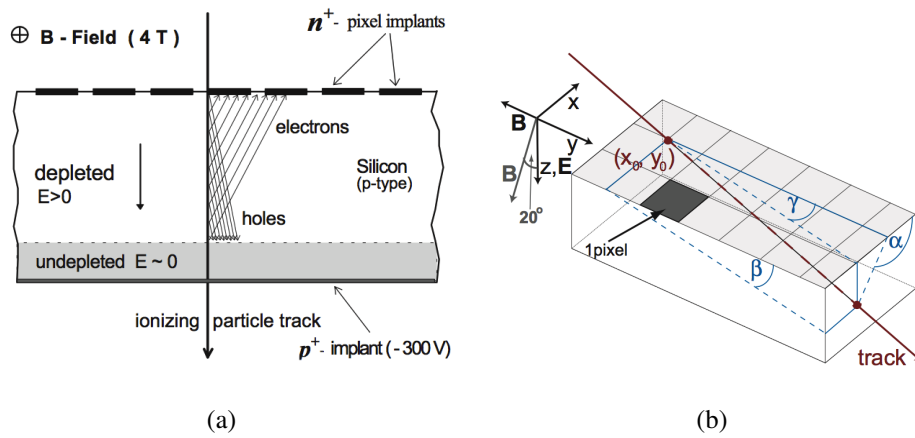


Figure 2.13: *Functionality of silicon based particle detection (a). On (b) sketch of the track impact angles with respect to a pixel sensor. The magnetic field vector is anti-parallel to the y axis for the barrel sensors and at  $20^\circ$  with respect to the z axis for the endcap sensors.*

Since the deposited charge is often shared among several pixels, an analog charge readout is implemented. Charge sharing enables interpolation between pixels, which improves the spatial resolution. In the barrel section the charge sharing in the  $r\phi$ -direction is largely due to the Lorentz effect: the charges drift at an angle (Lorentz angle) relative to the direction of the electric field. The pixel hit reconstruction exploits this effect to improve the spatial resolution by interpolating the charge collected in a cluster. Once the interpolation is done the resulting position is adjusted to account for the Lorentz drift. Because the pixel barrel sensor planes are parallel to the magnetic field, the Lorentz drift is both maximal and in the azimuthal direction. In the endcap pixels the sharing is enhanced by arranging the blades in the turbine-like layout. The spread of the charge over

## 2. The CMS Experiment at the LHC

neighboring pixels depends on the particle's incidence angle and has a minimum for tracks parallel to the drift direction of the charge carriers. The Lorentz angle is extracted by finding the minimum of the mean cluster size along the local  $x$  coordinate measured as a function of the cotangent of the incidence angle  $\alpha$ , as shown in Fig. 2.13(b).

The resulting hit resolution depends on the cluster size and position, and is in general between 10 and 25  $\mu\text{m}$  (Fig. 2.14(a)). In the first two years of operation the detector has shown a hit reconstruction efficiency of about 99.8%, as shown in Fig 2.14(b).

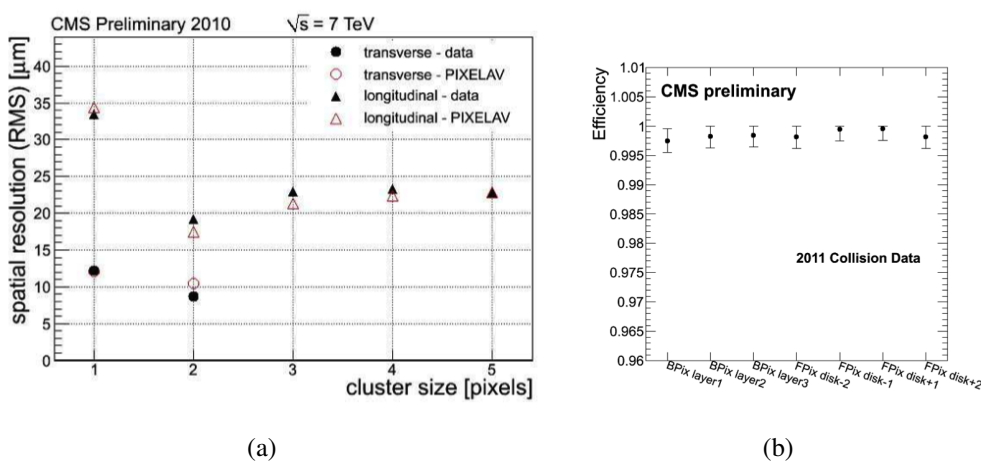


Figure 2.14: In (a) transverse and longitudinal pixel spatial resolution as a function of the cluster size. Full dots and triangles are measurements, open symbols are simulations. In (b) its reconstruction efficiency as measured for all layers of the tracker.

### The strip detector

The pixel system is surrounded by the Silicon Strip Tracker (SST). With its more than 9.3 million detector channels, 15000 silicon modules and a total active detector area of about 200  $\text{m}^2$ , it is the largest silicon tracker ever built. The SST was completed at CERN using the tracker integration facility, a clean room with facilities to assemble, connect and operate parts of the tracker in turn. The sealed SST was finally transported to the experimental area and lifted down into the cavern.

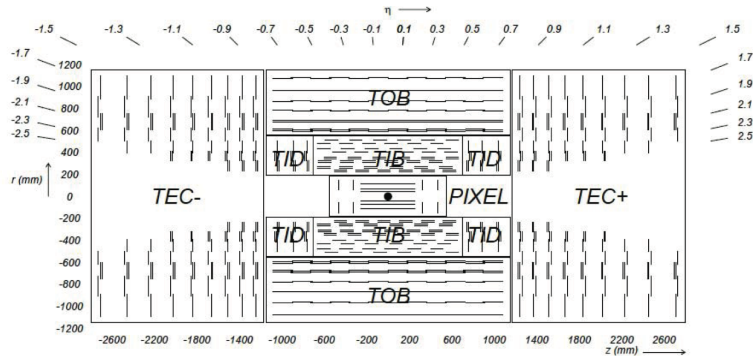


Figure 2.15: *The tracker schematic structure.*

The SST consists of four main subsystems, shown in Fig.2.15 the four-layer Tracker Inner Barrel (TIB), the six-layer Tracker Outer Barrel (TOB) and, on each side of the barrel region, the three-disk Tracker Inner Disks (TID), and the nine-disk Tracker End Caps (TEC). Each TID disk is made of three rings of modules, while TEC disks have seven rings. The entire system is operated at a temperature below  $10^{\circ}\text{C}$ . The active detector elements, the silicon modules, consist of a carbon or graphite fibre frame, which supports the silicon sensor and the associated front-end readout electronics. The silicon sensors are made up of single-sided  $p^+$  strips on  $n$ -bulk sensors with two different thicknesses:  $320\ \mu\text{m}$  and  $500\ \mu\text{m}$  in the inner four and outer six layers of the barrel, respectively;  $320\ \mu\text{m}$  in the inner disks, and  $320\ \mu\text{m}$  and  $500\ \mu\text{m}$  in the inner four and outer three rings of the end cap disks, respectively. More than 20 different module geometries exist, with differences in terms of strip length, pitch and material resistivities, to ensure that the single strip occupancy is low even at full LHC luminosity. Both single-sided and double-sided modules (two single-sided modules mounted back to back with a stereo angle of  $100\ \text{mrad}$ ) are used. The final single hits resolution depends on the type of sensors and their position, and has been measured to be between  $15$  and  $45\ \mu\text{m}$ , in accordance to the design expectation (Fig. 2.16).

### 2.2.3 The Electromagnetic Calorimeter

The CMS Electromagnetic Calorimeter is composed of 75848 lead tungstate ( $\text{PbWO}_4$ ) crystals, chosen because of their excellent energy resolution. The de-

## 2. The CMS Experiment at the LHC

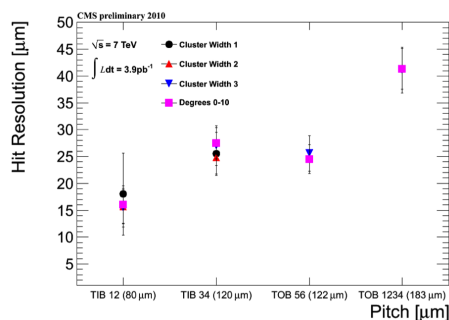


Figure 2.16: *Silicon strip hit resolution as a function of strip pitch.*

tector consists of a barrel region, extending to a pseudorapidity  $|\eta|$  of 1.48, and two endcaps, which extend coverage to  $|\eta| = 3.0$ . The Barrel section (EB) has an inner radius of 129 cm, and is structured as 36 identical supermodules, each covering half the barrel length. Each supermodule is composed by 1700 crystals with a front face cross-section of about  $22 \times 22 \text{ mm}^2$  and a length of 230 mm, corresponding to 25.8 radiation lengths ( $X_0$ ). The crystal axes are inclined at an angle of  $3^\circ$  relative to the direction of the nominal interaction point, in both the azimuthal ( $\phi$ ) and  $\eta$  projections.

The two ECAL endcaps (EE) are located at a distance of 314 cm from the vertex and are constructed from four half-disk dees, each consisting of 3662 tapered crystals, with a frontal area of  $2.68 \times 2.68 \text{ cm}^2$  and a length of 22 cm (corresponding to  $24.7 X_0$ ), arranged in a quasi-projective geometry. The crystals are focussed at a point 1.3 m farther than the nominal interaction point along the beam line, with off-pointing angles between  $2^\circ$  and  $8^\circ$ . The crystals in each dee are organised into 138 standard  $5 \times 5$  supercrystal units, and 18 special shaped supercrystals that are located at the inner and outer radii.

A Preshower detector (ES) is placed in front of the crystal calorimeter over the endcap pseudorapidity range  $1.653 < |\eta| < 2.6$ . Its active elements are two planes of silicon strip detectors, with a pitch of 1.9 mm, which lie behind disks of lead absorber at depths of  $2 X_0$  and  $3 X_0$ . A schematic layout of ECAL is reported in Fig. 2.17.

The scintillation light produced in the crystals is read-out by a pair of avalanche photo-diodes (APD) for each EB crystal, and a vacuum phototriode (VPT) for each EE crystal. The small Moliere radius ( $RM = 2.2 \text{ cm}$ ) in combination with

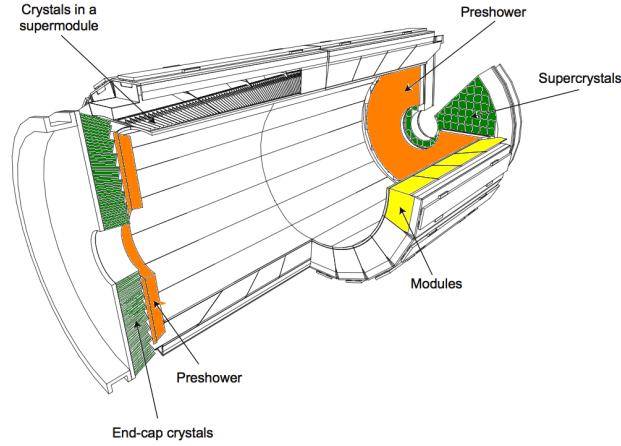


Figure 2.17: View of the CMS ECAL structure: Barrel (one supermodules in yellow), Endcap (in green), Preshower (in orange).

the large number of crystals results in a fine granularity for the lateral shower shape. In the forward region the granularity is further improved by the Preshower detector.

In order to achieve the desired energy resolution of the ECAL it is necessary to maintain the stability of the individual channel energy calibration over time. This places stringent requirements on the stability of the temperature of the ECAL and of the high voltage applied to the APDs. This is due to the temperature dependence of the crystal light yield, as well as the sensitivity of the APD gains to variations in both temperature and high voltage (the VPT response is much less sensitive to temperature and high voltage variations). The ECAL energy resolution measured in electron test beams is parameterized as

$$\left(\frac{\sigma}{E}\right)^2 = \left(\frac{\alpha}{\sqrt{E}}\right)^2 + \left(\frac{\sigma_n}{E}\right)^2 + c^2 \quad (2.9)$$

for electrons incident on the center of crystals [43]. The three contributions correspond to the stochastic term, the noise term and the constant term. The stochastic term depends on the event-by-event fluctuations in the electromagnetic shower development, on the photo-statistics and on the photodetector excess noise factor. The noise term depends on the level of the electronic noise and event pile-up. The constant term depends on the non-uniformity of the longitudinal light collection,

## 2. The CMS Experiment at the LHC

on the leakage of energy from the rear face of the crystals and on the accuracy of the detector inter-calibration constants.

For electromagnetic showers of energies above 100 GeV the energy resolution is dominated by the constant term. As a consequence, in the CMS environment the detector's performance will depend mainly on the quality of its inter-calibration and monitoring. Of particular importance are changes in crystal transparency under irradiation that have to be tracked in order to apply the needed correction, as can be seen in the example is in Fig. 2.18 and Fig. 2.19.

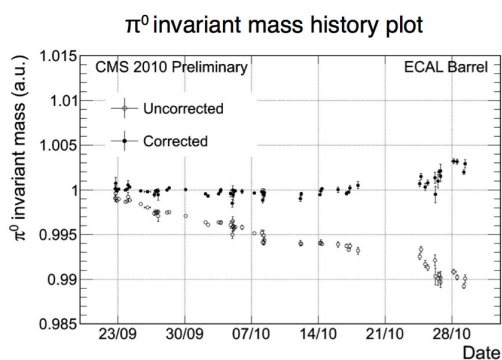


Figure 2.18:  $\pi_0$  invariant mass history plot in 2010 for the ECAL Barrel detector, before and after the corrections for the crystal transparency loss.

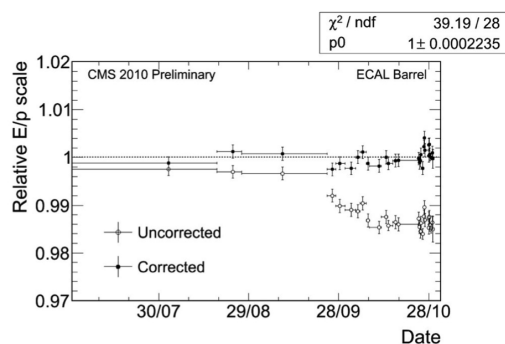


Figure 2.19:  $E/p$  history plot, with  $E$  = ECAL electron energy and  $p$  = Tracker electron momentum, for  $W \rightarrow e\nu$  decays measured in 2010 with the ECAL Barrel detector.

### 2.2.4 The Hadronic Calorimeter

The Hadron Calorimeter (HCAL) is used, together with the ECAL, to perform measurements on direction and energy of hadronic jets and to estimate the amount of missing transverse energy (missing  $E_T$ ) of each event. The request to perform precise missing  $E_T$  measurement implies the development of a very hermetic system, whose design is constrained by compactness requests and by the high magnetic field. In order to fulfill these requirements a sampling calorimeter system based on brass absorber layers alternated to active plastic scintillators has been built.

The signal coming from active scintillators is read out with embedded wavelength-shifting fibers (WLS) and conveyed via clear fiber wave-guides to hybrid photo-diodes. The choice of brass as absorber material has been driven from its short interaction length  $\lambda_I$  and its non-magnetic nature. The HCAL consists of the following parts:

- **HCAL Barrel region (HB).** It is located between the EB (see Section 2.2.3) and the solenoid and covers a range of  $|\eta| < 1.3$ . The HB contains brass absorber plates alternating with layers of plastic scintillator tiles, which have wavelength shifting fibres embedded for the signal readout. As this setup results in a material thickness of  $10.6 \cdot \lambda_I$  at  $|\eta| = 1.3$  and only  $5.82 \cdot \lambda_I$  at  $|\eta| = 0$ , the additional HCAL outer region is necessary. The segments of the HB have a tower-like readout, i.e. all the light collected by the scintillator tiles of one segment is directed to one Hybrid Photo Diode via fibres. Thus a two-dimensional resolution of  $\Delta\phi = 5^\circ$  and  $\Delta\eta = 0.087$  is obtained.
- **HCAL Outer region (HO).** In order to guarantee the containment of lately developing and highly energetic hadronic showers within the calorimeter of the CMS barrel, an additional layer, the HO, is needed. It is also located in the barrel region, but outside the solenoid, and covers  $|\eta| < 1.3$  as well. It consists of five wheels, placed in front of the iron return yoke. As the central region of the HB has the lowest material thickness with regard to the trajectory of the hadrons, for the central HO wheel two layers of scintillator tiles surround an absorber (iron). The other four wheels are made of scintillator only, using the solenoid coil as absorber. The segmentation and readout of the HO reflects the HB's tower structure, in order to form combined HCAL towers. Considering all contributions from ECAL, HCAL, the solenoid, support structure and the first layer of the iron return yoke, a minimum material thickness of  $11.8 \cdot \lambda_I$  is achieved.
- **HCAL Endcaps (HE).** They cover a range of  $1.3 < |\eta| < 3.0$  and basically work the same way as the HB. As in the HB, scintillator tiles are being read out collectively as HCAL towers. Their granularity decreases from  $\Delta\phi = 5^\circ$  and  $\Delta\eta = 0.087$  for  $|\eta| < 1.6$  to  $\Delta\phi = 10^\circ$  and  $\Delta\eta = 0.17$  for  $|\eta| > 1.6$ . Together with the ECAL, the total material thickness is about  $10 \cdot \lambda_I$ .

## 2. The CMS Experiment at the LHC

- **HCAL Forward region (HF).** It covers a range of  $2.9 < |\eta| < 5.2$ , which is not covered by any other detector part. To handle the very high particle fluxes in the forward region of the detector, the design of the HF has to be quite different from the rest of the HCAL. Radiation tolerant quartz fibres are embedded in a  $10 \cdot \lambda_I$  long steel absorber. The charged shower particles generate Cherenkov light within the fibres, which are bundled into towers of about  $\Delta\phi = 10^\circ$  and  $\Delta\eta = 0.175$ .

Together, the components of the HCAL cover a range of  $|\eta| < 5.2$ , which is illustrated in Fig. 2.20, and only a small range of  $< 0.7^\circ$  around the beam direction remains uncovered.

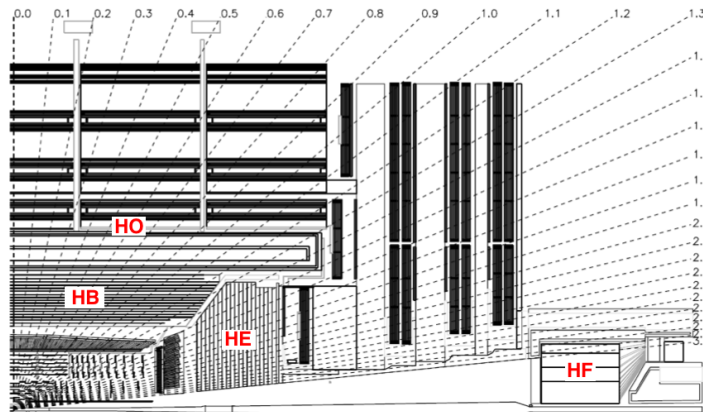


Figure 2.20: Longitudinal view of one quarter of the HCAL subsystem.

### 2.2.5 The Muon System

The presence of the term "Muon" in the name of the experiment underlines the importance given to the detection of this kind of particles in CMS. Muons are characterized by a great penetrating power, so they can easily go through the calorimeters and are easy to detect being charged particles. Moreover many of the interesting physical processes in the LHC program are characterized by final states which will involve the presence of high  $p_T$  muons. Hence a robust and redundant muon spectrometer is needed to provide precise muon identification, high resolution  $p_T$  measurements and effective trigger capabilities.

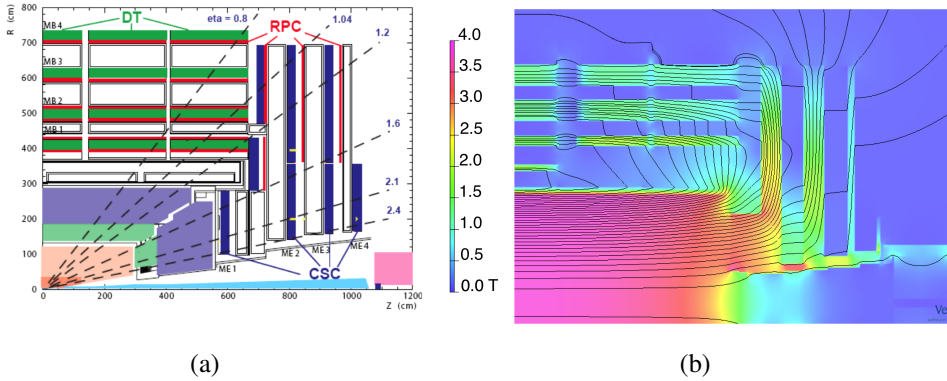


Figure 2.21: *Longitudinal view of on quarter of the CMS detector. In (a) are shown the various system composing the CMS muons spectrometer, while in (b) are reported the value for the magnetic field in the same regions as calculated by the Tosca [44] simulation.*

The muon system [45] is the outermost group of subdetectors of the CMS experiment, it covers an  $\eta$  region up to 2.4 and is located in the iron yoke for the return of the magnetic field, as shown in Fig. 2.21. It consists of three different types of gaseous detectors, chosen in function of the large surface to be covered, and whose design is driven by the differences in the radiation environment and magnetic field at different values of  $\eta$ . Drift Tubes Chambers (DTs) are used in the barrel (up to  $|\eta| < 1.2$ ) where low track occupancy and residual magnetic field are expected. The endcaps ( $0.8 < |\eta| < 2.4$ ) are instead equipped with Cathode Strip Chambers (CSCs), chosen to cope with the high particle flux and non uniformity of the magnetic field at large  $\eta$ .

In order to ensure redundancy and improve trigger capabilities, Resistive Plate Chambers (RPCs) complement DT and CSC based detectors, both in barrel and endcaps, covering an  $\eta$  region up to 2.1. RPCs allow only coarse spatial resolution measurements, however they are characterized by fast response and their excellent time resolution provides unambiguous BX identification to the muon trigger. For muons up to  $p_T \approx 200 \text{ GeV}/c$  the system resolution is limited by the multiple scattering of the particle before reaching the first spectrometer station, at higher  $p_T$  the precision of the chamber measurements dominates thanks to the larger bending radius.

The resolution is directly proportional to the square root of the amount of ma-

## 2. The CMS Experiment at the LHC

---

material in the muon system in units of  $X_0$  (radiation length) and inversely proportional to the magnetic field. For high  $p_T$  ( $\sim 1\text{TeV}/c$ ) the momentum resolution is proportional to the spatial resolution of the muon chambers. Up to the last muon station the thickness of the absorber is 16 interaction lengths.

Good muon identification is achieved by absorption of charged particles before the muon system in ECAL and HCAL, and in the muon system by the iron yoke. Moreover, the muon system is able to measure the charge of the muons up to about 1 TeV. The muon system can withstand the harsh radiation environment produced by high rate interactions.

An important issue for the muon system is its alignment, both internally and with respect to the inner tracker. The misalignment originates from imperfect assembly, temperature instabilities or deformations related to the magnetic field. It is important to monitor the alignment, as the measurement of muons is based on the combination on data from muon chambers and from the tracker.

### Drift Tubes chambers

The Drift Tubes (DT) are used for the barrel of the CMS muon system because of the large dimensions of the surface to be covered. The CMS regions inside the return yoke of the magnet have the lowest particle rate and radiation doses. The DT system is segmented in 5 wheels along the  $z$  direction, each about 2.5 m wide and divided into 12 azimuthal sectors, covering  $\sim 30^\circ$  each. Drift tubes are arranged in 4 concentric cylinders - called stations - within each wheel, at different distances from the interaction point, and interleaved with the iron of the yoke.

Each station consists of 12 chambers, with the exception of the outermost station MB4, whose top and bottom sectors are equipped by two chambers each (instead of only one), thus yielding a total of 14 chambers in that station. The overall CMS detector is thus equipped with a total of 250 DT chambers. The dimensions of each chamber are station-dependent. Each chamber is azimuthally staggered with respect to the preceding inner one, in order to maximize the geometrical acceptance.

The basic detector element of the DT muon system is a drift tube cell, whose section is shown in Fig. 2.22(a). The dimensions of a cell are  $42\text{mm} \times 13\text{mm}$  and it has a stainless steel anode wire with diameter  $50\mu\text{m}$  and length varying from

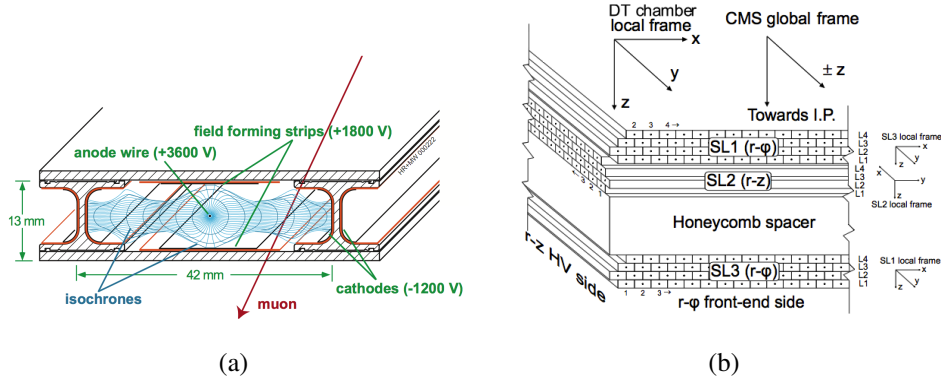


Figure 2.22: In (a) transverse view of a drift tube cell, with drift lines and isochrones for a typical voltage configuration of the electrodes. In (b) Cross-section of a barrel muon chamber with the local and global reference frames.

2 to 4 m. A layer of cells is obtained by two parallel aluminum planes within which a series of I-shaped aluminum beams - 1.2 mm thick and 9.6 mm high - define the boundaries among adjacent cells. Aluminum strips, deposited on either faces of each I-beam and electrically isolated from the I-beam body using Mylar tape, serve as cathodes. Anode wires and cathodes are put at positive and negative voltage (+3600 V, -1800 V) respectively, and provide the electric field within the cell volume.

The distance of the traversing track to the wire is measured by the drift time of ionization electrons; for this purpose, two additional positively-biased strips are mounted on the aluminum planes (with an insulator in between) on both inner surfaces in the center of the cell itself, just in correspondence of the anode wire, in order to provide additional field shaping to improve the space-to-distance linearity over the cell (which is crucial for triggering purposes). Typical voltages are +3600 V, +1800 V and -1800 V for wires, strips and cathodes respectively. The tubes are filled with a 80%/20% gas mixture of  $Ar/CO_2$ , which provides good quenching properties.

A cross-sectional view of a muon chamber is shown in Fig 2.22(b). Each muon station is instrumented in the transverse plane and in the longitudinal  $\theta - z$  plane. The drift cells are assembled in layers, the number of cells depending on the chamber dimensions. Four layers are assembled together to form a quadruplet called superlayer (SL), with neighbouring planes staggered by half a tube,

## 2. The CMS Experiment at the LHC

allowing to resolve the left-right ambiguity of a single layer. Each DT station is composed of 3 superlayers, two of which are devoted to the position measurement in the bending plane  $r - \phi$  (the wires are parallel to the beam line), and one to the measurement of the  $z$ -coordinate in the longitudinal plane  $\theta - z$  (the wires are disposed orthogonally to the  $z$  direction). The only exception is the outermost station MB4, which lacks the SL in the  $\theta - view$ . In addition, a 128 mm thick honeycomb plate, acting as a rigid but light spacer, is inserted between the inner  $\phi - view$  SL and the outer ones. It increases the lever-arm in the bending plane, thus improving the angular resolution.

### Cathode Strip Chambers

In the two endcap regions of CMS, where the muon rates and background levels are high and the magnetic field is large and non-uniform, the muon system uses Cathode Strip Chambers. CSC chambers are multi-wire proportional chambers with fast response time, fine segmentation, and radiation resistance, so that they can operate at high occupancy levels and in the presence of a large inhomogeneous magnetic field. CSC chambers identify muons between  $|\eta|$  values of 0.9 and 2.4, and are arranged in four stations placed between the iron disks of the yoke. The innermost station consists of three concentric rings, the first (ME1/1) being closer to the interaction point than the other two. The other stations are composed by two disks only.

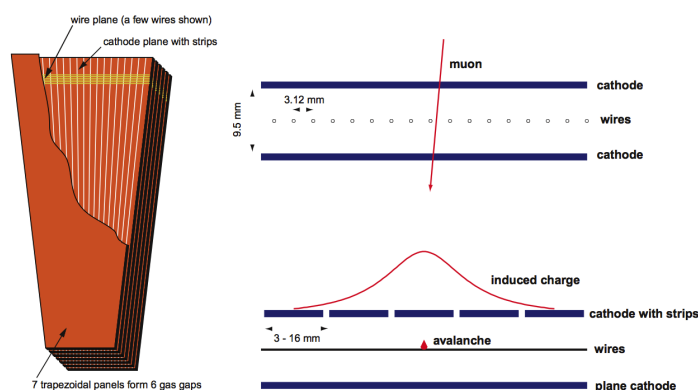


Figure 2.23: Schematic representation of a CSC chamber (left), and of the effect of a traversing muon in one gap (right).

The rings are formed by 18 or 36 trapezoidal chambers, which, with the exception of the outermost ring of ME1, are staggered with a small overlap in  $\phi$ . Chambers are composed of six layers, each consisting of an array of anode wires between two cathode planes, as sketched in Fig. 2.23. The gap is 9.5 mm thick and is filled with a 30%/50%/20% mixture of  $Ar/CO_2/CF_4$ . One of the two cathode planes is segmented into strips orthogonal to the wires.

The avalanche produced in the gap by a crossing charged particle induces a charge in several adjacent strips, an interpolation of the signals gives a precise spatial measurement. Strips are radial and measure the  $\phi$  coordinate. The orthogonal coordinate ( $r$ ) is measured by the wires which, to reduce the number of channels, are read out in groups of 5 to 16. The resolution is of the order of  $\sim 0.5\text{cm}$ , to be compared with  $\sim 150\mu\text{m}$  of the strip measurement.

### Resistive Plate Chambers

For improving the ability of muon system trigger and measuring the correct beam crossing time when the LHC reaches full luminosity, a complementary, dedicated trigger system consisting of resistive plate chambers (RPC) was added in both the barrel and endcap regions. The RPCs provide a fast, independent, and highly-segmented trigger with a sharp  $p_T$  threshold over a large portion of the rapidity range ( $|\eta| < 1.6$ ) of the muon system.

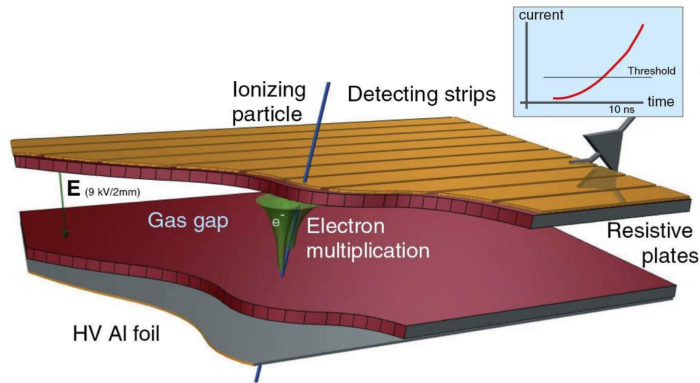


Figure 2.24: Graphical representation of an RPC gap.

The RPCs are double-gap chambers, operated in avalanche mode to ensure good operation at high rates (in Fig. 2.24 a graphical representation of its op-

eration). They produce a fast response, with good time resolution but coarser position resolution than the DTs or CSCs. They also help to resolve ambiguities in attempting to make tracks from multiple hits in a chamber.

A total of 6 layers of RPCs are embedded in the barrel muon system, 2 in each of the first 2 stations, and 1 in each of the last 2 stations. The redundancy in the first 2 stations allows the trigger algorithm to work even for low- $p_T$  tracks that may stop before reaching the outer 2 stations. In the endcap region, there is a plane of RPCs in each of the first 3 stations in order for the trigger to use the coincidences between stations to reduce background, to improve the time resolution for bunch crossing identification, and to achieve a good  $p_T$  resolution.

### 2.2.6 CMS Trigger System

When running at its design luminosity, the LHC will deliver bunch crossings every 25 ns, each causing about 20 particle interactions. Most of these events are soft, i.e. no high  $p_T$  particles are produced during the collision. Storing the data of all of these events is neither practicable with today's technology nor necessary. In order to select only interesting events and thus to reduce the event rate which has to be processed, a trigger system has been developed for CMS. It consists of two logic stages (Fig. 2.25).

- The Level 1 triggers (L1 [46]) are hardware based online triggers, meaning that they decide whether to save the events or not, directly after they have been recorded by the detector. In fact, the decision has to be made within 3  $\mu s$  after each collision, because the data saved in the buffer are overwritten after this period. The L1 triggers lead to a reduction of the event rate from 40 MHz to 100 kHz, which is low enough to be saved and transferred to a computer farm.
- Events passing the L1 trigger are processed by the second stage of the trigger system, the High Level Trigger (HLT [47]). It is a software based offline trigger, that has more time for making decisions. Thus, it can use reconstruction algorithms to further reduce the event rates. Only permanently storing events that at least passed one HLT criteria, leads to a reduction of

the event rate from 100 kHz to a few hundred Hz, which corresponds to the manageable rate  $\sim 100$  MB/s to be stored on tape.

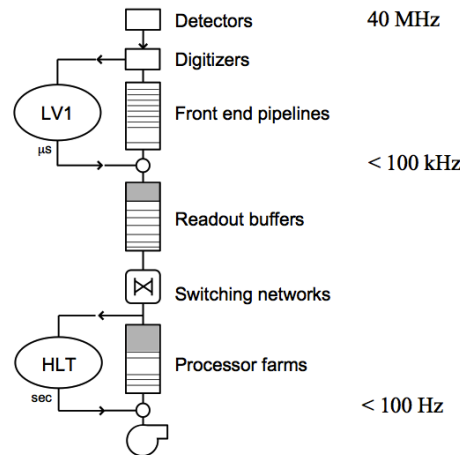


Figure 2.25: Data flow in the CMS Trigger system. Two consecutive processing stages are implemented: level-1 and High Level Triggers.

Different triggers exist for each of the trigger stages, which are specialised for finding special event types. L1 trigger is organized into three major parts: the L1 calorimeter trigger, the L1 muon trigger, and the L1 global trigger. For sub-L1-systems, the calorimeter trigger preserves the tower energy sums from the ECAL, HCAL and HF individual cells (or towers) and reconstructed candidates of electrons, photons, taus and jets. Thresholds are added on these particle candidates.

According to design, for instance, the transverse missing energy trigger requires the events with MET (Transverse Missing Energy) greater than 100 GeV, but at the very first low luminosity this trigger was not enabled. The muon sub-trigger focuses on  $\mu$  preselection. Information from DT, CSC and RPC is used to drop events with low quality muons. The global muon trigger converts muon tracks from different chambers into the same  $\eta, \phi$  and  $p_T$  scale, then to correlate the tracks.

Another important task for global muon trigger is to identify whether the muon is isolated or not via vetoing the event with an  $\eta - \phi$  grid of noisy calorimeter towers. The global L1-subtrigger holds a time match on these information from both

## 2. The CMS Experiment at the LHC

---

calorimeter and muon chambers, and decides to accept or reject each bunch crossing based on the programmed logical combination. The CMS data acquisition system processes events accepted by the first-level trigger at a maximum input rate of a few 100 kHz. Event data are read out from the detector and stored in readout buffers at a total rate of 1 Terabit/s. The event-builder then assembles event fragments into full events employing a large switching network.

The high-level trigger algorithms run on a farm of commercial processors. Each event is processed by a single processor, which has access to the full raw event data. High level-trigger reconstruction code will be as close as possible to the full offline analysis code, the main differences resulting from limited processing time and the possible lack of precise calibration constants. The following three key features of HLT software guarantee minimal processing time:

- *Reconstruction on demand.* Trigger objects are only reconstructed if needed in the trigger decision. Unnecessary calculations are avoided by rejecting events as early as possible using fast algorithms. The reconstruction and selection therefore take place in several stages (virtual trigger levels), which roughly correspond to the functions of traditional second and third trigger levels. There is no limitation to the number of virtual trigger levels or to the algorithms employed except for CPU time. For historic reasons the terminology Level- 2 is used for a first high-level trigger stage based on data from the muon systems and calorimeters while Level-3 refers to algorithms including tracker data.
- *Partial/Region reconstruction:* only parts of detector information are analysed guided by the trigger objects found in the preceding trigger levels.
- *Conditional reconstruction.* Reconstruction is aborted if further calculations would not alter the result (for example when reconstructing additional tracks in an isolation algorithm) or if the condition arises that resulting trigger object would not be relevant to the trigger decision.

HLT available algorithm changed a lot since the startup, in order to follow the luminosity delivered by LHC. Events that have passed the HLT reach the CERN Tier 0 (Section 2.1.5) for the reconstruction and are then distributed on the GRID for an easy access for all the CSM collaboration.

# Chapter 3

## The CMS software

The goal of this chapter is to describe the software used for the analysis described in this thesis. It is aimed to process the electric deposits in the various CMS subdetectors to obtain the reconstructed physics object.

This is done by a dedicated software framework named CMSSW [48]. It consists of over a thousand subpackages which have been created to provide an extensive toolkit for users to carry out analyses on data and perform other software-related tasks. A schematic overview of the software framework is given in Fig. 3.1. The CMS Event Data Model (EDM) is centred around the concept of Event. An Event is a C++ object container for all RAW and reconstructed data related to a particular collision. During processing, data are passed from one module to the next via the Event, and are accessed only through the Event.

In software terms, an Event starts as a collection of the RAW data from a detector or MC event, stored as a single entity in memory, a C++ type-safe container called `edm::Event`. Any C++ class can be placed in an Event, there is no requirement on inheritance from a common base class.

As the event data is processed, products (of producer modules) are stored in the Event as reconstructed (RECO) data objects. The Event also contains meta-data describing the conditions and calibration data used for reconstruction of each contained object.

All objects in the Event may be individually or collectively stored in ROOT files. Products in an Event are stored in separate containers, organizational units within an Event used to collect particular types of data separately. There are parti-

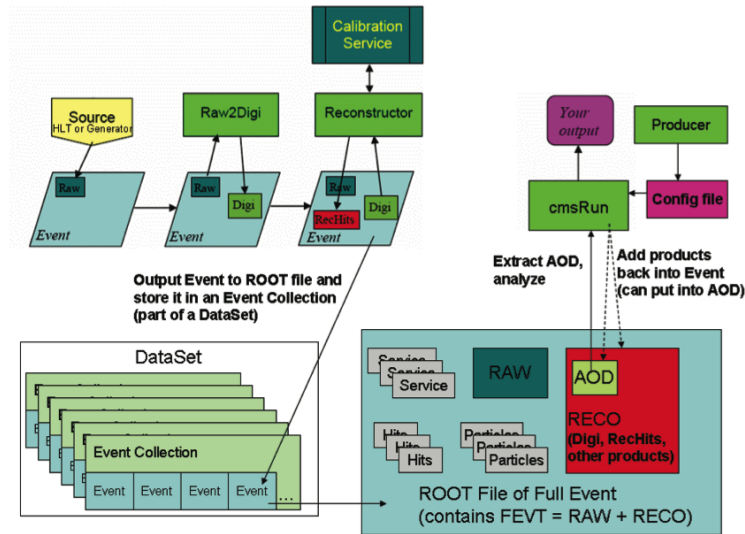


Figure 3.1: A schematic overview of the software framework.

cle containers (one per particle), hit containers (one per subdetector), and service containers for things like “provenance tracking”.

The full event data (FEVT) in an Event is the RAW plus the RECO data. Analysis Object Data (AOD) is a subset of the RECO data in an event; AOD alone is sufficient for most types of physics analysis.

The present analysis has been written in the CMSSW framework. The studies are performed on the AOD type collections of real data and simulated Monte Carlo data. The latter have been produced by dedicated packages, described in the next paragraph, in the same version of framework used for the analysis .

With respect to the real data, which are acquired and reconstructed, the Monte Carlo events have to be *generated* and the passage through all the CMS subdetectors has to be *simulated*, before going to the *reconstruction* step.

### 3.1 Event Generation

In high energy experiments various Monte Carlo (MC) generators are used to produce simulated events, which are then reconstructed and compared with real data.

Usually the Standard Model and MSSM samples are produced with the CTEQ6L [49] set of parton distribution functions by different event generators, depending on the considered process. These predicted cross sections and their uncertainties at NLO and NNLO are calculated by the LHC experiments with the 7 TeV data in deep-inelastic scattering, Drell-Yan and jet processes. Concerning the generators, they are not specific for each experiment but for the final states or the topologies that are able to generate. The more common are PYTHIA 6 [50], Evtgen [51], POWHEG [52] and Madgraph [53].

## 3.2 Simulation

After the generation the events are processed through a full GEANT4 [54, 55] detector simulation and trigger emulation. This is referred as *simulation*. It is aimed to reproduce all that happens when a particle passes through the detector. Therefore an accurate description of the detector geometry is needed, and each process that characterizes the real data-taking has to be taken into account: electronic noise, dead time, PU effects, etc.

In order to reproduce the phenomenology of the particle-matter interaction in the active and passive detector layers, the complete CMS detector is simulated considering one by one all the subdetectors and their geometry, in turn simulated by specific algorithms. When processes as decays, bremsstrahlung, nuclear interactions, multiple scattering, pair production, etc are simulated, the result is a collection of analogue signals for each subdetector. These collections, as in the real acquisition, are processed by the trigger algorithms: the effect of L1 trigger (hardware) is simulated, and, for the events that survive, the digitization and the HLT are emulated. The result is a RAW events collection.

## 3.3 Reconstruction

The reconstruction phase is aimed to produce high level physics objects. In practice, starting from RAW data, event by event, RECO data are obtained. These consist in collections of particles as electrons, muons, photons, charged and neutral hadrons, and more complex objects as jets, and *tau*-jets. At this level also the

missing transverse energy (MET or  $E_T^{miss}$ ) of the event is computed.

The reconstruction is performed by the Rec-Units, that work independently in each subdetector. In general each of them starts with a partial reconstruction of the objects. Cluster in the calorimeters, segments in tracker and in the muon system are created. These local informations are used to reconstruct the *global tracks* and the *primary* and *secondary vertices* for each event. In the end, a set of sophisticated algorithms, putting these informations together, perform the particle identification. A tree-scheme of this procedure is shown in figure 3.2. Further

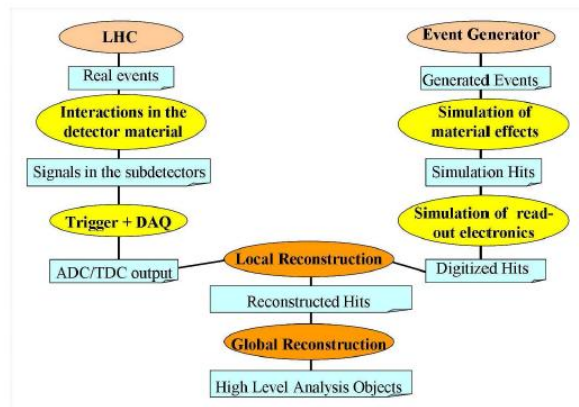


Figure 3.2: A schematic overview of the software for the events generation and reconstruction.

sophisticated algorithms are used to create a so called Particle Flow (PF) reconstruction, described in the following sections.

In the search for MSSM Higgs in two muons, objects reconstructed by PF algorithms are used: muons, jets and  $E_T^{miss}$ , as illustrated below.

#### 3.3.1 Iterative Tracking reconstruction

The CMS tracking software [56] is implemented in CMSSW and is known as the ‘Combinatorial Track Finder’ (CTF). Before this standard track reconstruction sequence begins, a fast pixel-only track and vertex reconstruction step is run in

order to locate the primary vertices in the event. Pixel hits from at least three layers are found and fit using a fast pattern recognition and helix fitter [57]. These pixel standalone tracks are used both in the on-line, high-level trigger, and in the full general tracking. In the high level trigger, this information is used for b-hadron tagging,  $\tau$ -lepton tagging, and to help calculate calorimetric isolation quantities.

In CMS, the standard track collection is derived from multiple passes of the track reconstruction sequence in a process called *iterative tracking* [58]. The basic philosophy of iterative tracking is that by removing the hits associated with already found tracks, it is possible to find additional tracks by reducing the combinatorics and relaxing the selection criteria. Each iteration is designed to find a particular class of tracks and the number and configurations are frequently changed accordingly with the LHC operation. At the beginning of each iteration, hits already used to produce a good quality track in the previous iterations are masked off.

Each reconstruction iteration proceeds in four steps:

- The seed generation provides initial track candidates using only a few hits, like 2 or 3. A seed defines the initial trajectory parameters and uncertainties.
- The track finding is based on a global Kalman filter [59] and extends the seeds to find other hits on a potential track, corresponding to the trajectory taken by a charged particle.
- The final track fitting module is used to provide the best possible estimate of the parameters of the trajectories by means of a Kalman filter and smoother.
- The final track selection sets quality flags and discards tracks which fail certain criteria.

The main differences in the configuration of the iterations are the seed generation and final track selection.

### Seed generation

The trajectory seeds define the starting trajectory parameters and uncertainties of potential tracks. In the uniform magnetic field present where the track develops, charged particles follow helices and therefore five parameters (including the

trajectory curvature) are needed to define a starting trajectory. To obtain these five parameters requires at least 3 hits, or 2 hits and a beam constraint. To limit the hit combinations, seeds are required to satisfy loose criteria such as minimum transverse momentum and consistency with originating from the proton-proton interactions region.

Seeds are constructed starting from the pixel layer because granularity of the pixel detector ensures that the average occupancy of the inner pixel layer is much less than the average occupancy of the outer strip layer (Fig. 3.3) and to maintain high efficiency.

In fact due to the mass of the Tracker, many particles produced in LHC collisions suffer destructive interactions before exiting the Tracker. Although most high  $p_T$  muons traverse the entire Tracker, between 5% and 15% of the produced pions interact inelastically in the Tracker (Fig. 3.4). In addition, many electrons lose a significant fraction of their energy due to bremsstrahlung radiation in the Tracker.

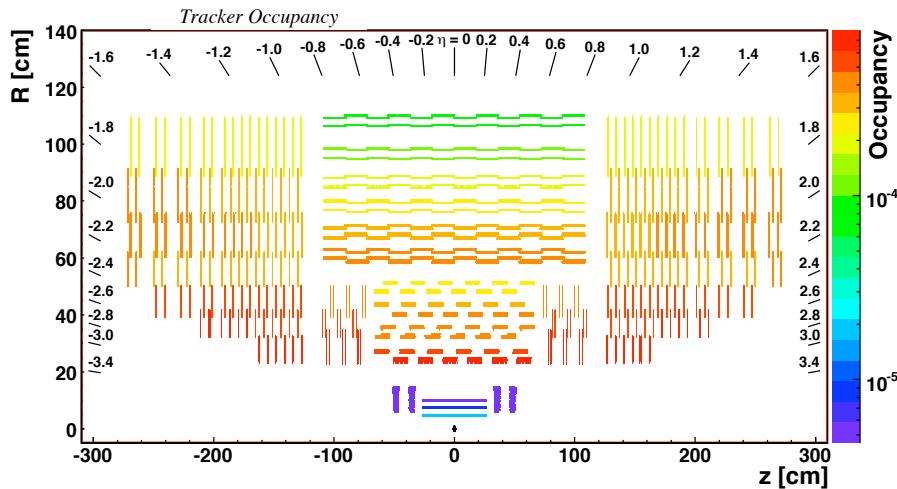


Figure 3.3: Occupancy of the Silicon Tracker detectors for Minimum Bias events simulated with superimposed pile-up collisions. The pseudorapidity values are also indicated in figure.

More than 90% of charged particles produced in LHC collisions inside the geometrical acceptance of the Tracker cross 3 pixel layers and therefore can be

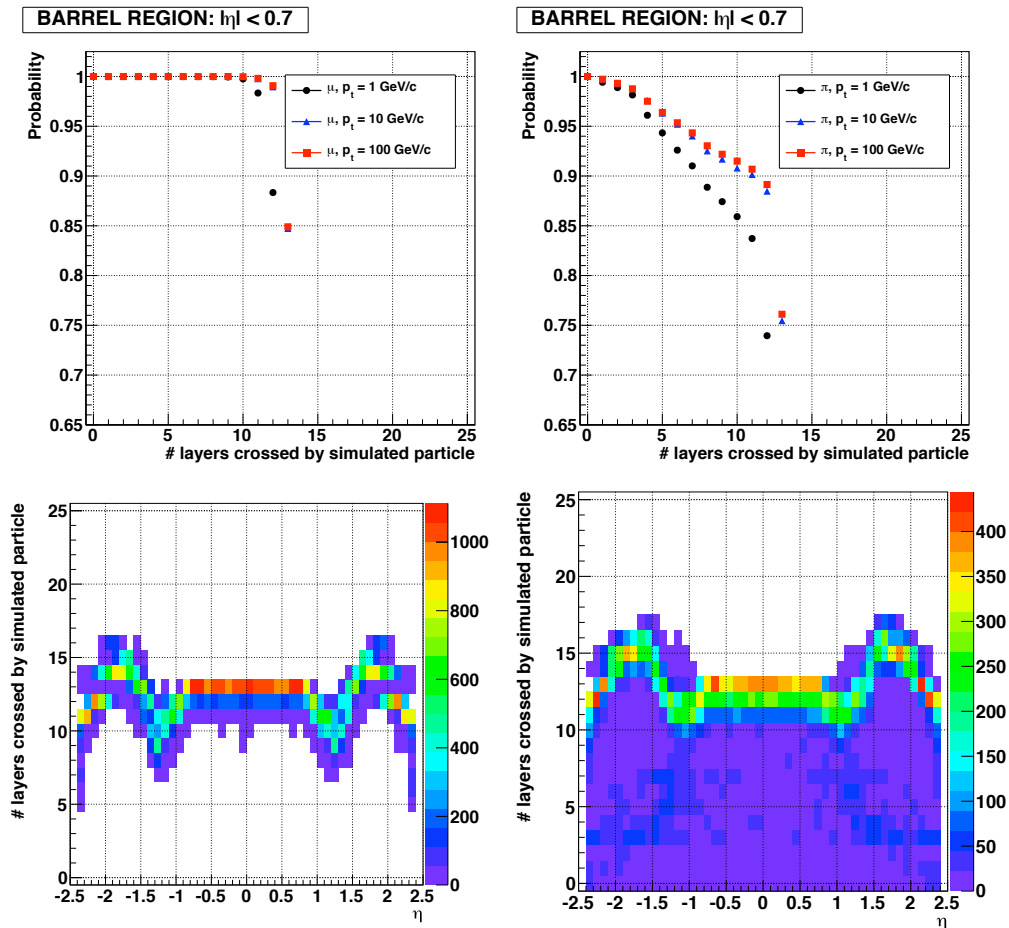


Figure 3.4: The top plots show the probability that muons (left) and pions (right) of different momenta are not absorbed by the detector material as a function of the number of Tracker layers crossed in the barrel region. The bottom plots show the number of crossed layers versus pseudorapidity for muons (left) and pions (right) with transverse momentum equal to 10 (1) GeV/c [56].

reconstructed starting from trajectory seeds obtained from triplets of pixel hits. To recover inefficiencies in the pixel detector (from gaps in coverage, non-functioning modules, and saturation of the readout) and to reconstruct particles not originating directly from the proton-proton collisions other kind of seeds are created using mixing information with that coming from the strip detector.

#### Track Finding

The track finding module of the CTF algorithm is based on the Kalman filter method. The filter proceeds iteratively from the seed layer, starting from a coarse estimate of the track parameters provided by the trajectory seed, and includes the information of the successive detection layers one by one. The information provided at each layer includes the location and uncertainty of any found hit as well as the amount of material crossed which is used to estimate the uncertainty arising from multiple Coulomb scattering. Each iteration of the Kalman filter is implemented in four steps.

The first step, navigation, uses the parameters of the track candidate, evaluated at the current layer, to determine which adjacent layer(s) of the tracking detector would be intersected by the extrapolated trajectory, allowing for the current uncertainty on that trajectory.

The second step is a search for compatible *detectors* on the layers returned by the navigation step.

The third step forms groups of hits, obtained by collecting all the hits from each detector.

The fourth and last step is to update the trajectory state. One or more new track candidates are formed from each of the original ones, by adding to them exactly one of the compatible hits from each detector grouping (where this hit may be the invalid hit). The candidate's trajectory parameters are then updated at the new detector surface, by combining the information from the hit with the extrapolated track trajectory of the original candidate.

For the second, third and fourth steps above, a more accurate *material propagator* is used which includes the effect of the material in the Tracker. This differs from the simple analytical propagator, in that it inflates the uncertainty on the trajectory parameters according to the predicted rms scattering angle in the Tracker

material. It also adjusts the momentum of the trajectory according to the mean energy loss predicted by the Bethe-Bloch equation.

After a track candidate has completed the outward search for hits, an inward search for hits is begun. This is started by taking all of the hits assigned to the track, excluding those belonging to the track seed, and using them to make a new trajectory. Then, following the steps above, this trajectory is propagated inward through the seeding layers and then further inwards until the inside edge of the detector is reached or too many invalid hits are found.

The track of a single charged particle may be reconstructed more than once, either by starting from different seeds or when a given seed develops into more than one track candidate. To fix this feature, a “trajectory cleaner” is applied after all the track candidates in a given iteration have been found. The trajectory cleaner calculates the fraction of shared hits between two track candidates:

$$f_{shared} = \frac{N_{shared}^{hits}}{\min(N_1^{hits}, N_2^{hits})} \quad (3.1)$$

where  $N_1^{hits}$  ( $N_2^{hits}$ ) is the number of hits in the first (second) track-candidate. If this fraction exceeds the (configurable) set value of 19%, the trajectory cleaner removes the track with the least number of hits; if both tracks have the same number of hits, the track with the largest  $\chi^2$  value is discarded. The procedure is repeated iteratively on all pairs of track candidates. The same algorithm is applied when tracks from the six iterations are combined into a single track collection.

### Track Fit

For each trajectory, the track finding stage results in a collection of hits and an estimate of the track parameters. However, the full information is only available at the last hit of the trajectory and the estimate can be biased by constraints applied during the seeding stage.

The Kalman filter is initialized at the location of the innermost hit with the trajectory estimate obtained during seeding. The corresponding covariance matrix is scaled up by a large factor in order to avoid any bias. The fit then proceeds in an iterative way through the full list of hits, updating the track trajectory estimate with each hit in turn. For each valid hit, the hit’s position estimate is re-evaluated using the current values of the track parameters. To obtain ultimate precision, this

filtering and smoothing procedure uses a *Runge-Kutta propagator* to extrapolate the track trajectory from one hit to the next. This not only takes into account the effect of material, but is also able to accommodate an inhomogeneous magnetic field.

Estimates of the track trajectory at other points, such as the point of closest approach to the beam-line, can be obtained by extrapolation from the trajectory evaluated at the nearest hit. This extrapolation also uses the Runge-Kutta propagator.

After filtering and smoothing, a search is made for spurious hits (*outliers*), wrongly associated to the track. These hits can be correlated with the otherwise well-defined track, e.g. if they originate from  $\delta$ -rays, or uncorrelated, such as hits from nearby tracks or electronic noise. There are two methods which are used to find outliers.

#### 3.3.2 Primary Vertex Reconstruction

The term “Primary Vertex” refers to the reconstruction of the point of the proton-proton interaction. Vertexes originated from the subsequent decay of prompt particles are referred as “Secondary Vertex”. In the primary vertex reconstruction [60], the measurements of the location and uncertainty of an interaction vertex are computed from a given set of reconstructed tracks. The prompt tracks originating from the primary interaction region are selected based on the transverse impact parameter significance with respect to the beam line (see section 3.3.2), number of strip and pixel hits, and the normalized track  $\chi^2$ . To ensure high reconstruction efficiency in the minimum bias events, there is no requirement on the track transverse momentum.

In the reconstruction of CMS data in 2009 and 2010, the selected tracks were then clustered based on their  $z$  coordinates at the point of closest approach to the beam line. Vertex candidates were formed by grouping tracks that were separated in  $z$  by less than a distance  $z_{\text{sep}}$  (typically in the range 2 mm to 1 cm) from their nearest neighbour. Small values of  $z_{\text{sep}}$  can lead to splitting tracks from one interaction into two separate vertices. However, vertices closer than  $z_{\text{sep}}$  will always be merged. This algorithm is therefore inefficient for running with multiple  $pp$  interactions per crossing.

For the reconstruction of CMS data in 2011, when pile-up becomes more relevant, tracks are clustered using a deterministic annealing (DA) algorithm [61, 62]. The  $z$ -coordinates of the points of closest approach of the tracks are referred to as  $z_i$ , and the associated uncertainty is  $\sigma_i$ . The tracks must be assigned to some unknown number of vertices at positions  $z_k$ . The assignment probability of track  $i$  to vertex  $k$  is described by  $p_{ik}$ . The procedure then finds the most likely distribution of assignments for a given  $\langle \chi^2 \rangle = \sum_{ik} p_{ik} \frac{(z_i - z_k)^2}{\sigma_i^2}$ , referred to as the ‘‘principle of maximum entropy’’.

Candidates containing at least two tracks are then fit with an adaptive vertex fit [63] to compute the best estimate of vertex parameters such as position and covariance matrix, as well as the indicators of the success of the fit, such as the number of degrees freedom of the vertex and track weights of the tracks in the vertex.

In the adaptive vertex fit, to each track in the vertex is assigned a track weight between 0 and 1 based on its compatibility with the common vertex. For a track consistent with the common vertex, its weight is close to 1. The number of degrees of freedom is defined as  $n_{\text{dof}} = 2 \sum_{i=1}^{n_{\text{Tracks}}} w_i - 3$ , where  $w_i$  is the weight of the  $i^{\text{th}}$  track. It is thus strongly correlated to the number of tracks compatible with the primary interaction region. For this reason, the number of degrees of freedom of the vertex can be used to select real proton-proton interactions.

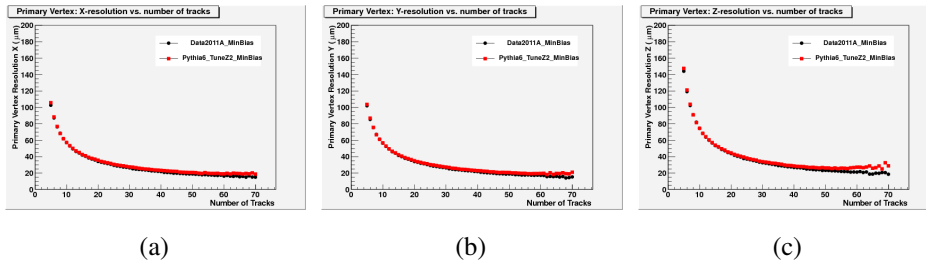


Figure 3.5: Primary vertex resolution in  $x$  (a),  $y$  (b), and  $z$  (c) as a function of the number of tracks used in the fitted vertex [56]. The Pythia8 Tune 1 is used in the simulation.

The primary vertex resolution depends strongly on the number of tracks used in fitting the vertex and the  $p_T$  of those tracks. It’s also of great importance to have a good vertex resolution in particular for estimating the life-time of long

lived prompt particles, like the b-mesons, which is done by measuring the distance between primary and secondary vertexes. In order to measure in a data sample the resolution as a function of the number of tracks in the vertex a method as been developed, called *split method*.

The tracks used in the vertex in an event are split evenly into two different sets. During the splitting procedure, the tracks are ordered in descending order of  $p_T$  first and then grouped in pairs starting from the track with largest  $p_T$ . In each pair, tracks are randomly assigned to one or the other track set. This procedure ensures that the two split track sets have the same kinematic distributions on average. These two different track sets are then fitted independently with the adaptive vertex fitter. The distributions of the difference in the fitted vertex positions for a given number of tracks are fit with a single Gaussian distribution to extract the resolution.

Fig. 3.5 shows the measured primary vertex resolutions in  $x$  (a),  $y$  (b), and  $z$  (c) as a function of the number of tracks. Results are shown for both minimum-bias-triggered data and simulation and a good agreement in the curves is seen. The resolutions in  $x$  and  $y$  are observed to be consistent. For minimum bias events, the resolutions in  $x(y)$  and  $z$  are found to be below  $20\mu m$  and  $25\mu m$  for the primary vertexes using more than 50 tracks.

In order to estimate the vertex reconstruction efficiency given a set of tracks clustered in  $z$  which forms a reconstructed vertex, it's checked how often its position is consistent with the true value. Similar to the primary vertex resolution, the primary vertex efficiency also strongly depends on the number of tracks in the cluster. The split method can be used to measure the primary vertex reconstruction efficiency as a function of the number of tracks in the cluster. Fig. 3.6 shows the measured primary vertex efficiency as a function of the number of tracks that are clustered in  $z$ . The results obtained using the split method described above are applied to both data and simulation and good agreement between the two is observed. The primary vertex efficiency is estimated to be close to 100% if there are more than two tracks with transverse momenta greater than 0.5 GeV/c in the vertex.

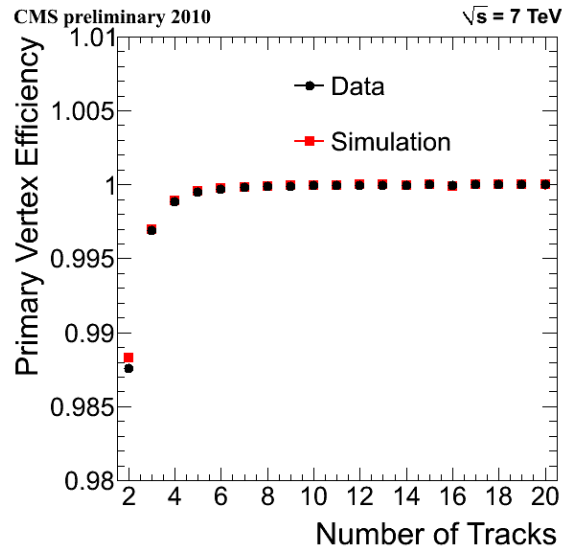


Figure 3.6: Primary vertex efficiency as a function of the number of tracks in a cluster [56].

### Reconstruction of the LHC Beam Line

The beam line (referred also as *beamspot*) represents the three-dimensional profile of the luminous region where the LHC beams collide at CMS. The beam line is determined in an average over many events, in contrast to the event-by-event primary vertex which gives the precise position of a single collision. A good measurement of the position and slope of the beam line is an important component of the event reconstruction. The beam line position can be used, especially in the high level trigger, as an estimate of the primary interaction point prior to the reconstruction of the primary vertex and even as the primary interaction point in low multiplicity data. This position can be determined in two ways. The first is through the reconstruction of primary vertexes. The reconstructed vertexes map out the collisions and thus the shape of the beam line. The mean position in  $x$ ,  $y$ , and  $z$  can be determined from a likelihood fit to the 3D distribution of vertexes.

The second method exploits a correlation between the transverse impact parameter ( $d_{xy}$ ) and the azimuthal angle of tracks ( $\phi_0$ ) that exists when the beam line is displaced from the expected position. To first order the  $d_{xy}$  for tracks coming

from the primary vertex can be parametrized by

$$d_{xy}(\phi_0, z) = x_0 \cdot \sin \phi_0 + \frac{dx}{dz} \cdot \sin \phi_0 \cdot z - y_0 \cdot \cos \phi_0 - \frac{dy}{dz} \cdot \cos \phi_0 \cdot z, \quad (3.2)$$

where  $x_0$  and  $y_0$  are the position of the beam at  $z = 0$ , and  $\frac{dx}{dz}$  and  $\frac{dy}{dz}$  are the  $x$  and  $y$  slopes of the beam. The beam line fit [64] uses an iterative  $\chi^2$  fit to exploit this correlation between  $d_{xy}$  and  $\phi_0$ . With a sample of 1000 tracks, the position can be determined with a statistical precision of  $\sim 5 \mu\text{m}$ .

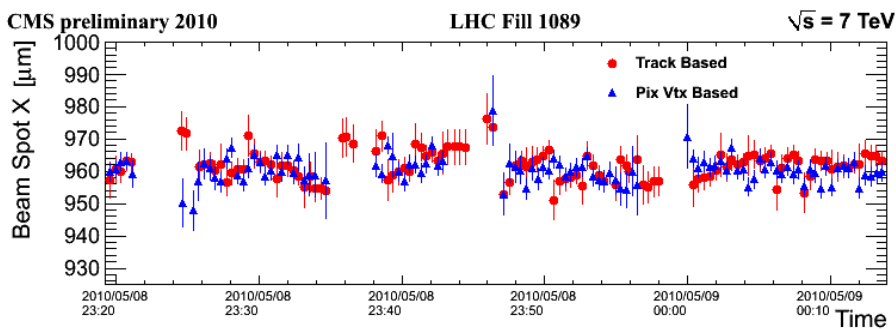


Figure 3.7: *Fitted  $x_0$  positions of the beam line as a function of time during an LHC fill where a luminosity scan was performed [56].*

Figure 3.7 shows the fitted positions as a function of time during one part of one fill in which LHC performed a luminosity scan. While the beam position is normally stable, during this scan the position in  $y$  was adjusted by LHC operators during the fill. No points are plotted where an insufficient number of tracks or vertexes were reconstructed to fit the beam line. The plots show that the two methods give consistent results and CMS is able to track well the movements of the beam.

### 3.3.3 Muon reconstruction

In Section 3.3.1 the charged tracks reconstruction in the central tracker has been described. In the charged tracks also muons are included, which then can reach the muon chamber in the return yoke of the magnetic field. In the standard CMS reconstruction for pp collisions [65, 66], tracks are first reconstructed

independently in the silicon tracker (*tracker track*) and in the muon spectrometer (*standalone-muon track*). Based on these, two reconstruction approaches are used:

1. *Global Muon reconstruction (outside-in)*. Starting from a standalone muon in the muon system, a matching tracker track is found and a *global-muon track* is fitted combining hits from the tracker track and standalone-muon track. At large transverse momenta ( $p_T \gtrsim 200 \text{ GeV}/c$ ), the global-muon fit can improve the momentum resolution compared to the tracker-only fit [65, 66].
2. *Tracker Muon reconstruction (inside-out)*. In this approach, all tracker tracks with  $p_T > 0.5 \text{ GeV}/c$  and  $p > 2.5 \text{ GeV}/c$  are considered as possible muon candidates and are extrapolated to the muon system, taking into account the expected energy loss and the uncertainty due to multiple scattering. If at least one muon segment (i.e. a short track stub made of DT or CSC hits) matches the extrapolated track, the corresponding tracker track qualifies as a *tracker-muon track*. The extrapolated track and the segment are considered to be matched if the distance between them in local  $x$  is less than 3 cm or if the value of the pull for local  $x$  is less than 4. At low momentum (roughly  $p < 5 \text{ GeV}/c$ ) this approach is more efficient than the global muon reconstruction, since it requires only a single muon segment in the muon system, whereas global muon reconstruction is designed to have high efficiency for muons penetrating through more than one muon station.

The majority of muons from collisions (with sufficient momentum) are reconstructed either as a Global Muon or a Tracker Muon, or very often as both. However, if both approaches fail and only a *standalone-muon track* is found, this track is also added to the general collection of muons (and classified as Standalone-muon), even if muons of this kind are not usually used in the physics analyses.

The final result is a single collection of muon candidates, each one containing information from the standalone, tracker, and global fit, when available. Candidates found both by the Tracker Muon and the Global Muon approach that share the same tracker track are merged into a single candidate. Similarly, standalone-muon tracks not included in a Global Muon are merged with a Tracker Muon if they share a muon segment.

The combination of different algorithms provides a robust and efficient muon reconstruction. A given physics analysis can achieve the desired balance between identification efficiency and purity by applying a selection based on the muon identification variables. The default algorithm for muon momentum assignment, dubbed the “sigma-switch”, chooses the global fit if both the global and tracker-only fit estimate the muon transverse momentum ( $p_T$ ) to be above 200 GeV/c and if the results of the two fits for  $q/p$  agree to within two sigma of the tracker-only fit, otherwise it chooses the tracker-only fit.

#### **Muons reconstruction in the Inner Tracker**

Muons are the charged particles that are best reconstructed in the Tracker. They mainly interact with the silicon detector through ionization and their energy loss by bremsstrahlung is generally negligible, except when muons are produced with an initial energy higher than about 100 GeV. Therefore these particles usually cross the whole volume of the tracking system, producing detectable hits on *all* the sensitive layers of the apparatus. Finally, muon trajectories are scattered exclusively by Coulomb scattering, whose effects are straightforward to include inside the Kalman filter formalism. For isolated muons with a transverse momentum between 1 GeV/c and 100 GeV/c, the tracking efficiency is higher than 99% in the full  $\eta$ -range of the Tracker acceptance and the efficiency does not depend on the transverse momentum of the particles.

The average hit-finding efficiency (Fig. 3.8(a)) is higher than 99% both in the barrel and in the endcaps; it is still above 97% in the barrel-transition region where the layer navigation is more complicated and the material budget of the Tracker is more significant. The trajectory contamination due to spurious hits produced by electrical noise or  $\delta$ -rays is of the order of  $10^{-3}$  (Fig. 3.8(b)).

#### **Muon Reconstruction in the Muon Spectrometer**

The basic element to construct a muon track in the muon systems is the result of the local reconstruction [67]. Its goal is the reconstruction of basic hits and segments in individual muon chambers, starting from the output of the Data Acquisition system. Different implementations are used to reflect the hardware differences in the 3 types of chambers:

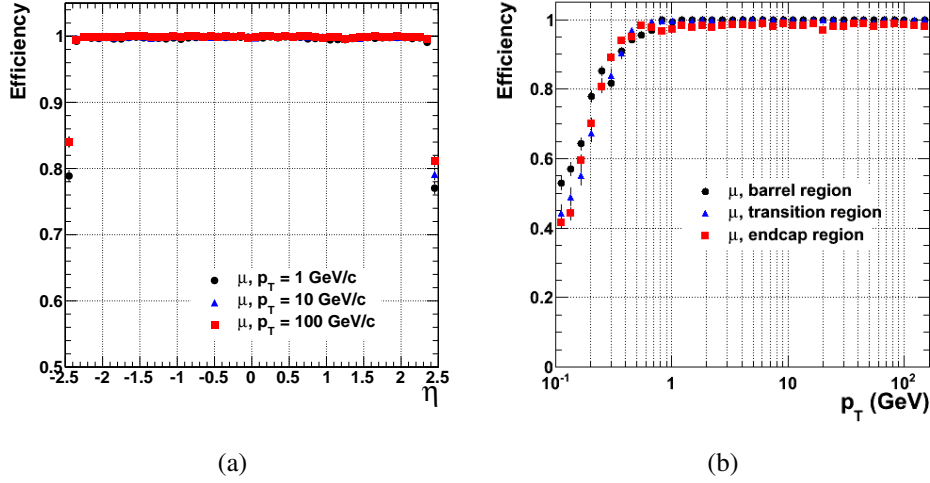


Figure 3.8: Global track reconstruction efficiency extracted from single track simulation as a function of  $\eta$  (a) and  $p_T$  (b) for muons of transverse momenta of 1, 10 and 100 GeV/c.

- Local reconstruction in the DTs begins with the reconstruction of mono dimensional hits in individual drift cells. The only information contained in these hits is their distance from the anode, with an intrinsic left/right ambiguity and without any information about their position along the wire. The cell hits are the starting point for the reconstruction of segments in the  $r - \phi$  and  $r - z$  projections separately. The 3D position and direction of the muon crossing the chamber are obtained combining the two projections, obtaining segments with an angular resolution of about 0.7 mrad in  $\phi$  and about 6 mrad in  $\theta$  [68].
- In a CSC chamber each plane measures a point in two dimensions. The radial coordinate  $r$  is measured by the wires, the azimuthal coordinate  $\phi$  by the strips. The hits in a chamber are used to fit a three-dimensional straight line segment (made of up to six points). The position resolution of segments varies from about 50  $\mu m$  in the first CSC station to about 250  $\mu m$  in the fourth [69]. The directional resolution varies with the chamber type, with an average of about 40-50 mrad in  $\phi$  and slightly worse in  $\theta$ .

- The RPCs have a spatial resolution limited by the strip pitch. The resolution on  $\phi$  is around 1 cm, while the orthogonal coordinate is only constrained by the strip length [70].

The results are track segments in the single DT and CSC chambers and individual points in the RPCs that are then used to form the stand-alone track, following a step-by-step method similar to the one used in the track and described in Section 3.3.1:

- *First step: seed generation.* The seeding algorithm takes DT and CSC segments as input and combines them to produce a set of initial states which are the starting point for the reconstruction of muon tracks. The efficiency of building a muon seed is mainly determined by detector acceptance and, in part, by the efficiency of segment reconstruction.
- *Second step: pattern recognition and fit.* Tracks are built using the Kalman filter technique, a recursive algorithm which performs the pattern recognition layer by layer and, at the same time, updates the trajectory parameters. Once all the hits have been collected, a final fitting step (smoothing) can be applied, updating the trajectory state at the location of all intermediate hits with the information from all the collected measurements, thus obtaining the optimal track parameters. The algorithm is flexible enough to allow different possible strategies: the fit can be applied in either direction, from the innermost layer towards the outermost or vice versa (forward or backward), possibly multiple times to remove a bias from the initial seed, and using either segments or individual hits to update the trajectory parameters.
- *Third step: ghost suppression.* The trajectory building algorithm is run for each seed. If the seeding algorithm fails to merge all the track segments from the same muon, several seeds can be built from a single muon, giving rise to duplicates of the same tracks. These duplicates, called ghosts, usually share a fraction of their measurements. In order to remove them, all the track candidates that share at least one hit are compared with each other and only the best candidate is kept. The algorithm proves very effective, especially in the barrel region, where the rate of duplicate tracks is reduced by several orders of magnitude.

- *Fourth step: beam spot constraint:* In order to improve the momentum resolution of tracks, the beam spot (see Section 3.3.2) position is used to constrain the track parameters. Although the beam position in the transverse plane is known within few tens of microns, the beam spot position uncertainty is set to 1 mm in the constraint. The constrained tracks are stored and made available to the global reconstruction. The unconstrained tracks are kept for reference and saved in a separate collection.

### Global muon reconstruction

After the completion of the reconstruction of the stand-alone tracks and in the inner tracker the reconstruction of global muon tracks can begin. Each stand-alone track is matched to a compatible tracker track and a fit of all the available measurements is performed.

The process of identifying the tracker track to combine with a given stand-alone muon track is referred to as “track matching” and consists of two steps.

The first step is to define a Region Of Interest (ROI) in the track parameter space that roughly corresponds to the stand-alone muon track, and to select the subset of tracker tracks inside this ROI. The matching is performed by comparing the parameters of both tracks by propagating them onto a common reference surface, the detector layer of the innermost stand-alone track hit.

The second step is to iterate over this subset, applying more stringent spatial and momentum matching criteria to choose the best tracker track to combine with the stand-alone muon.

Finally, a global track is fitted using all hits belonging to the matching tracker and stand-alone tracks. The global refit algorithm attempts to perform a fit for each tracker-stand-alone track pair. If more than one global track is produced for a given standalone, the one with the best  $\chi^2$  is chosen. Thus, for each stand-alone muon there is a maximum of one global muon that will be reconstructed.

In Fig. 3.9, the efficiency of global track reconstruction is shown for simulated muons with a flat  $\eta$  distribution between -2.5 and 2.5 and with design geometry and alignment. A large inefficiency appears in the barrel region for muons with  $p_T = 5$  GeV/c. At low  $p_T$ , muons easily stop in yoke without crossing all muon stations, especially in the barrel region, and stand-alone tracks are reconstructed

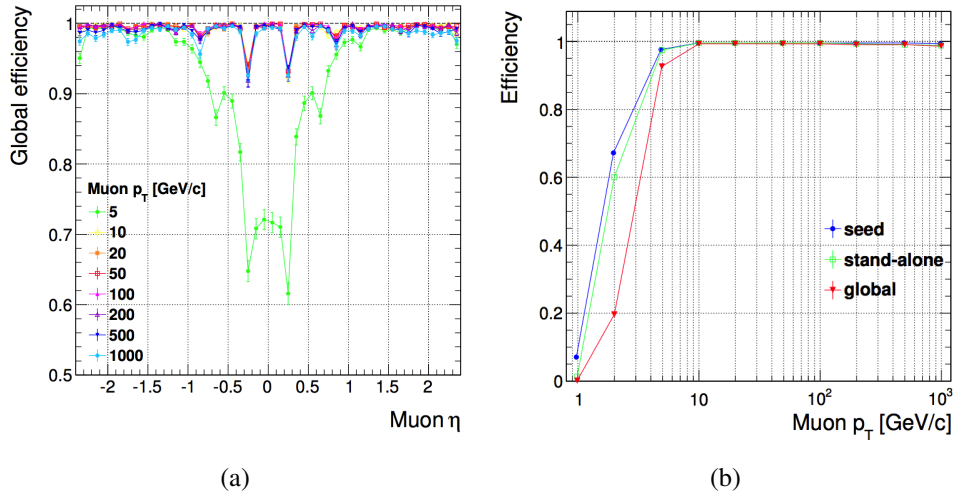


Figure 3.9: Global Muon track efficiencies from simulation (a) vs  $\eta$  and (b) vs  $p_T$  [67].

with a relatively low number of hits and with a poorer momentum resolution. This makes the matching with tracker tracks more difficult and less efficient.

### Tracker Muons Reconstruction

The standard muon track reconstruction starts from the muon system and combines stand-alone muon tracks with tracks reconstructed in the inner tracker. This approach naturally identifies the muon tracks in the detector. However, a large fraction of muons with transverse momentum below 6-7 GeV/c does not leave enough hits in the muon spectrometer to be reconstructed as standalone muons. Moreover, some muons can escape in the gap between the wheels. In order to recover the loss of efficiency for low  $p_T$  muons present in the Global Muon approach (see 3.9(b) a complementary approach has been designed to identify off-line these muons and hence improve the muon reconstruction efficiency. It consists in considering all silicon tracker tracks and identifying them as muons by looking for compatible signatures in the muon system. The algorithm for the muon identification of the tracker tracks starts with the extrapolation of each silicon track outward to its most probable location in the muon system. After collecting the associated signals the algorithm determines compatibility variables corresponding to how well the observed signals fit with the hypothesis that the silicon track is produced

by a muon. For each crossed or nearly crossed chamber in the muon system the algorithm looks for at least one associated segment and the resulting muon is called “tracker-muon”. Since each track is treated individually, if two or more tracks are near to each other, it is possible that the same segment or set of segments is associated to more than one track, resulting in duplicate tracker muons. This ambiguity can be resolved by the arbitration algorithm, which assigns segments to tracks by looking at the best  $\Delta R$  match.

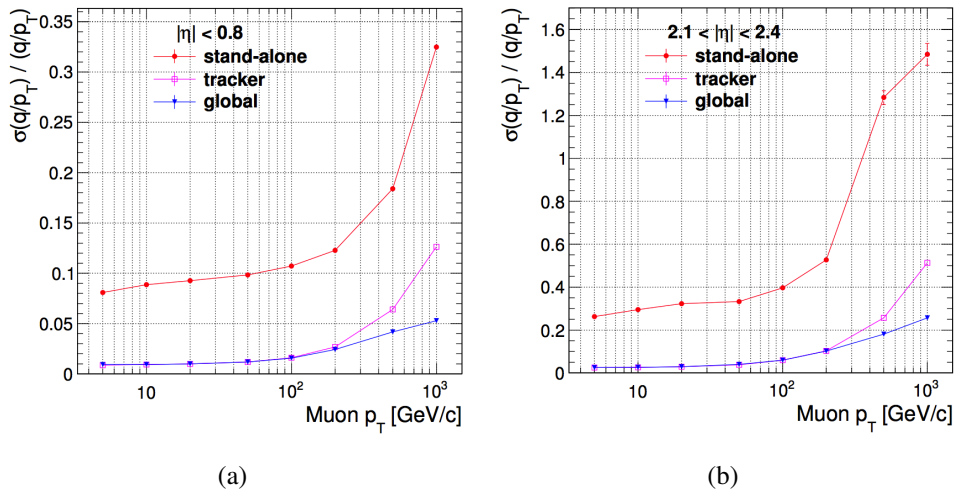


Figure 3.10: Muon  $q/p_T$  resolution vs.  $p_T$  for the three different types of fit: standalone (red), tracker-only (magenta) and global (blue) in the central part of the barrel (a) and in the forward region (b) [67].

Fig. 3.10 shows the  $q/p_T$  resolution of muons tracks resulting from the different fits: standalone, tracker-only and global. In the different  $\eta$  range, the resolution of global tracks is always dominated by the tracker resolution up to  $p_T \sim 200$  GeV/c. For higher  $p_T$ , the contribution of the muon system becomes significant and improves the global resolution by 10-20% at 1 TeV/c.

### Muon High Level Trigger

The CMS muon trigger, as explained in Section 2.2.6, is structured in a first hardware level, the Level-1 Trigger (L1), and a software part, the High Level Trigger (HLT).

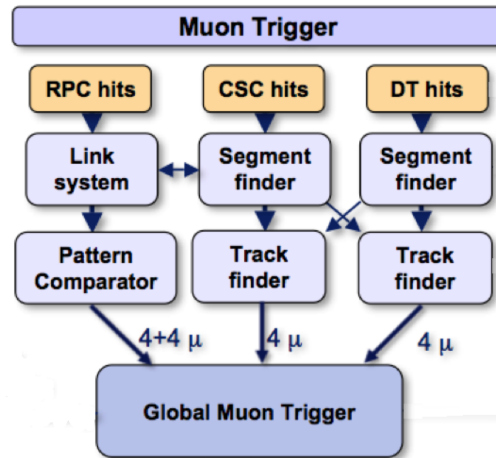


Figure 3.11: *Scheme of the L1 Muon Trigger.*

In Fig. 3.11 is reported the logic scheme of the L1 Muon Trigger. The muon *Level – 1* electronics uses groups of segments from DTs and CSCs, and hit patterns from RPCs. It identifies muon candidates, determines their position and quality, and provides a transverse momentum estimate in a discretely binned form, based on segment slopes in DTs and CSCs, and on predefined hit patterns in RPCs.

It also provides event timing and assigns events to a particular bunch crossing. Finally, the Global Muon Trigger (GMT) matches DT, CSC and RPC candidates, and rejects unconfirmed candidates of low quality. Up to four muon candidates, satisfying some minimal quality criteria and with the highest  $p_T$ , are transmitted to the HLT for further processing.

The HLT is implemented in software and runs on the CMS on-line filter farm. Muon HLT performs a full track reconstruction, using the same algorithms and software employed in the off-line reconstruction. The muon HLT is structured in two main levels, called “*Level-2*” and “*Level-3*”. This allows for a first reduction of the rate, based on a limited part of the information, which saves time for a more detailed reconstruction of the selected events.

After each HLT reconstruction level, a selection is applied on the reconstructed muon candidates. The main selection variables that can be used are the number of muon candidates in the event, their quality,  $p_T$ ,  $\eta$ , impact parameter, and isolation variables. The trigger requirements are implemented in software modules called

filters. A sequence of reconstruction steps and filters is called a trigger path. Different trigger paths can be defined by varying the filter cuts. In such a way, the muon trigger can be specialised to fulfil the needs of different physics analyses.

It is important to stress that a trigger path is considered successful only if the requirements of all the three levels are satisfied. When a muon candidate passes a trigger level, all the candidates in the event are transmitted to the following level, even those that failed the selection. In particular, a muon candidate failing to pass the L1 filter of a given path may still be reconstructed at L2 and L3, if the event passes to the next trigger levels, because of another trigger requirement; such a candidate (“volunteer”) is not considered for the trigger path which failed at L1.

### 3.3.4 Jet reconstruction

High energy quarks and gluons coming from the colliding protons almost instantly form hadrons that appear in the detector as *jets*. The jet reconstruction is important in all kinds of physics searches. The nature and the properties of jets provide us information about the physics processes that took place in the event under study. For example in the case of Higgs searches, the multiplicity and the topology of jets become clear signature for a particular type of production mechanisms, like vector boson fusion, associated production with b-jets and more.

A few steps are necessary to go from calorimeter digis (a.k.a. frames), which are essentially non-linear ADC counts, to jet objects:

- convert ADC counts, collected in HCAL and ECAL in reconstructed hits, to which the calibration corrections are applied;
- combine ECAL and HCAL cells into projective towers corresponding to HCAL granularity;
- run clustering algorithm to produce jets.

Several basic algorithms are currently implemented for CMS. The one used in this analysis is the “anti- $kt$ ” [71].

The  $kt$  and Cambridge/Aachen are inclusive jet finding algorithms and belong to a broader class of sequential recombination jet algorithms, parametrised by the power of the energy scale in the distance measure. The general idea is to have an idealised cone algorithm, in which only jets with a soft fragmentation are conical.

Let  $d_{ij}$  be the distance between entities, such as particles and pseudo-jets,  $i$  and  $j$ , and  $d_{iB}$  the distance between entity  $i$  and the beam (B). The inclusive clustering proceeds by identifying the smallest of the distances. If it is a  $d_{ij}$  the entities  $i$  and  $j$  are recombined, while if it is  $d_{iB}$ ,  $i$  is called *jet* and removed from the list of entities. The distances are recalculated and the procedure repeated until no entities are left. The generalization of this algorithms follows:

$$\begin{aligned} d_{ij} &= \min(k_{ti}^{2p}, k_{tj}^{2p}) \frac{\Delta_{ij}^2}{R^2} \\ d_{iB} &= k_{ti}^{2p}, \end{aligned} \quad (3.3)$$

where  $\Delta_{ij}^2 = (y_i - y_j)^2 + (\phi_i - \phi_j)^2$  and  $k_{ti}$ ,  $y_i$  and  $\phi_i$ , are respectively the transverse momentum, rapidity and azimuth of particle  $i$ . In addition to the radius parameter  $R$ , a parameter  $p$  is added to control the relative power of the energy against the geometrical,  $\Delta_{ij}$ , scales.

The case  $p = 1$  corresponds to the inclusive *kt* algorithm. It can be shown in general that for  $p > 0$  the behaviour of the jet algorithm with respect to soft radiation is rather similar to that observed for the *kt* algorithm, because what matters is the ordering between particles and for finite  $\Delta$  this is maintained for all positive values of  $p$ . The case of  $p = 0$  is special and it corresponds to the inclusive Cambridge/Aachen algorithm. The algorithm gives valid results even in the case where  $p$  is negative. The behaviour with respect to soft radiation will be similar for all  $p < 0$ , so here we will concentrate on the case where  $p = -1$  which is known as the anti-*kt* jet-clustering algorithm. The functionality of the anti-*kt* algorithm can be understood by considering an event with a few well separated hard particles with transverse momenta  $k_{t1}, k_{t2}, \dots$  and many soft particles. In the anti-*kt* algorithm  $d_{1i}$  between a hard particle 1 and a soft particle  $i$  is:

$$d_{1i} = \min\left(\frac{1}{k_{t1}^2}, \frac{1}{k_{ti}^2}\right) \frac{\Delta_{1i}^2}{R^2}. \quad (3.4)$$

This quantity is exclusively determined by the transverse momentum of the hard particle and the  $\Delta_{1i}$  separation. Therefore the  $d_{ij}$  between soft particles with similar  $\Delta$  separation will be much larger. As a result, soft particles will tend to cluster with hard ones long before they cluster among themselves. If a hard particle has no hard neighbours within a distance  $2R$ , it will simply accumulate all the soft particles within a circle of radius  $R$ , resulting in a perfectly conical jet.

If another hard particle 2 is present such that  $R < \Delta_{12} < 2R$  then there will be two hard jets, not perfectly conical:

- in case of  $k_{t1} \ll k_{t2}$  then jet 1 will be conical and jet 2 will be partly conical, since it will miss the part overlapping with jet 1;
- in case of  $k_{t1} = k_{t2}$  neither jet will be conical and the overlapping part will simply be divided by a straight line equally between the two.

For a general situation,  $k_{t1} \simeq k_{t2}$ , both cones will be clipped, with the boundary  $b$  between them defined by:

$$\frac{\Delta_{1b}}{k_{t1}} = \frac{\Delta_{2b}}{k_{t2}}. \quad (3.5)$$

Similarly when  $\Delta_{12} < R$  the particles 1 and 2 will cluster to form a single jet, that:

- in case of  $k_{t1} \ll k_{t2}$  will be a conical jet centred on  $k_1$ ;
- for  $k_{t1} = k_{t2}$  has a shape of union of cones with radius  $< R$  around each hard particle plus a cone of radius  $R$  centred on the final jet.

The key feature of the anti- $k_t$  algorithm is that the soft particles do not modify the shape of the jet, while hard particles do. The jet boundary in this algorithm is resilient with respect to soft radiation, but flexible with respect to hard radiation. Finally with this algorithm, the hard jets are circular with a radius  $R$ , and only the softer jets have more complicated shapes.

The output of this algorithm is a collection of calorimetric jets, written as a C++ class that contains all the jets characteristics and related properties.

### Jet energy corrections

The calorimeter response to particles is not linear and therefore it is not straightforward to translate the measured jet energy to the true particle or parton energy. The jet corrections are a set of tools that allows the proper mapping of the measured jet energy deposition to the analysis desired level (particle or parton).

CMS has adopted a factorized solution for their implementation, where each level of correction takes care of a different effect. Each level of correction is essentially a scaling of the jet four momentum with a scale factor (correction)

which depends on various jet related quantities as  $p_T$ ,  $\eta$ , flavor, etc. The levels of correction are applied sequentially (the output of each step is the input to the next) and with fixed order. They are the following:

**L1 Pile Up** to remove the energy coming from pile-up events. In principle this will remove any dataset dependence on luminosity so that the following corrections are applied upon a luminosity independent sample.

**L2 Relative** to make the jet response uniform in pseudorapidity. It is achieved by correcting a jet at a given  $\eta$  relative to a jet in the central region ( $|\eta| < 1.3$ ). The derivation of the Relative correction is done either by using MC truth or by employing a data driven method (dijet balance).

**L3 Absolute** to make the jet response flat versus  $p_T$ . The jet is corrected back to particle level, which means that the corrected CaloJet  $p_T$  is equal on average to the generated GenJet  $p_T$ . The derivation of the Absolute correction is done either by using MC truth information or by employing data driven techniques ( $Z/\gamma$ +jet balance).

**L4 EMF (electromagnetic energy fraction)** to make the jet response uniform versus the electromagnetic energy fraction. It is a residual correction on top of the default L2+L3 and it improves the jet resolution.

**L5 Flavour** to correct for the jet flavour dependence. It is optional and is applied on top of the default L2+L3 jet correction. It corrects back to the particle level.

The L2+L3 corrections scale the energy of an average QCD jet back to the energy of the corresponding generator level particle jet. However, analyses of the individual jet flavours (uds, c, b, gluon) need of different corrections for different jet flavours, because, when the L2+L3 corrections are applied, lead to an over- or under- correction depending on the jet flavour composition. For example, jets from the hadronic decay of a W boson consist only of uds and c quarks, which have a higher energy response than b and gluon jets.

L5 corrections are derived on QCD dijets events and from top-quark pair events.

**L7 Parton** The optional L7 parton correction is applied on top of the default L2+L3 correction and corrects back to the parton level, which means that the corrected CaloJet  $p_T$  is equal to the originating parton  $p_T$  on average. The L7 correction function has been calculated comparing the GenJet  $p_T$  to the matched parton in a cone with  $\Delta R < 0.15$ .

**L2L3 Residual** are introduced after the first collision data at  $\sqrt{s} = 7$  TeV, because the comparison between data and MC showed small differences in the jet energy response, up to 10%, depending on  $\eta$ . Therefore, the adopted strategy is: at first, the L2+L3 are applied, which takes care of the bulk of the energy response; and then a small residual calibration ( $\eta$  and  $p_T$  dependent) is applied to fix the small differences between data and MC.

### 3.3.5 Missing Transverse Energy reconstruction

Missing energy is used to infer the presence of non-detectable particles such as neutrinos or supersymmetric particles and is expected to be a signature of many new physics events.

In hadron colliders, the initial momentum of the colliding partons along the beam axis is not known, however the initial energy in particles travelling transverse to the beam axis is zero, so any net momentum in the transverse direction indicates Missing Transverse Energy (MET or  $E_T^{\text{miss}}$ ). Basically its reconstruction strongly depends on the calorimeter clusters, previously described as jets.

### 3.3.6 Particle Flow algorithm

The aim of the CMS particle flow event-reconstruction algorithm [72, 73] is to identify and reconstruct individually each particle arising from the LHC proton-proton collision, by combining the information from all subdetectors. The PF algorithm consists in the following steps:

- 1) taking informations from a local reconstruction, described above:

- calorimeter clustering,

- tracking, and extrapolation to the calorimeters,

- muon identification,

electron pre-identification;

- 2) linking topologically connected elements;
- 3) particle identification and reconstruction.

The algorithms at first point are not specific for the PF but are the ones described so far. Then dedicated linking and reconstructing algorithms are applied. The output is a list of particles used: to build jets and missing energy; to identify taus from their decay products; to quantify charged lepton isolation with respect to other particles; to tag jets coming from b-quarks, etc. The resulting global event description leads to an improvement in the performance of the reconstruction of jets and  $E_T^{miss}$ , and the identification of electrons, muons, and taus, because a precise measurement of the energy and direction for each particle is achieved by combining the capabilities of all the subdetectors.

#### 3.3.7 Link algorithm

In general for a given particle there are many particle flow elements in the various subdetectors, for example, a charged particle track, several calorimeter clusters, muon track etc. The event display in figure 3.12 shows an example of such case. The link algorithm connects these elements to fully reconstruct each single particle and avoid possible double counting from different detectors. The connection is performed according to the quality of the link. This last is defined for a given pair of elements in the event, as the distance between them. If the link has good quality a *block* is defined. In turn the blocks are linked to the other elements.

For a link between charged-particle track and calorimeter cluster, the track is extrapolated into the ECAL and HCAL, taking into account the typical shower shapes in all sub-detectors. A link to any given cluster is established if the extrapolated position is within cluster boundaries. To collect the energy of all bremsstrahlung photons emitted tracks are extrapolated to ECAL from the intersection points between the track and each of the tracker layers. A cluster is linked to the track as a potential bremsstrahlung photon if the extrapolated tangent position is within the boundaries of the cluster.

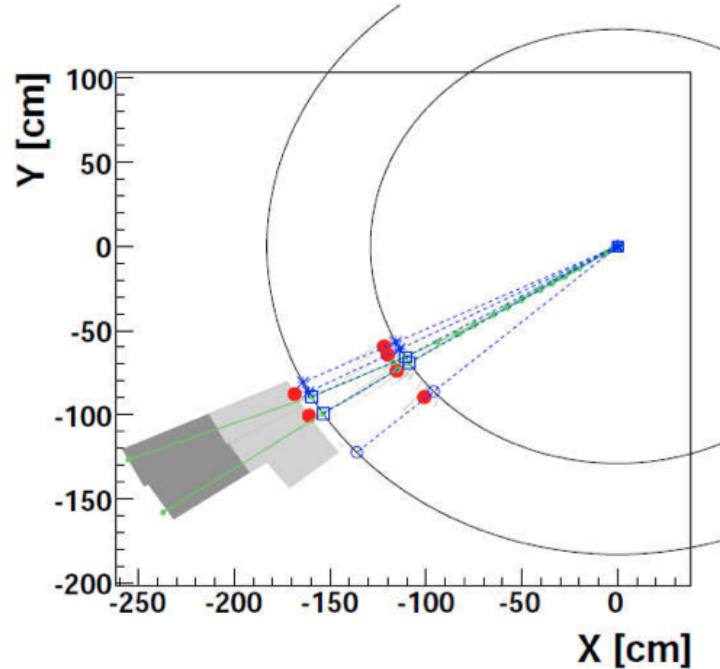


Figure 3.12: An event display of a simple hadronic jet in the  $(x, y)$  view.

To have a link between two calorimeter clusters (between ECAL and HCAL cluster or between ECAL and PS cluster), the cluster position of more granular calorimeter should be within the cluster envelope in the less granular calorimeter.

For charged-particle track in tracker and a muon track in muon system, link is established when a global fit between the two tracks returns an acceptable  $\chi^2$  [74]. When several global muons can be fit with a given muon track and several tracker tracks, only the global muon that returns the smallest  $\chi^2$  is retained.

Due to fine granularity of CMS detectors, these blocks typically contain only one, two or three elements which constitute simple inputs for particle reconstruction and identification algorithm.

### 3.3.8 Particle reconstruction and identification

The reconstruction and identification of a set of particles from each block of elements is finally performed using a dedicated PF algorithm. It starts from muons,

proceeds with electrons, charged hadrons and neutral hadronic and electromagnetic particles. The resulting list of reconstructed particles constitutes a global description of each event, available for subsequent physics analysis.

#### **PF-Muon reconstruction**

Each global muon [75] gives rise to a *PF-muon*[76], if its combined momentum is compatible with that determined from the sole tracker within three standard deviations. The details on the global muon reconstruction are given in 3.3.3.

Within the PF algorithm no further requirements are imposed on isolated muons, while for non-isolated muons slightly tighter criteria on the track-quality are applied to remove imbalances in the jet response, which can occur if neutral energy is wrongly associated to a muon, for example lost in the jets energy.

#### **Electron reconstruction**

Electron reconstruction is performed by combining tracking and ECAL information [77]. Seeds are formed from ECAL clusters as well as from tracks. For high electron momentum the seeding from the ECAL is very efficient (ECAL driven), while for low momentum electrons the seeding from tracks is more efficient (track driven). Each track of the block is submitted to a pre-identification stage which exploits the tracker as a pre-shower: electrons tend to give rise to short tracks, and to lose energy by bremsstrahlung in the tracker layers on their way to the calorimeter. Pre-identified electron tracks are refit with a Gaussian-Sum Filter [78] in an attempt to follow their trajectories all the way to the ECAL. A final identification is performed with a combination of a number of tracking and calorimetric variables. Each identified electron gives rise to a *PF-electron*, and the corresponding track and ECAL clusters, including all ECAL clusters identified as bremsstrahlung photons, are removed from further processing of the block.

In case of electrons within a jet, the energy is computed summing the ECAL deposits of geometrically adjacent clusters.

In case of isolated electrons the energy is measured in ECAL superclusters, which collect bremsstrahlung photons that are emitted along the electron track in the tracker volume.

### Charged and Neutral Hadrons

Charged hadron energy is obtained from a combination of the tracker and calorimeter measurements, when the two values are found to be compatible. Otherwise, if the energy measured in the calorimeters is small compared to the track momentum, a cleaning procedure to remove the potential spurious or mis-reconstructed tracks is invoked [79]. Otherwise if calorimeter response is too large, the algorithm assigns the energy excess to a photon and possibly to a neutral hadron.

#### 3.3.9 Particle Flow Jets

The reconstruction of *PF-jets* starts from the list of reconstructed particles previously described. The main difference with respect to the calorimetric jets, is that the latter are energy clusters in the calorimeters, while the *PF-jets* are cluster of particles in the overall detector. The jet momentum and spatial resolutions are expected to improve in this case, since the use of the tracking detectors and of the excellent granularity of the ECAL allows to resolve and precisely measure charged hadrons and photons inside jets, which constitute about 90% of the jet energy. The remaining 10% of energy, coming from neutral hadrons, is affected by the poor resolution of HCAL.

The further difference with respect to the calorimetric jets concerns the energy corrections. As explained in 3.3.4, the calorimetric jets need to be corrected for detector and physics effects, while in case of PF-jets just the detector effects play a role. Therefore in this case the reconstructed PF-jet energy is scaled by a factor that takes into account of an offset corrections for pile-up and noise, a factor for the calorimetric energy response as a function of PF-jet  $\eta$  relative to the barrel, and a factor for the absolute energy response as a function PF-jet  $p_T$  in the barrel.

#### 3.3.10 b-tagging Algorithm

In order to identify the provenance of a jet different kinds of algorithms are implemented in CMSSW. In general they are able to distinguish, from the jet properties, the quark from which they are coming.

For this analysis we are interested to a jet coming from b-quark.

Several b-tag algorithms have been implemented in CMSSW. Some exploit

the long b-quark lifetime, others its semi-leptonic decay mode and others use kinematic variables related to the high b-quark mass and hard b fragmentation function. A b-tag algorithm associates a single real number, called discriminator, to each jet. Depending on the algorithm, the discriminator, is obtained taking into account one or more b-jet properties.

Furthermore most of these properties can be exploited only using charged particle tracks, since only the tracker offers the spatial resolution needed to resolve properties of b-hadron decays.

This is the case of the *Combined Secondary Vertex* (CSV) algorithm [80], applied to the PF-jets of this analysis. It is based on the reconstruction of the secondary vertex of the b-quark decay. The secondary vertices are reconstructed in an inclusive way inside the jet, using all tracks in the jet and rejecting additional tracks used then to reconstruct more vertices. A multivariate analysis technique is used to compute a discriminator. It is based on a dedicated set of selection cuts applied to tracks and secondary vertices separately to reject backgrounds such as c-quarks,  $K_s^0$ ,  $\Lambda^0$  and nuclear interactions in the beam pipe or the first layers on the pixel detector. Further topological and kinematics variables related to the secondary vertex as well as variables related to the impact parameter significance of charged particle tracks are used.

#### 3.3.11 PF Missing Transverse Energy

In principle should be simple to compute the missing energy after the particle flow event reconstruction, since it is obtained summing the transverse momentum-vector of all reconstructed particles in the event, and taking the opposite of this azimuthal, momentum two-vector. The missing transverse energy is the modulus of this vector. Accurate reconstruction of MET is demanding because it entails reconstruction of all visible particles in an event with precision. This requires a hermetic detector which can contain all the particles which strongly or electromagnetically interact.

An algorithm of particle flow type, exploiting the ECAL high granularity, the HCAL tightness, the redundancy of the muon systems, and the spatial resolution of the silicon trackers, can give values very close to the generated missing energy, taken from simulation.

Since the PF-jet energy correction are applied, its effects has to be taken into account in the PFlow-MET computation applying the so called *Type-I* correction. This correction is the propagation of the L2L3 jet energy correction described in section



# Chapter 4

## The MSSM $H \rightarrow \mu^+ \mu^-$ search at CMS

The search for MSSM Higgs in the dimuon decay channel is performed using data collected during 2011 in collisions at  $\sqrt{s} = 7$  TeV, and during 2012 in collisions at  $\sqrt{s} = 8$  TeV.

Theoretical scenarios, chosen to benchmark the signal hypothesis, are presented here, while the selection criteria, the evaluation of the acceptance and the efficiency with its systematic errors, and the final results are presented in the next two chapters.

### 4.1 Benchmark scenarios

As already mentioned in sec. 1.5, Supersymmetry is a theory that solves many problems of the Standard Model. Nevertheless the theory contains many new free parameters, also in the simplest case of the MSSM. Many of these are coupling constants or mixing angles between the vacuum expectation values of the SUSY particles, and their values strongly depend on the model.

Due to the large number of free parameters, a complete scan of the MSSM parameter space is impossible. Therefore, to compare the discovery potential of new supersymmetric physics, the studies are restricted to some benchmark scenarios [81]. A scenario is defined by setting the values of most of the MSSM free parameters. There are several benchmark scenarios, as for example: the  $\mathbf{m}_h^{\max}$ , the

**no-mixing**, the **fermiophobic Higgs**, the **gluophobic Higgs** etc. The one chosen to perform the search presented in this thesis is the  $\mathbf{m}_h^{\max}$ .

#### 4.1.1 The $\mathbf{m}_h^{\max}$ scenario

The main involved parameters for the MSSM Higgs sector are the following:

$$\begin{aligned}
 M_t &= 173.2 \text{ GeV} \\
 M_{SUSY} &= 1000 \text{ GeV} \\
 \mu &= 200 \text{ GeV} \\
 M_2 &= 200 \text{ GeV} \\
 m_{\tilde{g}} &= 1500 \text{ GeV} \\
 X_t^{OS} &= 2M_{SUSY} \\
 X_t^{\overline{MS}} &= \sqrt{6}M_{SUSY} \\
 A_b &= A_\tau = A_t \\
 M_{\tilde{t}_3} &= 1000 \text{ GeV}
 \end{aligned} \tag{4.1}$$

where:  $M_t$  is the mass of top quark;  $M_{SUSY}$  denotes the value of mass at which the SUSY-breaking occurs, and it is assumed as mass of the third generation squarks;  $\mu$  is the mass mixing parameter of the two Higgs doublets;  $M_2$  is the SU(2) gaugino mass parameter;  $m_{\tilde{g}}$  is mass of gluino;  $M_{\tilde{t}_3}$  is the soft SUSY-breaking parameter in the neutrino sector;  $X_t$  is a parameter whose value depends from the renormalization scheme OS (on-shell) or  $\overline{MS}$  (modified minimal subtraction scheme);  $A_b$  is the trilinear coupling between the Higgs and the sbottom quark, which is set equal to the couplings  $A_t$  and  $A_\tau$  between Higgs and stop quark and Higgs and  $\tau$  respectively. Only two free parameters remain: the mass of scalar A,  $m_A$  and  $\tan\beta$ , the ratio between the vacuum expectation values of the two Higgs doublets.

This scenario is chosen for its property to maximize the Higgs-boson mass  $m_h$  as a function of  $\tan\beta$ , where  $m_h^{\max} < 135 \text{ GeV}$ . It is the most conservative scenario to derive bounds on  $\tan\beta$ . The masses of the other four Higgs bosons can be expressed as a function of these two parameters:

$$m_{H^\pm} = (m_W^2 + m_A^2)^{1/2} \tag{4.2}$$

$$m_h = \left\{ \frac{1}{2} \{ m_A^2 + m_Z^2 - [(m_A^2 + m_Z^2)^2 - 4m_A^2 m_Z^2 \cos^2 2\beta]^{1/2} \} \right\}^{1/2} \tag{4.3}$$

$$m_H = \left\{ \frac{1}{2} \{ m_A^2 + m_Z^2 + [(m_A^2 + m_Z^2)^2 - 4m_A^2 m_Z^2 \cos^2 2\beta]^{1/2} \} \right\}^{1/2} \quad (4.4)$$

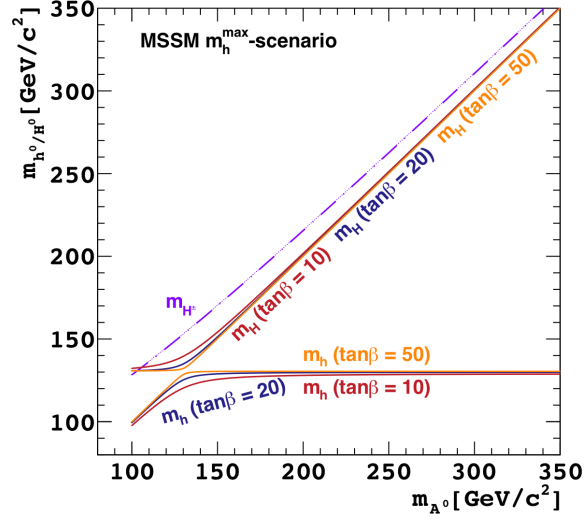


Figure 4.1: The plot shows the behaviour of the  $h$  and  $H$  bosons masses as a function of  $A$  boson mass. Curves of different color correspond to different  $\tan \beta$  values.

The dependence of the neutral bosons masses  $m_h$  and  $m_H$  with respect to  $m_A$ , in the  $m_h^{\max}$  scenario is presented in Fig. 4.1. Depending on  $\tan \beta$ , different curves are superimposed, and as it is evident, the  $\tan \beta$  dependence is quite smaller than one on  $m_A$ . Indeed by varying  $m_A$  it is possible to distinguish three different regions that correspond to three different regimes [82]:

**the decoupling regime**, occurs when  $m_A \gg m_h^{\max}$ . In this case, apart for  $m_h$  that achieves its maximum value at about 135 GeV and has properties similar to SM Higgs, the mass of the other bosons are very heavy and almost degenerate.  $H$  and  $A$ , besides their masses, are degenerate also in width and cross-section.

**The low  $m_A$  regime** occurs when  $m_A < m_h^{\max}$ . The behaviour of the two CP-even neutral Higgs bosons  $h$  and  $H$  is swapped with respect to the de-

## 4. The MSSM $H \rightarrow \mu^+ \mu^-$ search at CMS

coupling regime:  $h$  is almost degenerate in mass, width and cross section with  $A$ , and  $H$  is the SM-like Higgs, with a mass close to  $m_h^{\max}$ .

**the intense coupling regime** occurs for  $m_A \sim m_h^{\max}$ . It leads to similar, but not degenerate, masses for the three neutral Higgs bosons: this property can be exploited, in principle, to detect the three neutral Higgs separately, as also the cross-sections are large enough to allow the study through the  $H \rightarrow \mu^+ \mu^-$  decay channel.

The position of the crossover point depends mostly on the nature of the mass mixing in the stop sector. The dependence of the  $A$  width,  $\Gamma_A$ , on the  $m_A$  for

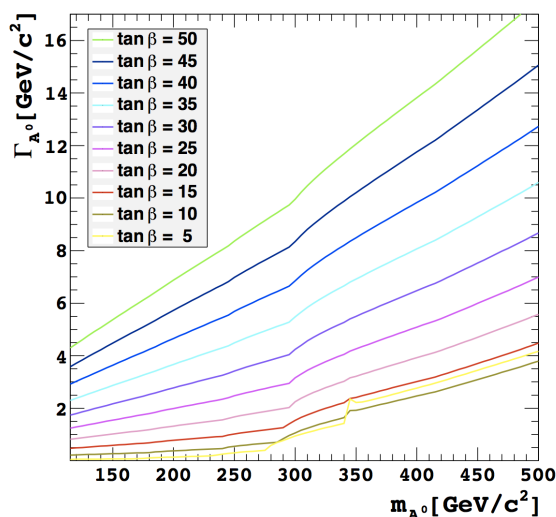


Figure 4.2: The plot shows the behaviour of width of boson  $A$  as a function of its mass. Curves of different color correspond to different  $\tan \beta$  values.

different values of  $\tan \beta$  is shown in Fig.4.2. The kinks observed for  $m_A \sim 300$  GeV are due to the opening of the  $t\bar{t}$  decay channel, kinematically forbidden at lower values of  $m_A$ .

### 4.1.2 The $m_h^{\text{mod}}$ scenario

After the recent discovery of the Standard Model Higgs boson with a mass of approximately 125 GeV a modified  $m_h^{\max}$  scenario, called  $m_h^{\text{mod}}$ , was pro-

posed [83]. As in the MSSM model the light neutral Higgs  $h$  corresponds to the SM Higgs boson in the limit of large values of  $m_A$ , the modified scenario employs a set of parameters so that  $m_h$  does not exceed 125 GeV. A convenient way of modifying the  $m_h^{\max}$  scenario in this way is to reduce the amount of mixing in the stop sector, i.e. to reduce  $|X_t/M_{SUSY}|$  compared to the value of about 2 (eq.4.1) that gives rise to the largest positive contribution to  $m_h$  from the radiative corrections. This can be done for both signs of  $X_t$ , therefore the  $m_h^{\text{mod}}$  scenario is proposed by their authors in two different versions, called  $m_h^{\text{mod}+}$  and  $m_h^{\text{mod}-}$ , which differ by their sign and absolute value of  $X_t/M_{SUSY}$ .

The parameters for these two modified scenarios are the following:

$$\begin{aligned}
M_t &= 173.2 \text{ GeV} \\
M_{SUSY} &= 1000 \text{ GeV} \\
\mu &= 200 \text{ GeV} \\
M_2 &= 200 \text{ GeV} \\
m_{\tilde{g}} &= 1500 \text{ GeV} \\
X_t^{OS} &= 1.5M_{SUSY} (X_t^{OS} = -1.9M_{SUSY}) \\
X_t^{\overline{MS}} &= 1.6M_{SUSY} (X_t^{MS} = -2.2M_{SUSY}) \\
A_b &= A_\tau = A_t \\
M_{\tilde{t}_3} &= 1000 \text{ GeV}
\end{aligned} \tag{4.5}$$

The results of the MSSM Higgs boson performed in this analysis are given in both kinds of scenarios: the  $m_h^{\max}$ , and the two  $m_h^{\text{mod}}$ . Although the  $m_h^{\max}$  scenario provides upper values of  $m_h$  that are about 5 GeV higher than the observed SM Higgs mass, it is still used in this analysis to allow the comparison with results of previous analyses, that were performed within the same benchmark condition.

## 4.2 Production and decays of the MSSM Neutral Higgs boson at LHC

The MSSM neutral Higgs production  $pp \rightarrow \Phi + X$  at the LHC is dominated by two processes: the  $b\bar{b}$ -associated production  $b\bar{b}\Phi$ , where  $\Phi$  is produced together with a  $b\bar{b}$  pair, (Fig.4.3a), and the *gluon gluon fusion* process,  $gg\Phi$  (Fig.4.3b).

#### 4. The MSSM $H \rightarrow \mu^+ \mu^-$ search at CMS

As it is mentioned in sec. 1.5, one of the Higgs doublet gives mass to the down-type quarks and the other gives mass to the up-type quarks, while  $\tan \beta$  represents the ratio between the vacuum expectation value of the two doublets. Therefore the coupling between the Higgs and the quarks strongly depends on  $\tan \beta$ . In particular the coupling of  $\Phi$  to b-quarks is enhanced at large values of  $\tan \beta$  with respect to the SM Higgs case [84]:

$$g_{bb\Phi}^{MSSM} = \tan \beta \cdot g_{bbH}^{SM} \quad (4.6)$$

As a consequence, while for low values of  $\tan \beta$  ( $< 15$ ) the main production

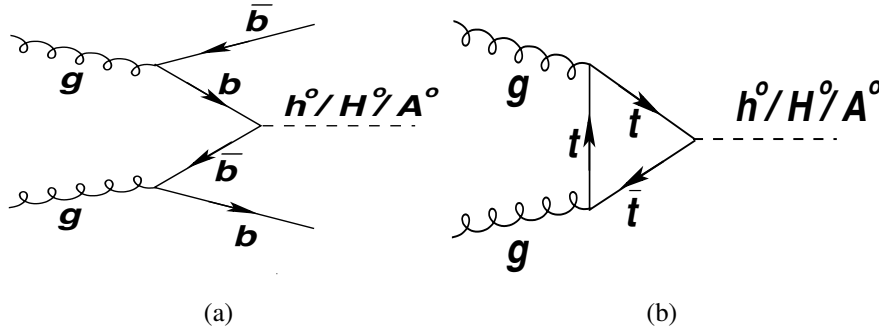


Figure 4.3: The Feynman diagrams represent the MSSM Higgs bosons production at LHC in the b-associated channel,  $b\bar{b}\Phi$  (a) and in the gluon-gluon fusion process  $gg\Phi$  (b).

mechanism is the gluon fusion, for high values of  $\tan \beta$  the b-associated production becomes dominant.

The production cross section of the  $\Phi$  boson at  $\sqrt{s} = 7$  TeV and  $\sqrt{s} = 8$  TeV as a function of its mass is shown respectively in figures 4.4 and 4.5. The values are computed using the FeynHiggs program [85, 86], in the framework of the  $m_h^{\max}$  scenario. In both figures the plots on the right (for  $\tan \beta = 30$ ), point out that the Higgs boson production in association with b quarks is enhanced with respect to the plots on the left (for  $\tan \beta = 5$ ), by a factor  $2 \tan^2 \beta$ .

For the same reason the neutral Higgs decay to b quarks has the highest branching fraction, about 90% (Fig.4.6). Indeed it is the heaviest down-type fermion. Moreover, the Higgs coupling is proportional to the square of particle mass. That explains why the second favourite decay channel is the  $\tau^+ \tau^-$  with

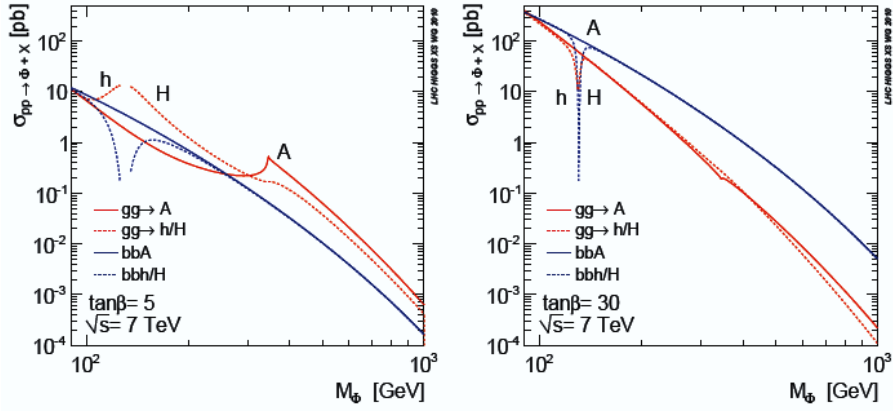


Figure 4.4: The production cross section of the  $\Phi$  boson at  $\sqrt{s} = 7$  TeV as a function of its mass for  $\tan\beta = 5$  (left) and  $\tan\beta = 30$  (right).

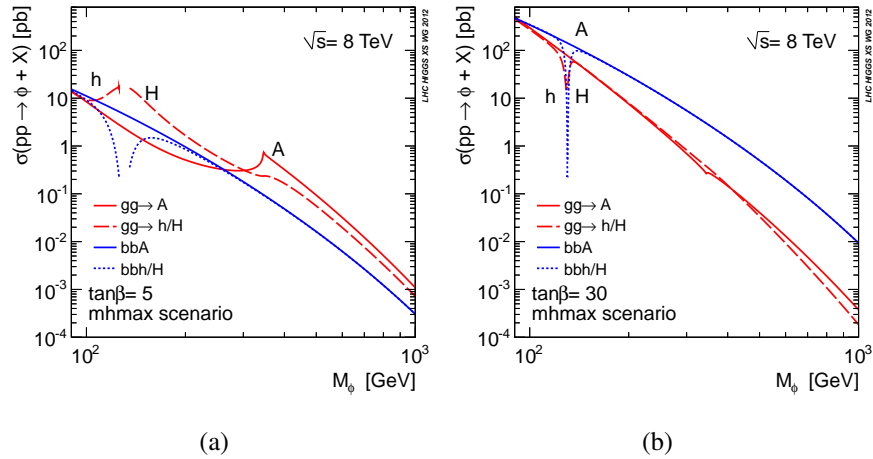


Figure 4.5: The production cross section of the  $\Phi$  boson at  $\sqrt{s} = 8$  TeV as a function of its mass for  $\tan\beta = 5$  (left) and  $\tan\beta = 30$  (right).

about 10% of branching fraction. A further MSSM Higgs decay has to be taken into account: the  $\mu^+\mu^-$  channel.

Despite their low branching ratio, the leptonic decays provide higher sensitivity than the  $b\bar{b}$  decay, strongly contaminated by the large QCD background characteristic of the LHC environment. Among them, while the  $\tau^+\tau^-$  process has a branching ratio larger by a factor  $(m_\tau/m_\mu)^2$  and provides better sensitivity

#### 4. The MSSM $H \rightarrow \mu^+ \mu^-$ search at CMS

in terms of statistics, the  $\mu^+ \mu^-$  process has a cleaner experimental signature and benefits of the full reconstruction of the final state. Furthermore, thanks to the high precision of the muon momentum measurement at CMS, the Higgs mass can be reconstructed from  $\mu^+ \mu^-$  decays with a better resolution, and a measurement of the  $\tan \beta$  parameter can be performed.

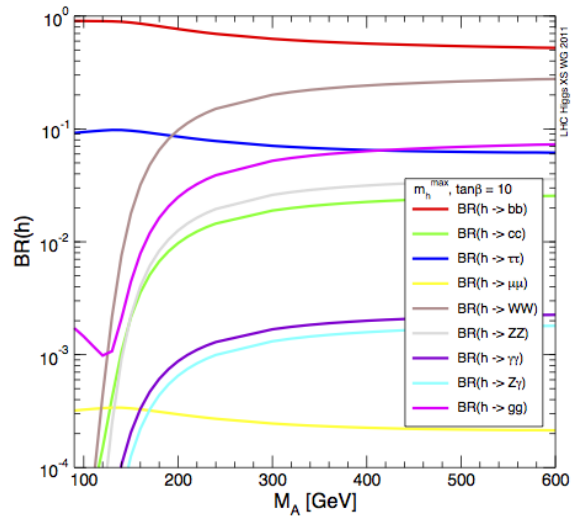


Figure 4.6: The decay branching ratios of the h boson as a function of A boson mass.

# Chapter 5

## Event selection

In this chapter the selection adopted to search for the neutral MSSM Higgs bosons in the supposed dimuon decay channel is described.

Usually, in the searches for new particles, the expected signal is studied from simulated samples, while the background can be estimated following different approaches: the so called *data-driven*, that exploits the data, or the *MC-based*, that uses simulated samples. This analysis adopts the data-driven approach, but, in order to verify the correct understanding of the role of different processes, simulated samples are also used for the study of background.

The experimental signature of the MSSM Higgs boson  $\Phi$ , considered in this analysis, is a pair of opposite-charged, isolated muon tracks with high transverse momentum:

$$\Phi \rightarrow \mu^+ \mu^-, \quad \Phi = A, H, h. \quad (5.1)$$

Their reconstructed invariant mass corresponds to the mass of the  $\Phi$  boson.

This signature can be simple to be separated from the hadronic processes that dominate at LHC, but the very low branching ratio of this process imposes to maximize the signal sensitivity while keeping under control the background. This is achieved making an events categorization, whose details are described below.

The main source of background comes from the processes with muon pairs in the final state such as *Drell-Yan* processes and  $t\bar{t}$  productions. The first is constituted by the dimuonic decays of the Z or  $\gamma^*$  bosons, while the second by the semileptonic decays of the top quark. Since this last process implies a presence of at least one neutrino, a veto on the missing energy is imposed.

## 5.1 Data and Simulated Samples

This search is performed using the data collected by the CMS experiment in years 2011 and 2012 in proton-proton collisions respectively at  $\sqrt{s} = 7$  and 8 TeV. They correspond to an integrated luminosity of  $5.1 \text{ fb}^{-1}$  for 2011 and  $19.4 \text{ fb}^{-1}$  for 2012. Details on the two datasets can be found in Tab. 5.1 and 5.2.

Datasets at $\sqrt{s} = 7 \text{ TeV}$	Run range	$\int \mathcal{L} [\text{fb}^{-1}]$
SingleMu/Run2011A-08Nov2011-v1/AOD	160329-175770	2.33
SingleMu/Run2011B-13Jul2012-v1/AOD	175832-180252	2.77

Table 5.1: *The datasets collected in year 2011 at  $\sqrt{s} = 7 \text{ TeV}$  used for the analysis, their run range and their corresponding integrated luminosity. The total integrated luminosity is  $5.1 \text{ fb}^{-1}$ .*

Datasets cat $\sqrt{s} = 8 \text{ TeV}$	Run range	$\int \mathcal{L} [\text{fb}^{-1}]$
SingleMu/Run2012A-13Jul2012-v1/AOD	190459-193621	0.81
SingleMu/Run2012B-13Jul2012-v1/AOD	193834-196531	4.40
SingleMu/Run2012C-24Aug2012-v1/AOD	198022-198523	0.50
SingleMu/Run2012C-PromptReco-v2/AOD	198934-203755	6.40
SingleMu/Run2012D-PromptReco-v1/AOD	203773-208940	7.27

Table 5.2: *The datasets collected in year 2012 at  $\sqrt{s} = 8 \text{ TeV}$  used for the analysis, their run range and their corresponding integrated luminosity. The total integrated luminosity is  $19.4 \text{ fb}^{-1}$ .*

The name of these datasets descends from the name of the HLT, used at CMS during the data acquisition.

Simulated samples are generated for the signal and for the most of the background processes with Pythia [50], otherwise with MadGraph, and in both cases with the same physics conditions of the data taking.

To reproduce the type of PU conditions of the data-taking, the same kind of samples have been produced in collisions at  $\sqrt{s} = 7 \text{ TeV}$  including the so-called

*Fall-2011* PU condition [87], and in collisions at  $\sqrt{s} = 8$  TeV including the so-called *Summer-2012* PU condition. The first samples are used for the studies with data of 2011 and the second for the studies with data of 2012.

### Simulated signal

The signal considered in this analysis covers a wide range of  $m_A$  and  $\tan \beta$  values: from 115 to 500 GeV for the first, and from 5 to 55 for the second.

The samples are produced for a set of  $(m_A, \tan \beta)$  points in the MSSM  $m_h^{\max}$  scenario free parameters space. For each point, six processes are simulated: three for A, H and h produced in association with a b-pair, whose Feynman diagram is shown in Fig.4.3 (a), and three for A, H and h produced in the gluon fusion process, whose Feynman diagram is shown in Fig.4.3 (b). These informations are summarised in Tab. 5.3.

$m_A$ (GeV)	$m_A$ (GeV) step	$\tan \beta$	$\tan \beta$ step
115-200	5	5-55	5
200-300	25	5-55	5
300-500	50	5-55	5

Table 5.3: *The  $m_A$  and  $\tan \beta$  values used to generate the signal samples.*

Each of these samples contains 2000 simulated events. Then for each  $(m_A, \tan \beta)$  point, the total expected signal comes from the sum of the events in the six samples, where each of them is opportunely re-weighted for its cross section: In order to use more accurate values, as also suggested from the CMS Higgs analysis group, the values of cross-section and mass of the MSSM neutral Higgs bosons are not taken from the Pythia generator, but are calculated with FeynHiggs [85] using the *5-flavour* scheme [88]. This program evaluates the cross section to next-to-next-to-leading order accuracy in the strong coupling constant, using the probability density function (PDF) MTSW2008 [89] and the related uncertainties.

To study the signal in the MSSM modified scenarios, the same samples generated with Pythia with the  $m_h^{\max}$  parameter set are used, since the Higgs production and decay kinematic remains the same. This is clear from figures 5.1 and 5.2, where Higgs mass and width values predicted by Pythia in the  $m_h^{\max}$  are com-

## 5. Event selection

pared to the values predicted by FeynHiggs in the  $m_h^{\text{mod}+}$  and  $m_h^{\text{mod}-}$  scenarios. The values are very similar between them, the major effect is in the width, but the changes are of the order of per mille with respect to the value of Higgs mass, so below the detector resolution.

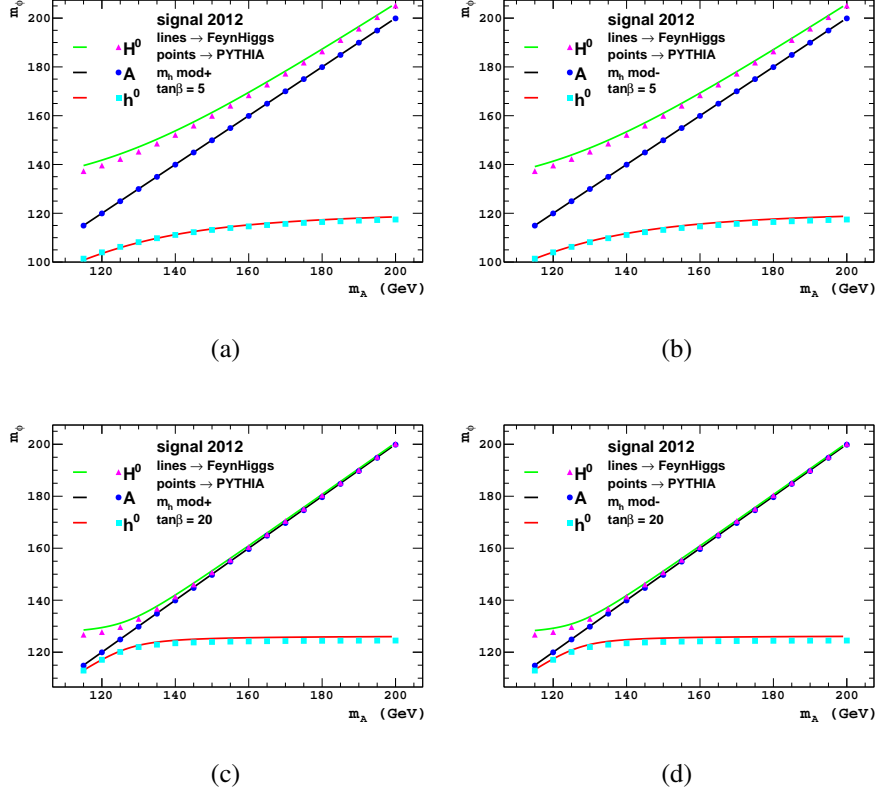


Figure 5.1: Mass of the three Higgs bosons as function of  $m_A$ : the plots show, separately for  $h$ ,  $H$  and  $A$ , the comparison between the values from Pythia samples in  $m_h^{\text{max}}$  and the values computed with FeynHiggs in the  $m_h^{\text{mod}+}$  (a, c) and  $m_h^{\text{mod}-}$  (b, d). This comparison is shown for  $\sqrt{s} = 8 \text{ TeV}$  in case of  $\tan \beta = 5$  (top), and  $\tan \beta = 20$  (bottom).

### Simulated background

The main source of background for this analysis is the Drell-Yan process:

$$Z/\gamma^* \rightarrow \mu^+ \mu^-, \quad (5.2)$$

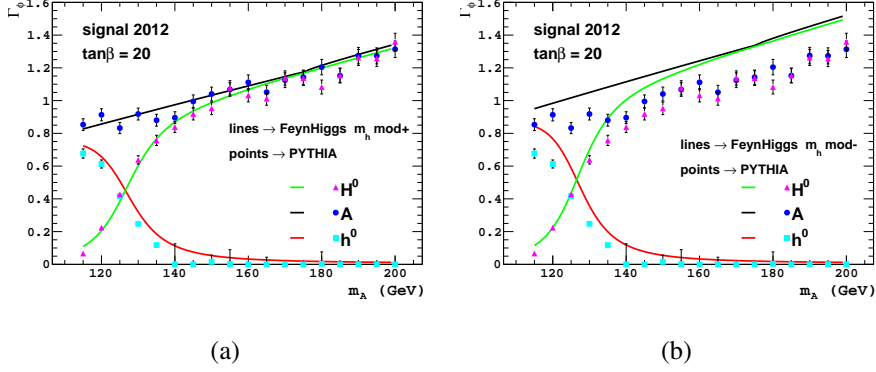


Figure 5.2: Width ( $\text{GeV}/c^2$ ) of the three Higgs bosons as function of  $m_A$ : the plots show, separately for  $h$ ,  $H$  and  $A$ , the comparison between the values from Pythia samples in  $m_h^{\text{max}}$  and the values computed with FeynHiggs in the  $m_h^{\text{mod}+}$  (a) and  $m_h^{\text{mod}-}$  (b). This comparison is shown for  $\sqrt{s} = 8 \text{ TeV}$  in case of  $\tan \beta = 20$ .

where the  $Z/\gamma^*$  is produced in association with a quark anti-quark pair. Among them, the  $b\bar{b}Z$  process is an irreducible background, since as in the signal there is a presence of jets from b-quark whereas events of the type  $c\bar{c}Z$  and  $q\bar{q}Z$  (where  $q = u, d, s$ ) can be suppressed.

Another relevant source of background comes from opposite-sign dimuon pairs produced in semileptonic decay of the top quark in  $t\bar{t}$  events:

$$t\bar{t} \rightarrow (W^- \bar{b})(W^+ b) \rightarrow (\mu^- \bar{\nu}_\mu \bar{b})(\mu^+ \nu_\mu b). \quad (5.3)$$

Other less relevant background processes are:  $W^\pm W^\pm$ ,  $W^\pm Z$  and  $ZZ$ , that contribute very little to the dimuon invariant mass distribution for masses larger than 110 GeV, where the search for the signal is performed.

The MC background samples are listed in Tab. 5.4 and 5.5 with their corresponding cross-sections and number of events.

Since the analysis is completely data-driven, these samples are used only to optimise the selection criteria, and not to compute the results, neither to determine the background for the expected signal. The background properties, its amount and shape, are entirely measured from the data. The following plots that show data-MC comparison are meant for illustration only.

## 5. Event selection

Sample & Generator	$\sigma$ (pb)	Events
DYJetsToLeptonLepton_7TeV-madgraph/Fall111-PU	3048.0	36264432
TTJets_7TeV-madgraph/Fall111-PU	165.8	10000000
WW_7TeV_pythia6/Fall111-PU	55.3	4225916
WZ_7TeV_pythia6/Fall111-PU	17.0	4265243
ZZ_7TeV_pythia6/Fall111-PU	3.8	4191045

Table 5.4: Monte Carlo background samples simulated at  $\sqrt{s} = 7$  TeV, their corresponding cross-section and number of events.

Sample & Generator	$\sigma$ (pb)	Events
DYJetsToLeptonLepton_8TeV-madgraph/Summer12-PU	3503.7	30459503
TTJets_8TeV-madgraph/Summer12-PU	225.2	6923652
WW_8TeV_pythia6/Summer12-PU	57.1	10000431
WZ_8TeV_pythia6/Summer12-PU	32.03	10000283
ZZ_8TeV_pythia6/Summer12-PU	8.3	9799908

Table 5.5: Monte Carlo background samples simulated at  $\sqrt{s} = 8$  TeV, their corresponding cross-section and number of events.

## 5.2 Event selection

The analysis is performed on data preselected on-line, where just the events that fire the isolated single-muon HLT are taken. At off-line level the PF technique is used to reconstruct the full event. At this point a specific selection cuts are applied: the events are required to fulfil the set of criteria accurately described below. The cut values are chosen in order to maximise the signal significance, defined as  $S/\sqrt{S+B}$ , where S are the signal events and B the background events of MC surviving a selection cut. To perform the event selection a C++ analyser was written in the CMSSW framework. It is interfaced with ROOT to produce the histograms and to perform the statistical treatment of data.

### 5.2.1 Trigger on-line selection

The events are preselected by the isolated single-muon HLT with the lowest transverse momentum threshold applied at CMS. This corresponds to  $p_T > 24$  GeV. The condition for this kind of trigger slightly changes from 2011 to 2012 data taking: the corresponding HLT path name for the dataset 2011A is HLT\_IsoMu24. For the rest of datasets, the trigger selection is restricted to the pseudorapidity range  $|\eta| < 2.1$ , and its path name is HLT\_IsoMu24\_eta2p1. The pseudorapidity cut is applied at the L1 trigger level, because of the poor resolution of the  $p_T$  measurement and the high rate in the very forward region of the muon chambers. Without this cut there would be a large amount of low quality muons, that would saturate the HLT band, but would be discarded later for their wrong momentum.

Anyway, in the off-line selection just the muons with  $|\eta| < 2.1$  are accepted, and all the datasets are treated in the same way.

### 5.2.2 Monte Carlo pile-up re-weighting

The MC samples are produced assuming a distribution for the number of PU interactions that roughly reproduce, though not exactly match, the average PU conditions expected for the data-taking. To re-weight for this mismatch an event by event correction is applied to simulated samples. It is based on the data-MC comparison of the *true number of interactions* [90].

The distribution expected in the data is computed by:

$$N_{true} = \mathcal{L}_{ist} \cdot \sigma_{inel}(pp), \quad (5.4)$$

where  $\mathcal{L}_{ist}$  is the measured instantaneous luminosity, and  $\sigma_{inel}(pp)$  is the total p-p inelastic cross-section.

The corresponding distribution for MC, is given by the number of PU interaction superimposed to the main event.

A weight is then computed event by event from the ratio of these two distributions, and it is assigned to each MC event.

### 5.2.3 Primary vertex selection

The events that pass the on-line trigger selection are processed by the off-line analysis. This requires events with at least one well reconstructed primary vertex (PV), i.e. with a ratio between  $\chi^2$  and the number of degrees of freedom  $\chi^2/ndf_{PV}$  smaller than 10. Its distance along the beam axis from the nominal centre of the detector has to be  $|z_{PV}| < 24$  cm.

### 5.2.4 Selection of $\mu^+\mu^-$ pairs

The events are selected if they contain at least two opposite-charged *tight-muon*. A PF-muon is defined *tight* if it fulfils the following requirements:

- it must have at least: 1 hit in the pixel detector alone, 6 layers with hits in pixel and strips tracker, and 1 hit in the muon chambers. In addition the  $\chi^2/ndf$  of the global fit must be smaller than 10. Such requirements provide a good measurement of the muon track momentum.
- to discard muon particles from cosmic rays, the transverse and longitudinal impact parameter of each PF-muon must be  $|d_{xy}| > 0.02$  cm and  $|d_z| < 0.1$  cm respectively.

The tight PF-muons are requested to have pseudorapidity  $|\eta| < 2.1$  and transverse momentum  $p_T > 25$  GeV. In events with more than two muon candidates, the two muons with the highest transverse momentum are considered. Furthermore at least one of the selected muons is requested to match the direction of the HLT candidate within a cone of  $\Delta R = 0.2$ . The  $\Delta R = \sqrt{\Delta\phi^2 + \Delta\eta^2}$  is the distance defined in the  $\phi - \eta$  plane, computed, in this case, between the PF-muon and the HLT candidate.

Both muon candidates have also to be isolated:  $I_\mu < 0.12$ . The isolation variable  $I_\mu$  used for this analysis is computed in a cone of width  $\Delta R = 0.4$  around the PF-muon and it is defined as:

$$I_\mu = \left( \sum p_T^{ChHad} + \delta_{PU} \right) / p_T^\mu \quad (5.5)$$

where  $\sum p_T^{ChHad}$  is the scalar sum of the transverse momenta of the track and

$$\delta_{PU} = \max \left\{ \sum E_T^{NeutHad} + \sum E_T^{Phot} - 0.5 \cdot \sum p_T^{PU ChHad}, 0 \right\} \quad (5.6)$$

is a factor that takes into account the energy coming from PU:  $\sum E_T^{NeutHad}$  and  $\sum E_T^{P^{hot}}$  is the scalar sum of the transverse energy of the neutral hadronic and electromagnetic particles respectively, while  $\sum P_T^{PU ChHad}$  is the scalar sum of the  $p_T$  of the charged particles that do not originate from the PV, and the factor 0.5 corresponds to the approximated average of neutral to charged particles[91].

A detailed summary of the muon selection criteria is given in Tab. 5.6.

$\mu$ type	PFMuon
$p_T$ (GeV)	$\geq 25$
$ \eta $	$\leq 2.1$
$Iso_\mu$	$\leq 0.12$
$\chi^2/ndf$	$\leq 10$
$ d_{xy} $ (cm)	$\leq 0.02$
$ d_z $ (cm)	$\leq 0.1$
$N_{\text{Pixel Hits}}$	$\geq 1$
$N_{\text{MuonChamber Hits}}$	$\geq 1$
$N_{\text{Matched Segments}}$	$\geq 2$
$N_{\text{Tracker Layers}}$	$\geq 6$

Table 5.6: List of the muon selection criteria.

The distributions of transverse momentum and pseudorapidity of the two selected PF-muons are shown in Fig. 5.3 for events at  $\sqrt{s} = 7$  TeV, and in Fig. 5.4 for events at  $\sqrt{s} = 8$  TeV. These stacked-plots contain a data-simulation comparison, where the data are represented by the black points and each component of signal and background is superimposed with a dedicated colour. The expected distribution for the sum of the signal processes  $b\bar{b}\Phi \rightarrow \mu^+\mu^-$  and  $g\bar{g}\Phi \rightarrow \mu^+\mu^-$ , chosen in this case, is the one for  $m_A = 150$  GeV and  $\tan\beta = 30$ .

The *MuSclFit* correction [92] is applied to the selected PF-muons to improve their momentum resolution. This correction is performed to take into account alignment effects, like shifts and deformations in the transverse plane, and magnetic field effect, that affects the muon momentum resolution. The correction is applied on both data and simulated events. The latter need an extra smearing on the muon momentum, also applied.

## 5. Event selection

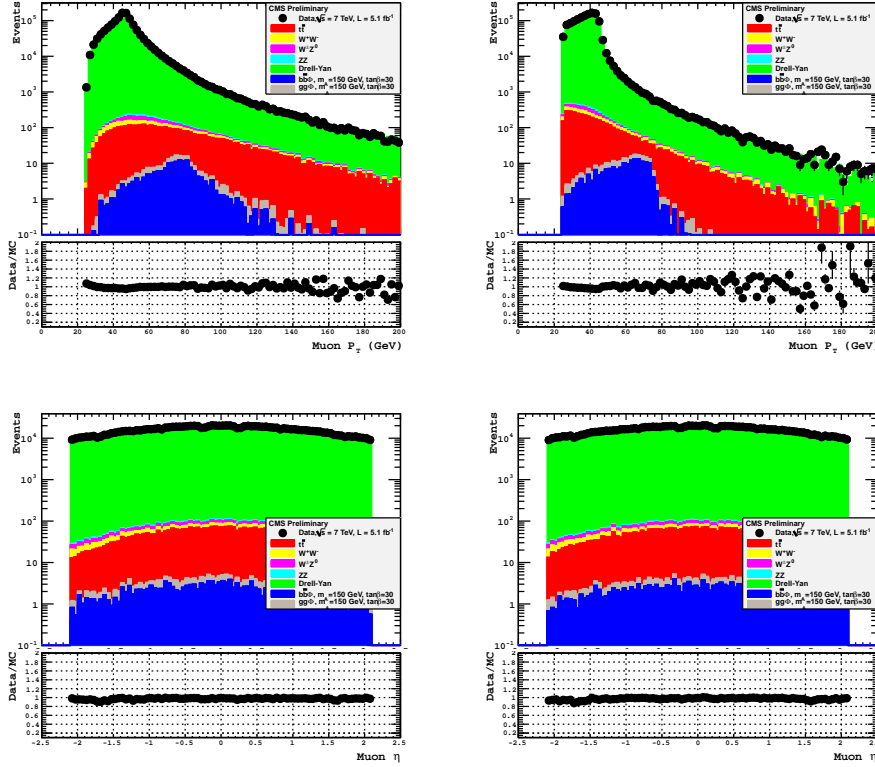


Figure 5.3: The distribution of the highest and second-highest transverse momentum of the muons candidates (top left and top right respectively). Distribution of the pseudorapidity  $\eta$  of the highest and second-highest transverse momentum muon (bottom left and bottom right respectively) at  $\sqrt{s} = 7$  TeV. For each plot the ratio between data and background simulated events is also shown.

Figure 5.5 shows the invariant mass distribution of the selected dimuon pairs, before any further selection cut, for events at  $\sqrt{s} = 7$  and  $\sqrt{s} = 8$  TeV. The data are clearly peaked at the mass value of 91 GeV, corresponding to the Z boson. The background from standard model processes is superimposed: it is strongly dominated by Drell-Yan events in the low mass region, and by the  $t\bar{t}$  events in the higher mass region. The expected signal in the case described above is also shown.

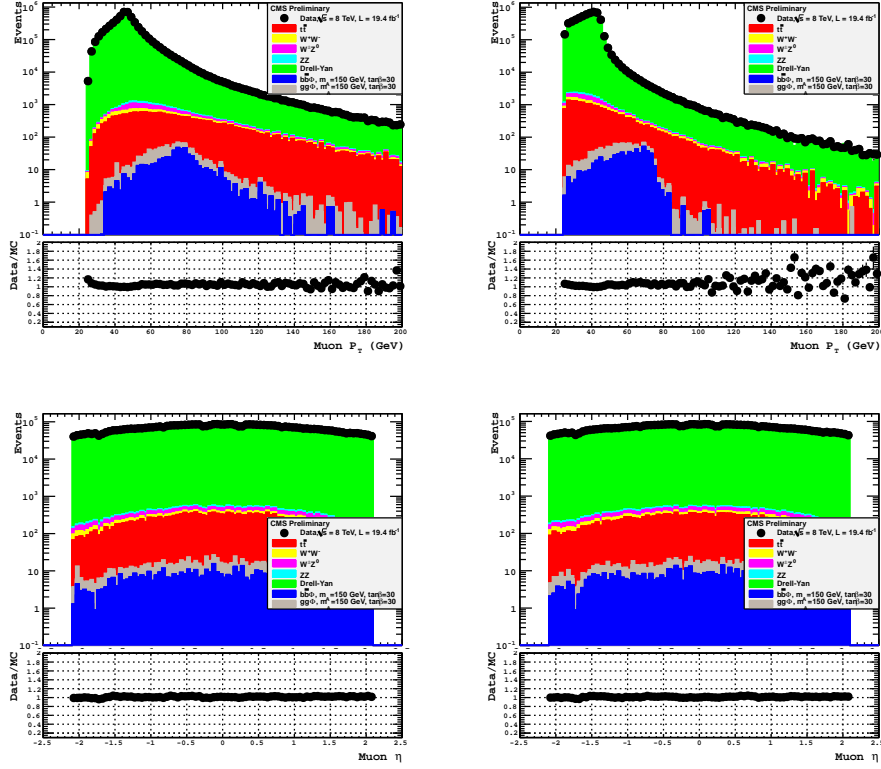


Figure 5.4: *The distribution of the highest and second-highest transverse momentum of the muons candidates (top left and top right respectively). Distribution of the pseudorapidity  $\eta$  of the highest and second-highest transverse momentum muon (bottom left and bottom right respectively) at  $\sqrt{s} = 8$  TeV. The black points correspond to the data, while the coloured stacked histograms are in green for the  $DY$  component, in red for the  $t\bar{t}$ , and in the other colors for the less relevant background sources as indicated in legend. The signal histograms are superimposed: in blue the  $b\bar{b}\Phi$  events and in grey the  $g\bar{g}\Phi$ . For each plot the ratio between data and background simulated events is shown.*

For each plot the ratio between data and background simulated events is shown, to quantify the data-MC agreement. This is very good for the pseudorapidity distribution in all the  $\eta$  range, and just as good for the  $p_T$  and mass distributions in all the range apart the tails, that suffer from low statistics. The good agreement vali-

dates the hypotheses concerning the background that affects this analysis. Nevertheless the background is directly estimated from data and these plots are meant for illustration only.

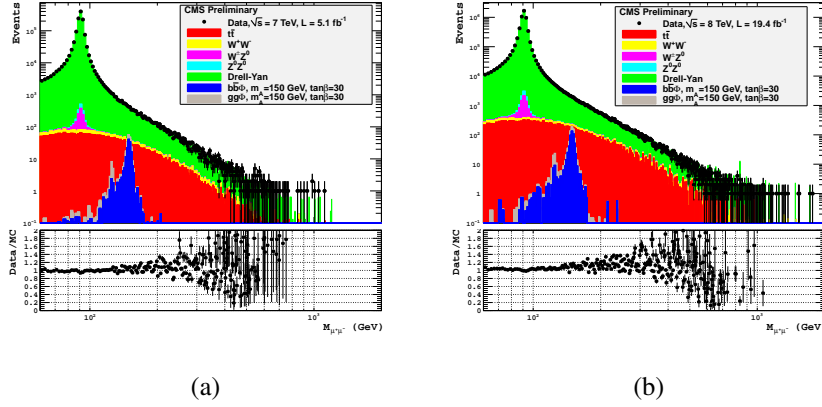


Figure 5.5: Distributions of the invariant mass of the dimuon pairs for tracks that pass the muon selection criteria at  $\sqrt{s} = 7 \text{ TeV}$  (a) and  $\sqrt{s} = 8 \text{ TeV}$  (a). The ratio between the data and the background simulated events is also shown in each case.

Since the reconstructed invariant mass for the signals is assumed to be in the range between 100 and 500 GeV, after the muon selection, only the events with invariant mass  $M_{\mu^+\mu^-} > 60 \text{ GeV}$  are kept.

### 5.2.5 Missing transverse energy selection

Since the presence of neutrinos from  $t$ -quark semi-leptonic decay characterises the final state of the  $t\bar{t}$  production, the selection based on  $E_T^{\text{miss}}$  provides a good separation between the signal events and the  $t\bar{t}$  background.

In this analysis the  $E_T^{\text{miss}}$  computed by the PF algorithm (PFMet), described in section 3.3.6, is used.

The  $E_T^{\text{miss}}$  distribution of data superimposed to the expected background and signal is shown in Fig. 5.6 for events with  $M_{\mu^+\mu^-} > 60 \text{ GeV}$  that pass the muon selection, produced at  $\sqrt{s} = 7 \text{ TeV}$  Fig. 5.6(a) and  $\sqrt{s} = 8 \text{ TeV}$  Fig. 5.6(b).

The selection veto  $E_T^{\text{miss}} < 35 \text{ GeV}$ , employed in this analysis, is estimated to provide the best significance in the presence of a signal, as shown in Fig. 5.7.

It is interesting to note that, for the chosen value, the significance at  $\sqrt{s} = 7$  TeV is slightly higher than at  $\sqrt{s} = 8$  TeV, so the  $E_T^{\text{miss}}$  cut rejects more events of the signal at  $\sqrt{s} = 8$  TeV than at  $\sqrt{s} = 7$  TeV. It happens because the  $E_T^{\text{miss}}$  distribution becomes broader as the centre-of-mass energy increases, especially for Drell-Yan and signal events.

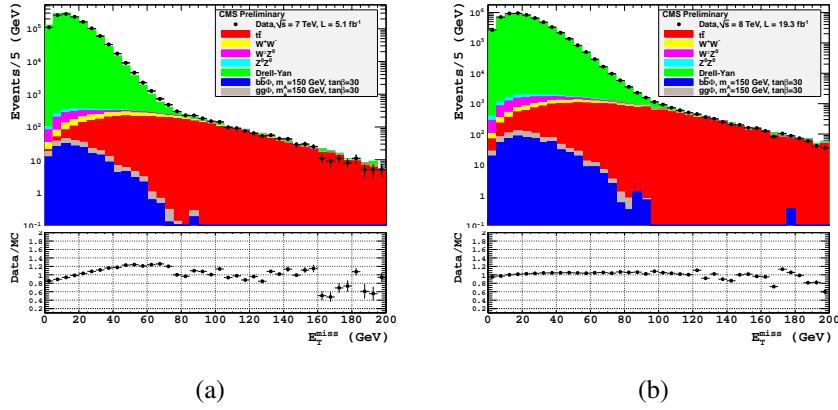


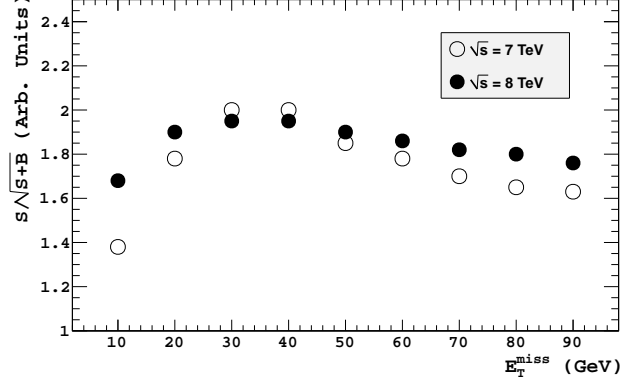
Figure 5.6: The  $E_T^{\text{miss}}$  distribution for data and simulated events at  $\sqrt{s} = 7$  TeV (a) and  $\sqrt{s} = 8$  TeV (b). The ratio between the data and the background simulated events is also shown.

### 5.2.6 $b$ -jets selection

The events selected by the previous criteria are split into two distinct categories, according to the presence or absence of  $b$ -tagged jets. This is done to obtain the highest sensitivity for both Higgs production processes:

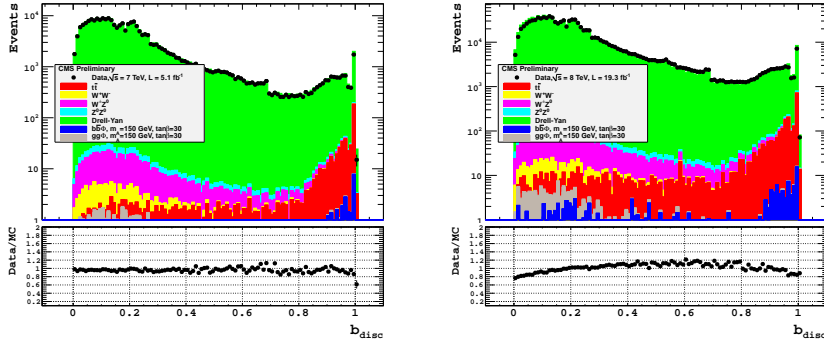
- The events with at least one  $b$ -tagged jet belong to the so-called Category 1 (Cat.1). These events are meant to provide the highest sensitivity for the  $b$ -associated production, whose feynman diagram is sketched in Fig. 4.3 (left).
- Events that do not contain  $b$ -tagged jets are assigned to Category 2 (Cat.2). These events, to whom no further cut are applied, provide the best sensitivity for the inclusive gluon fusion production, shown in Fig. 4.3 (right).

## 5. Event selection



(a)

Figure 5.7: The dependence of the significance of the MSSM Higgs signal, computed as  $S/\sqrt{S+B}$ , as a function of the  $E_T^{\text{miss}}$  selection cut, at  $\sqrt{s} = 7$  TeV and  $\sqrt{s} = 8$  TeV. The scale in the y axis is arbitrary, as the plots is meant to show the dependence on the  $E_T^{\text{miss}}$  selection value, and not its absolute value.



(a)

(b)

Figure 5.8: The  $b_{\text{disc}}$  distribution for events that pass the selection  $E_T^{\text{miss}} < 35$  GeV for data collected at  $\sqrt{s} = 7$  TeV (a) and  $\sqrt{s} = 8$  TeV (b). Data and simulated events are superimposed. The ratio between the data and the background simulated events is also shown in each case. The selection cut  $b_{\text{disc}} > 0.679$  is used to b-tag the jets.

For this analysis the PF-jets, reconstructed with the anti- $\kappa_T$  algorithm [93] within a cone  $\Delta R = 0.5$ , are used.

The events of Cat.1 are selected if they contain at least one jet with transverse momentum  $p_T^{jet} > 20$  GeV within the pseudorapidity range  $|\eta| < 2.4$ . Then a cut on the  $b$ -tagging variable is applied. The PF-jets are  $b$ -tagged using the combined secondary vertex (CSV) discriminator, described in section 3.3.10. This algorithm computes a discriminating variable,  $b_{disc}$ , which is able to distinguish  $b$ -quark from  $c$  and light-flavour jets.

The  $b_{disc}$  distribution for the events that pass the  $E_T^{miss}$  selection, is shown in Fig. 5.8. The plot on the left is for data collected at  $\sqrt{s} = 7$  TeV, while the plot on the right for data at  $\sqrt{s} = 8$  TeV. The expected distributions for signal and background processes are superimposed. PF-jets are considered  $b$ -tagged if their associated  $b_{disc}$  is larger than 0.679. This value allows to discard a large amount of Drell-Yan background events without significant effect on the signal produced in association with a  $b$ -pair. Most of the discarded signal is produced by gluon fusion, but, because events that fail these requests belong to Cat.2, no event is lost.

After the categorization, in order to remove from Cat.1 some rare  $b$ -tagged jet produced in pile-up interactions, the *PU-Jet identification* [94] is applied.

This algorithm exploits a set of discriminating variables related to three types of characteristics of the PF-jets:

- **the trajectories of tracks associated to the jets**, inside the tracker acceptance, are used to establish the compatibility of the jet with the PV;
- **the jet shape** is used to disentangle jets arising from the overlap of multiple interactions from truly hard jets;
- **the jet multiplicity**.

These informations are used as input to a *Boosted Decision Tree* algorithm [94] that returns a discriminating variable,  $PU_{id}^{jet}$ , used to discard events from PU interactions. Figure 5.9 shows the  $PU_{id}^{jet}$  distribution for the  $b$ -tagged jets of Cat.1: in case two or more jets are  $b$ -tagged in an event, the one with the highest  $b_{disc}$  is shown. The selection requires a  $PU_{id}^{jet} > 0$ , to ensure that no jets from PU

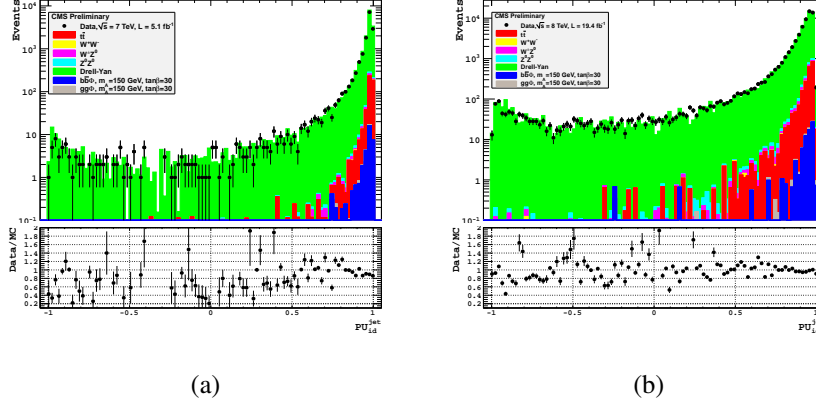


Figure 5.9: The distribution of the variable  $PU_{id}^{jet}$  for the  $b$ -tagged jet in the event, for data and simulated events at  $\sqrt{s} = 7$  TeV (a) and  $\sqrt{s} = 8$  TeV (a).

are kept. This cut has no effects on the jets that already pass the  $b$ -tag selection, except for very rare events.

A further cut is applied to reject events with more than two  $b$ -tagged jets to further suppress the  $t\bar{t}$  background, without having sensible effects on the signal, as shown in Fig. 5.10.

Figure 5.11 shows the transverse momentum distribution of the  $b$ -tagged jet with the highest  $b_{disc}$  in the events at  $\sqrt{s} = 7$  TeV (a) and  $\sqrt{s} = 8$  TeV (b), where the expected distributions for the signal and background processes are superimposed.

### 5.2.7 Dimuon spectrum

The dimuon invariant mass distributions for events that pass all the selection cuts and belong to Cat.1 and Cat.2 are shown in Fig. 5.12 for data and simulated events at  $\sqrt{s} = 7$  TeV. The same quantities are shown in Fig. 5.13 for  $\sqrt{s} = 8$  TeV.

As it is visible by eye, the data do not contain any excess of events over the background in the mass region where the blue and grey histograms are shown. In order to evaluate the probability to see or to exclude the expected signal, statistical studies performed as detailed in the next chapter.

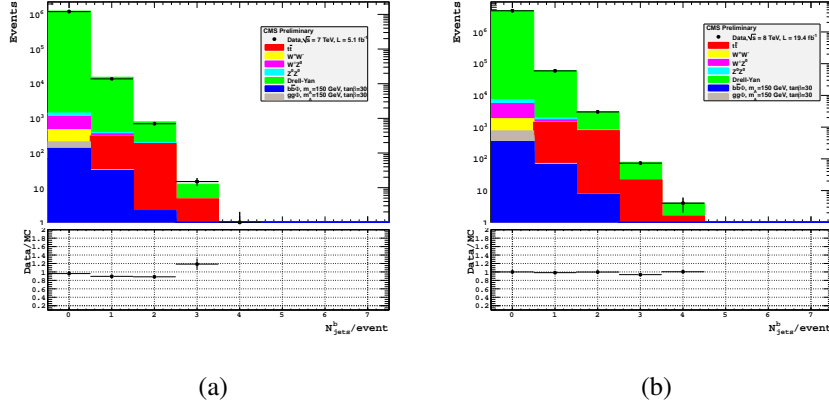


Figure 5.10: The distribution of the number of  $b$ -tagged jets per event after the  $E_T^{\text{miss}}$  selection, for data and simulation at  $\sqrt{s} = 7 \text{ TeV}$  (a) and  $\sqrt{s} = 8 \text{ TeV}$  (b). Events with more than two  $b$ -tagged jets,  $N_{\text{jets}}^b > 2$ , are rejected to further suppress the  $t\bar{t}$  background.

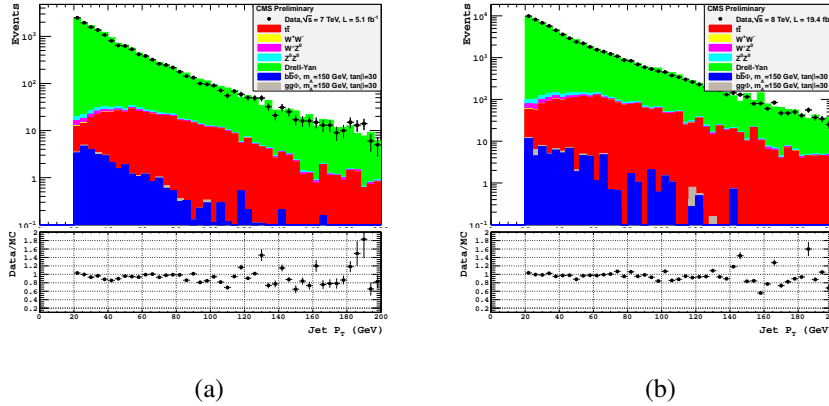
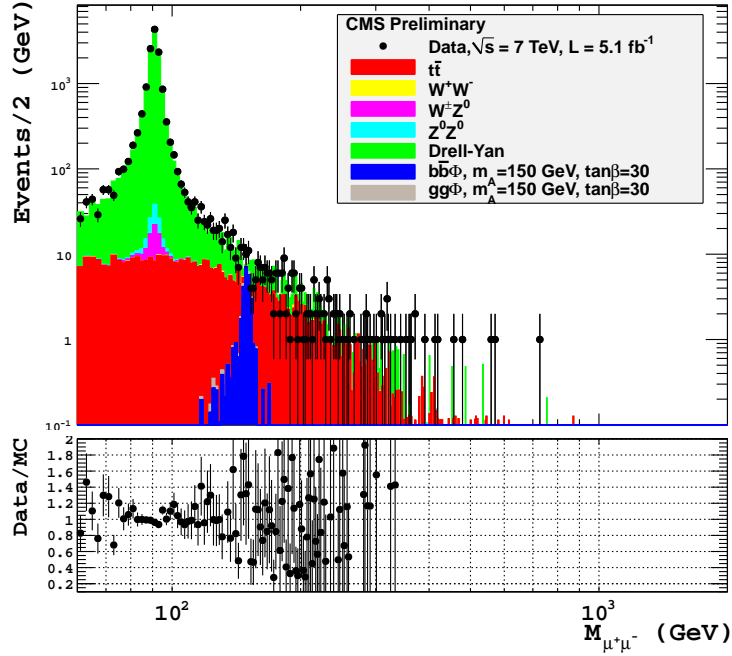


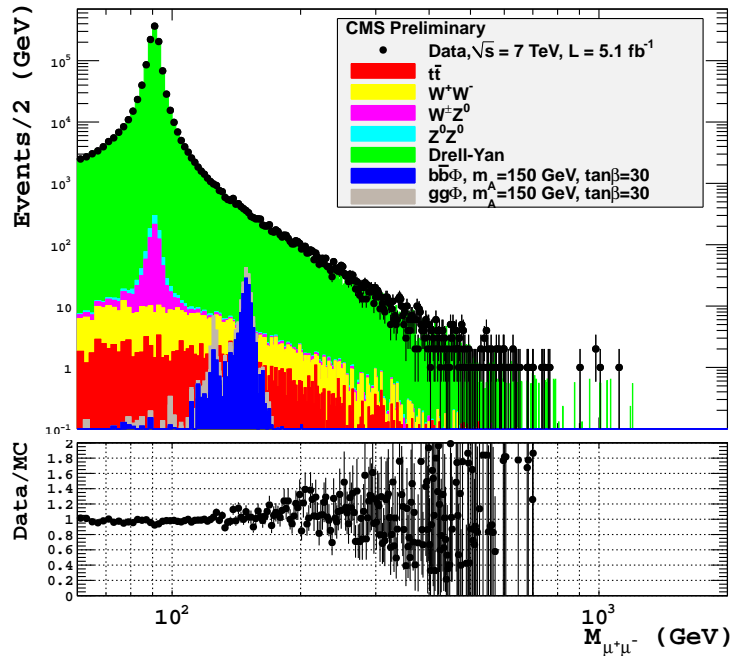
Figure 5.11: The distribution of the transverse momentum of the  $b$ -tagged jet with the highest  $b_{\text{disc}}$  in the event for data and simulation at  $\sqrt{s} = 7 \text{ TeV}$  (a) and  $\sqrt{s} = 8 \text{ TeV}$  (b).

In general the plots show a good data-MC agreement, especially at the  $Z$  peak, around 90 GeV. The fluctuations in the high mass region are due from low number of events. Because of this, the mass range where the results are computed is

## 5. Event selection

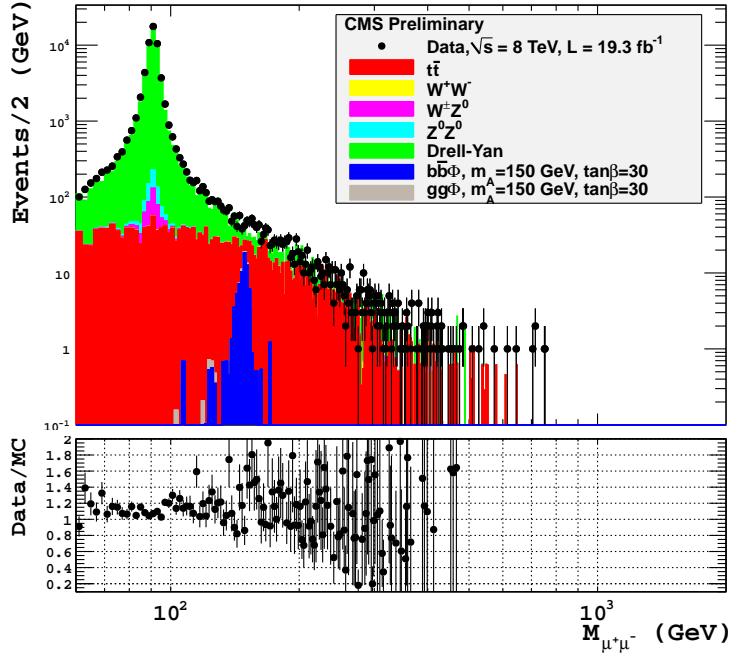


(a)

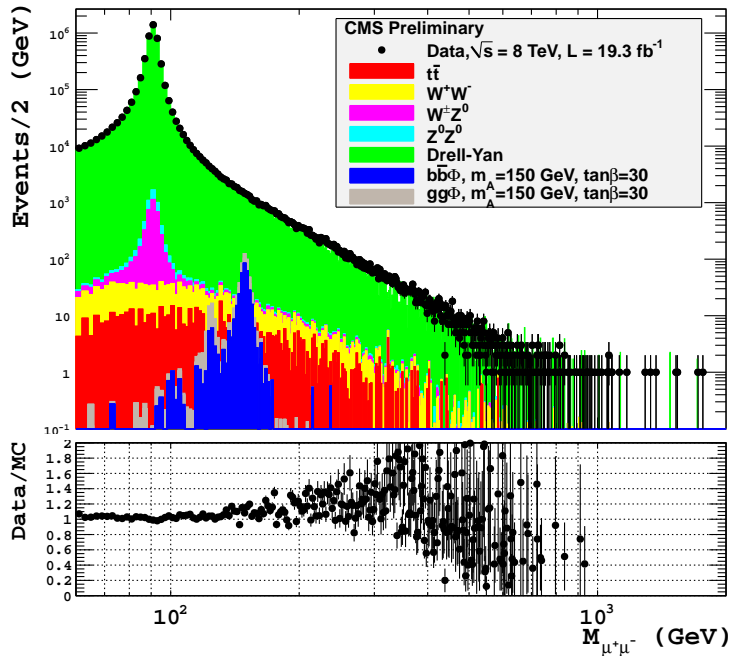


(b)

Figure 5.12: The dimuon invariant mass distribution for events that belong to Cat.1 (a) and Cat.2 (b) for data and simulated events at  $\sqrt{s} = 7$  TeV. The black points correspond to the data while the coloured stacked histograms to the background components. The signal histograms in blue and grey are superimposed.



(a)



(b)

Figure 5.13: The dimuon invariant mass distribution for events that belong to Cat.1 (a) and Cat.2 (b) for data and simulated events at  $\sqrt{s} = 8$  TeV. The black points correspond to the data while the coloured stacked histograms to the background components. The signal histograms in blue and grey are superimposed.

## 5. Event selection

---

set between 100 and 300 GeV. As expected, most of the remaining background comes from the Drell-Yan events. This fraction is minor for Cat.1, where the b-tag selection discards all the Drell-Yan events not produced in association with a b-quark, which instead belong to Cat.2.

# Chapter 6

## Results

The dimuon mass distributions, obtained analysing data and simulated signal samples, are used for a statistical treatment of results. This procedure is aimed at testing the presence of a signal.

The strategy followed in this analysis exploits a modified-frequentist CLS method, as recommended by the LHC HCG group [51,52]. To search for a signal, the null hypothesis,  $H_0$ , is defined as describing only known processes, here designated as background. This is to be tested against the alternative  $H_1$ , which includes both background and the searched signal. When setting limits, the model with signal plus background plays the role of  $H_0$ , which is tested against the background-only hypothesis,  $H_1$ .

The outcome of such a search consists in the quantification of the agreement between the observed data with a given hypothesis  $H$  by computing a p-value or its equivalent Gaussian significance. The p-value is a probability, under assumption of  $H$ , of finding data of equal or greater incompatibility with the predictions of  $H$ . In particle physics the p-value is usually converted into an equivalent significance,  $Z$ , defined such as a Gaussian distributed variable, found  $Z$  standard deviations above its mean, has an upper-tail probability equal to  $p$ :

$$Z = \phi^{-1}(1 - p) \quad (6.1)$$

where  $\phi^{-1}$  is the quantile function (inverse of the cumulative distribution) of the standard Gaussian.

To define a discovery of a new signal process, as for example the Higgs boson, the particle physics community requires rejection of the background hypothesis

with a significance of at least  $Z = 5$ , usually indicated as  $5\sigma$ , where  $\sigma$  is the standard deviation of the Gaussian. This corresponds to  $p = 2.87 \cdot 10^{-7}$ . For purposes of excluding a signal hypothesis, a threshold p-value of 0.05 (i.e., 95% confidence level) is often used, which corresponds to  $Z = 1.64$ .

This analysis adopts a data driven approach, in which the background contribution is estimated by a fit to the data. The invariant mass distributions of the events that belong to Cat.1 and Cat.2 are used to determine the background shape.

The signal shape, for each  $m_A$  and  $\tan\beta$  value listed in Tab. 5.3, is instead estimated by a fit to MC samples. These invariant mass distributions are properly weighted to account for data-simulation discrepancies, as described in sec.6.1.

The cross sections and the branching ratios, used to scale the MC signals with respect to the data luminosity, are computed with FeynHiggs by the LHC cross section group [12].

The selection efficiency is affected by systematic uncertainties. They are taken into account including in the test nuisance parameters that follow a log-normal distribution. It is assumed that the parametric model is sufficiently flexible so that for some values of the nuisance parameters it can be regarded as true.

### 6.1 Signal efficiency

The selection efficiency is defined as the fraction of initial events that pass the analysis cuts.

In the case of signal efficiency, this is determined by applying the event selection criteria to the simulated signal samples listed in Tab. 5.3.

Figure 6.1 shows the signal efficiency at the end of the selection for the  $b\bar{b}\Phi$  process at  $\sqrt{s} = 8$  TeV summing the two event categories, whereas Fig. 6.1 shows the same quantity for the  $gg\Phi$  process.

In the case of the b-associated production, since the efficiency does not depend significantly on  $\tan\beta$ , 1-dimensional plots are used, where the dark-red area represents the variation of the efficiency in the full  $\tan\beta$  range.

As an example, the selection efficiency in the case  $m_A = 150$  GeV and  $\tan\beta = 30$  is shown in Tab. 6.1, for events at  $\sqrt{s} = 7$  and 8 TeV. The quoted values have been computed with respect to the number of simulated events (2000). The fraction of data events passing the same selection criteria is also listed for illustration.

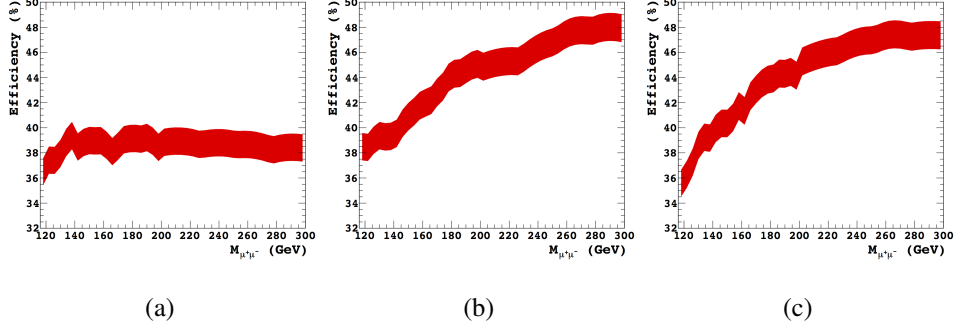


Figure 6.1: Signal efficiency for the  $b$ -associated production process at  $\sqrt{s} = 8$  TeV, separately for the three  $\Phi$  boson types,  $h$  (a),  $H$  (b) and  $A$  (c), as function of their reconstructed mass. The two event categories are added. The dark-red area represents the variation of the efficiency in the full  $\tan \beta$  range.

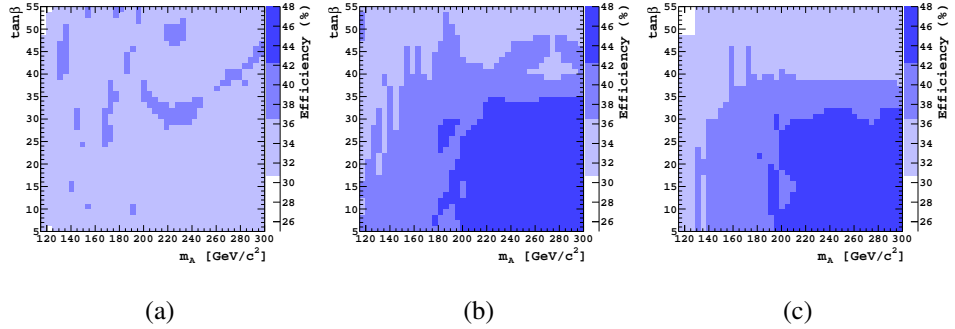


Figure 6.2: Signal efficiency for the gluon-gluon production process at  $\sqrt{s} = 8$  TeV, separately for the three  $\Phi$  boson types,  $h$  (a),  $H$  (b) and  $A$  (c), in the  $m_A - \tan \beta$  plane. The two event categories are added together.

The overall efficiency has to be corrected to take into account the data-MC discrepancy. This is evaluated step by step during the event selection and scale factors are applied to smooth the small differences that can occur between data and simulation. These factors, concerning muons [95] and  $b$ -tagging [96], are provided by the CMS collaboration and are calculated from data-MC comparisons in dedicated analyses. These are relative to the single object, as for example muon, jet, etc. Since scale factors relative to the full event are needed, they are computed

Sample	Selection	Tot. Eff. (%)		Rel. Eff. (%)	
		7 TeV	8 TeV	7 TeV	8 TeV
$b\bar{b}A$	$E_T^{\text{miss}}$	94.0	73.2	94.0	73.2
	Cat.1	16.7	12.6	17.8	17.2
	Cat.2	70.7	60.5	75.2	82.7
$ggA$	$E_T^{\text{miss}}$	99.1	78.1	99.1	78.1
	Cat.1	1.9	1.4	1.9	1.8
	Cat.2	93.4	76.7	94.2	98.2
Data	$E_T^{\text{miss}}$	93.2	83.2	93.2	83.2
	Cat.1	1.1	1.1	1.2	1.3
	Cat.2	92.1	82.1	99.0	98.7

Table 6.1: *Event selection efficiency obtained before categorization (after  $E_T^{\text{miss}}$  cut), and after the splitting in two categories (Cat.1 and Cat.2). The values of the total efficiency are calculated with respect to the events which pass the dimuon selection step, while the relative efficiency is evaluated with respect to the number of events before the categorization. The results are given for  $m_A = 150$  GeV,  $\tan\beta = 30$ , separately for  $\sqrt{s} = 7$  TeV and  $\sqrt{s} = 8$  TeV. The corresponding fraction of selected events for the inclusive dataset are given for comparison.*

as described below.

**The HLT efficiency** is evaluated after the HLT emulation. The scale factor to correct the MC with respect to the data is relative to each muon, and depends on its pseudorapidity and transverse momentum:

$$\epsilon^D = \epsilon^{MC} \cdot w^{HLT}, \quad (6.2)$$

where  $\epsilon^D$  and  $\epsilon^{MC}$  are the efficiency calculated on data and MC and  $w^{HLT}$  is the scale factor for the HLT part. As each event contains two muons and it is enough that one of the muon fires the trigger, the efficiency can be expressed as:

$$\epsilon = 1 - (1 - \epsilon_1)(1 - \epsilon_2), \quad (6.3)$$

where 1 and 2 are relative to the muons. So the total scale factor for each event is assigned according to:

$$(1 - \epsilon_1^D)(1 - \epsilon_2^D) = (1 - \epsilon_1^{MC} w_1^{HLT})(1 - \epsilon_2^{MC} w_2^{HLT}). \quad (6.4)$$

The distribution of the event weights for the HLT efficiency is shown in Fig. 6.3 (a). It is relative to the signal sample with  $m_A = 150$  GeV and  $\tan \beta = 30$ .

**The muon reconstruction efficiency** evaluates how many events, whose muon fires the HLT, effectively contain two reconstructed tight PF-muons. To take into account data-simulation discrepancy a scale factor is assigned to each muon candidate. Since each event contains two muons, a weight  $w^{eff}$ , calculated as a product of the two scale factors, is assigned to each event. Its distribution is shown in Fig. 6.3 (b) for the same signal sample mentioned above. The average value of the distribution is 0.989.

**The isolation efficiency** accounts how many reconstructed muons are isolated. Also in this case, an event weight  $w^{iso}$  is assigned to each event as the product of the scale factors relative to the two muons. The distribution of this event weight for the signal taken as example is shown in Fig. 6.3 (c). The average value of the distribution is 0.995.

**The  $b$ -tagging efficiency** takes into account the  $b$ -jet identification and mistagging rate. The first case includes the reconstructed  $b$ -jets effectively coming from the fragmentation of a  $b$ -quark, while the second case accounts for  $b$ -tagged jets coming from a different particle.

To account for the difference with respect to the data, the efficiency of the simulated signal samples is scaled by a factor which depends on the jet transverse momentum. Similarly to the previous cases, a weight  $w^{btag}$  is assigned to each event. In this case it corresponds to the scale factor of the jet with the highest  $b$ -tag discriminator. The distribution of this quantity for the signal case chosen as example is shown in Fig. 6.3 (d).

All of the event weights are very close to unity, since also the initial scale factor are so. This confirms that the simulation well reproduces data. The weights are applied all together as a total multiplicative weight to scale the reconstructed mass distributions of the signal samples before performing the fit (discussed in sec.6.4.1). Its effect does not determine big changes in the distributions shown in the previous chapter.

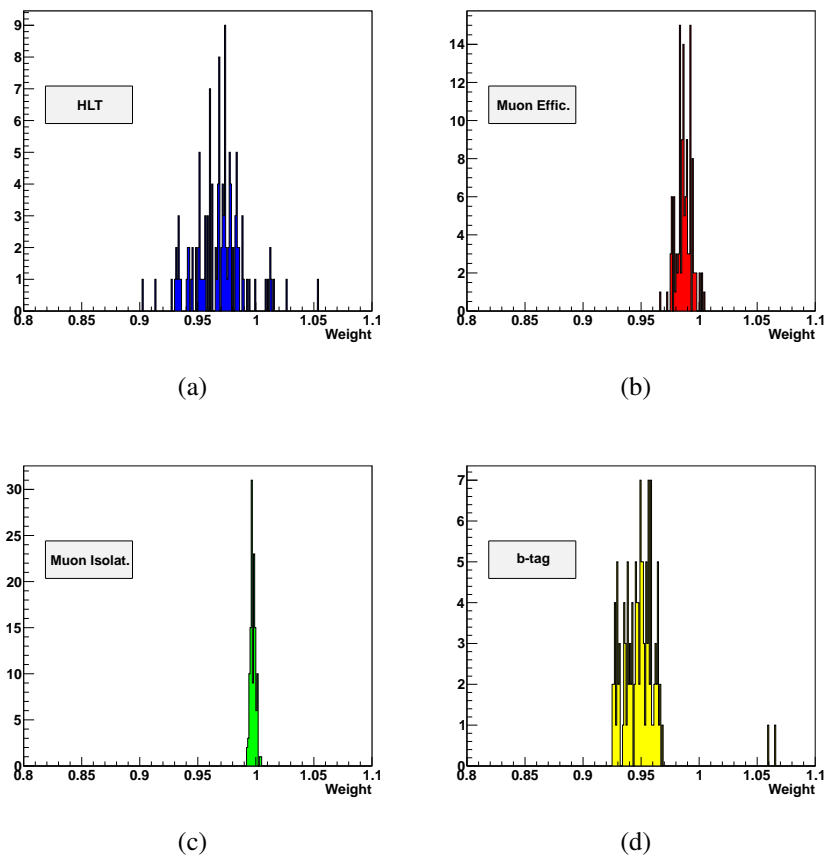


Figure 6.3: *Distribution of the weights assigned to each simulated signal event, for HLT (a), muon reconstruction (b), isolation (c) and b-tagging (d) efficiencies.*

## 6.2 Systematic uncertainties

The systematic errors are related to the set of measurements of the physics object properties, which are exploited for the selection cuts, as for example the muon isolation measurement, the jet energy measurement, etc. They are characteristic of the type of measurement, and are independent by each other. Their effect is evaluated on the signal efficiency and is assigned as nuisance parameter in the statistical test.

At first, because the signal efficiency is evaluated on simulated samples with a limited number of events, 2000 in this case, it gives a statistical uncertainty of

1.0%.

Uncertainties related to the muon identification, isolation and HLT are associated with the precision of the scale factors mentioned in the previous paragraph. The systematic uncertainty for the HLT efficiency is 0.5% whereas for the muon identification and isolation it is 1.0%.

The uncertainty due to PU is estimated by varying up and down the number of PU interaction of  $\pm 5\%$  with respect to the estimated mean value. The effect on the signal efficiency is evaluated at the end of selection. The observed variation is  $\pm 0.8\%$ .

The Jet Energy Scale (JES) uncertainty is estimated by smearing the jet momentum of a factor depending on  $p_T$  and  $\eta$  of each jet [97]. The effect is  $\pm 4.0\%$  for events that belong to Cat.1 and  $\pm 0.5\%$  for Cat.2, at  $\sqrt{s} = 8$  TeV. For  $\sqrt{s} = 7$  TeV the corresponding numbers are  $\pm 3.8\%$  and  $\pm 0.6\%$ .

The uncertainty related to the  $b$ -tag algorithm is computed taking into account an error of 3.0% on the  $b$ -tagging efficiency and an error of 10% on the mistag rate. Their overall contribution to the total systematic uncertainty is weighted to the relative amount of  $b\bar{b}\Phi$  and  $gg\Phi$  events, in turn depending on  $m_A$  and  $\tan\beta$ . The largest effect is 3.0% for Cat.1, and 0.4% for Cat.2.

The uncertainty on the transverse missing energy is estimated by propagating the uncertainty of each object used in the  $E_{\text{miss}}^T$  computation. The effect on the signal efficiency is  $\pm 3.0\%$  at  $\sqrt{s} = 8$  TeV and  $\pm 2.0\%$  at  $\sqrt{s} = 7$  TeV.

The uncertainty on the integrated luminosity is 2.2% at  $\sqrt{s} = 7$  TeV and 2.6% at  $\sqrt{s} = 8$  TeV as provided by the CMS collaboration [98].

The uncertainties on the Parton Distribution Functions and the strong coupling constant  $\alpha_s$  affect the production cross section of the MSSM Higgs boson. They are determined as explained in [99] and they are estimated to be 3.0%.

A further source of uncertainty is related to the fitting methods. This systematic error is smaller than 12% for Cat.1 and smaller than 7.0% for Cat.2., and it is accurately discussed in the paragraph 6.4.4.

Table 6.2 summarises all the systematic uncertainties on the signal efficiency.

Source	Systematic Uncertainty (%)	
	Cat.1	Cat.2
MC Statistics	1.0	1.0
HLT	0.5	0.5
Muon efficiency	1.0	1.0
Muon Isolation	1.0	1.0
Pile-up reweight	0.8	0.8
b-tag	3.0	0.4
Jet Energy Scale	4.0 (3.8)	0.5 (0.6)
$E_T^{\text{miss}}$	3.0 (2.0)	3.0 (2.0)
Integ. Luminosity	2.6 (2.2)	2.6 (2.2)
PDF and $\alpha_s$	3.0	3.0
Fitting method	$\leq 12$	$\leq 7.0$

Table 6.2: Systematic uncertainties that affect the signal efficiency. The values in parenthesis refer to  $\sqrt{s} = 7 \text{ TeV}$ .

### 6.3 FeynHiggs calculation of cross sections, masses and widths

As already mentioned the precision achieved by FeynHiggs in the cross section, mass and width calculation is higher than the one obtained with Pythia generator. Moreover the signal samples are generated with Pythia only within the  $m_h^{\text{max}}$  scenario, whereas we are also interested to study the  $m_h^{\text{mod+}}$  and  $m_h^{\text{mod-}}$ . Therefore the invariant mass distributions of the three Higgs bosons, obtained analysing the Pythia samples, are opportunely shifted according to the mass values computed by FeynHiggs in the corresponding scenario (Fig.5.1). This can be done since the differences in the predicted widths between Pythia and FeynHiggs are within the experimental resolution (Fig.5.2).

The parameters used to compute the cross section, mass and width of the  $\Phi$  bosons are listed in eq. 4.1 for the  $m_h^{\text{max}}$  benchmark, and in eq. 4.5 for  $m_h^{\text{mod+}}$  and  $m_h^{\text{mod-}}$ .

The calculation of the mass of the light MSSM Higgs boson  $h$  is shown in

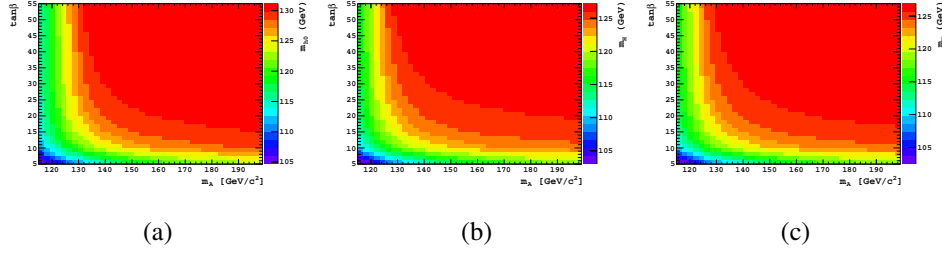


Figure 6.4: *FeynHiggs* values of  $m_h$  expressed in the coloured scale (on the right of plot) as function of  $m_A$  and  $\tan \beta$  for the three scenarios  $m_h^{\max}$  (left),  $m_h^{\text{mod}+}$  and  $m_h^{\text{mod}-}$ . In the plot (a) the red color reaches the value of 135 GeV, about 5 GeV higher than in the plot (b) and (c).

Fig. 6.4 in the  $m_A - \tan \beta$  plane. The results for the three benchmark scenarios are shown. In the  $m_h^{\text{mod}}$  scenarios the value of  $m_h$  is about 125 GeV for a large fraction of the  $m_A - \tan \beta$  values, and thus is consistent with the measured mass of the SM Higgs boson. On the contrary the  $m_h^{\max}$  scenario provides values of  $m_h$  that are  $\approx 5$  GeV higher.

The production cross section of the three  $\Phi$  boson types via the gluon-gluon fusion process is reported in Fig. 6.5 as a function of  $m_A$ . The two cases  $\sqrt{s} = 7$  and 8 TeV are shown. The calculations are performed assuming  $\tan \beta = 20$ . The results for the three benchmark scenarios  $m_h^{\max}$ ,  $m_h^{\text{mod}+}$  and  $m_h^{\text{mod}-}$  are superimposed.

Similarly the production cross section of the three  $\Phi$  boson types via the  $b$ -associated production process is reported in Fig. 6.6 as a function of  $m_A$ .

## 6.4 Fitting procedure

The sum of the signal and background, both described with the help of free parameters, allows to estimate the amount of signal and background contained in data for a given signal hypothesis. The background is entirely estimated by a fit to the data, while the signal is estimated by a fit to the MC distributions. In order to perform an homogeneous sum of signal and background functions, the signal distributions are scaled by the weights described in sec.6.1 to account for MC-data

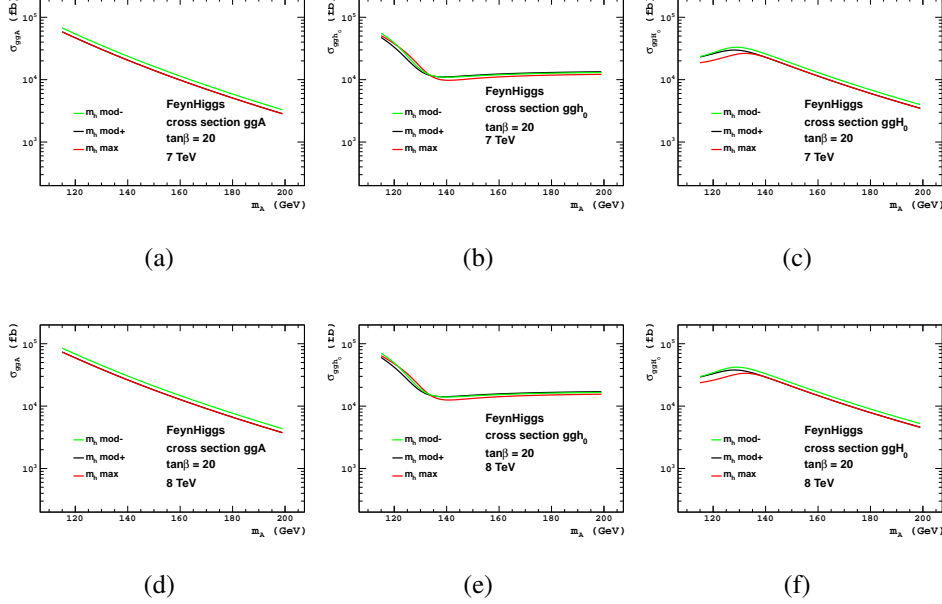


Figure 6.5: The production cross section of the three  $\Phi$  bosons via the gluon-gluon fusion process as a function of  $m_A$ . The predictions for  $\sqrt{s} = 7$  are shown in the top plots while the ones at 8 TeV in the bottom plots. The calculations are performed for  $\tan\beta = 20$ . The results for the three benchmark scenarios  $m_h^{max}$  (red),  $m_h^{mod+}$  (black) and  $m_h^{mod-}$  (green) are superimposed.

discrepancy.

### 6.4.1 Signal description

The total Higgs signal, for each  $m_A$  and  $\tan\beta$  value, is obtained as mentioned in the sec.5.1, and its shape is well described by the function  $F_{sig}$ . This is defined as a linear combination of three Breit-Wigner (BW) functions, one for each  $\Phi$  boson, convoluted with a Gaussian function to account for the detector resolution. Since the three functions are called  $F_h$ ,  $F_H$  and  $F_A$ , the function  $F_{sig}$  can be written as:

$$F_{sig} = w_h \cdot F_h + w_H \cdot F_H + (1 - w_h - w_H) \cdot F_A, \quad (6.5)$$

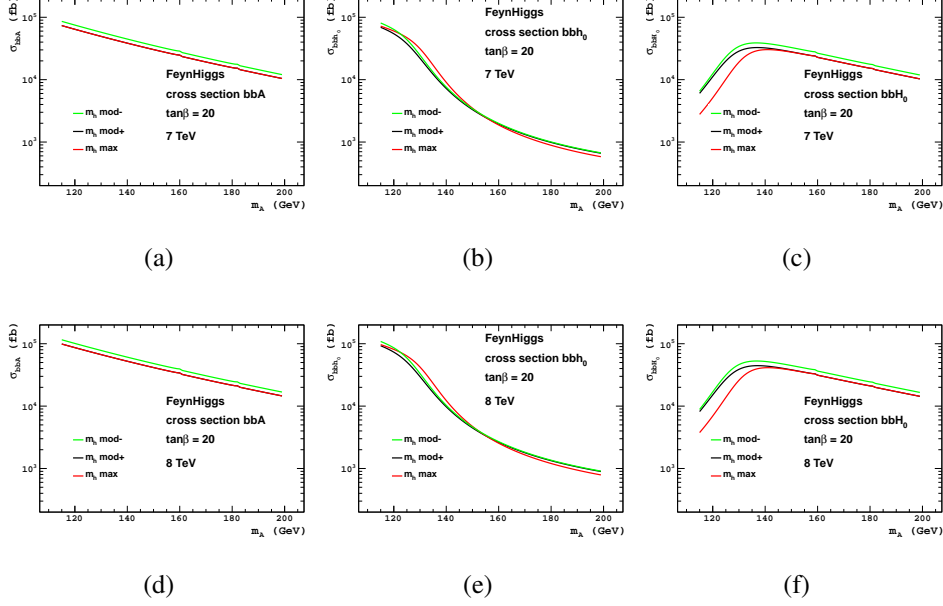


Figure 6.6: Cross section of the three  $\Phi$  bosons of the  $b$ -associated production process as a function of  $m_A$ . The predictions for  $\sqrt{s} = 7$  are shown in the top plots while the ones at 8 TeV in the bottom plots. The calculations are performed for  $\tan\beta = 20$ . The results for the three benchmark scenarios  $m_h^{max}$  (red),  $m_h^{mod+}$  (black) and  $m_h^{mod-}$  (green) are superimposed.

where  $w_h$  and  $w_H$  are the fractions of events with  $h$  and  $H$  in the signal samples. The  $w$  parameters, the masses and the widths of the three  $\Phi$  bosons are left to vary in the fit, as is the  $\sigma$  of the Gaussian function, that describes the mass resolution. An example of this procedure is shown in Fig. 6.7 (a), for the case  $m_A = 150$  GeV and  $\tan\beta = 30$  at  $\sqrt{s} = 8$  TeV. In this case the mass resolution is of the order of 2 GeV.

### 6.4.2 Background description

The function used to describe the background shape,  $F_{bkg}$ , is based on its main components. As the muon pairs from Drell-Yan dominate a large part of the mass spectrum  $F_{bkg}$  is modelled by a Breit-Wigner function,  $F_{DY}$ , plus the photon-exchange term  $F_\gamma$ , which is proportional to  $1/m_{\mu\mu}^2$ . Defining  $x = m_{\mu\mu}$ , the total

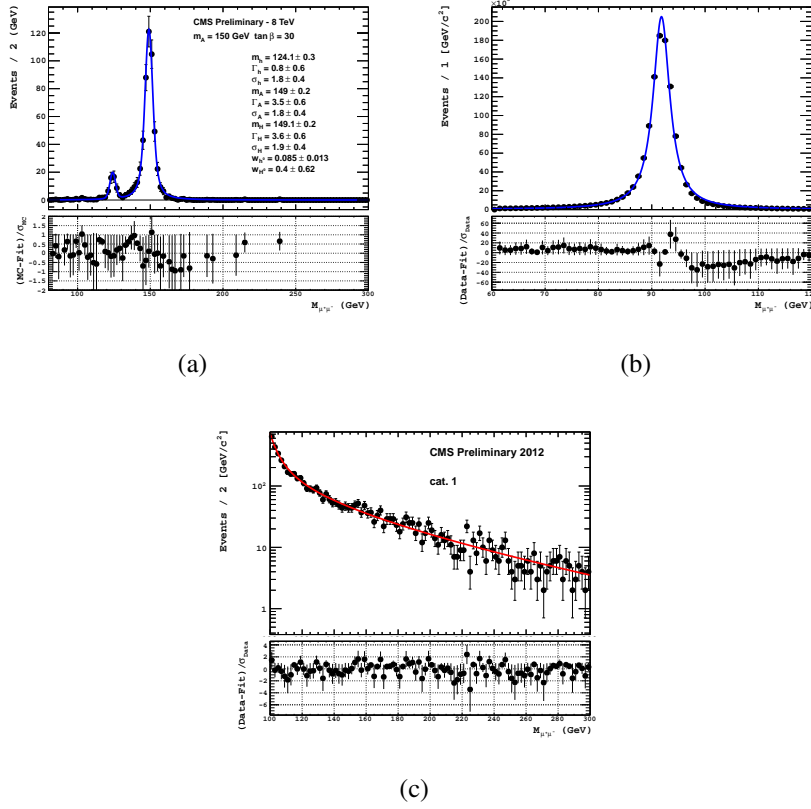


Figure 6.7: Invariant mass distribution of the expected signal after the event selection, for the case  $m_A = 150$  GeV and  $\tan \beta = 30$ , for Cat.1 (a). Fit of the dimuon invariant mass around the Z peak to determine the parameters  $\Gamma_Z$  and  $m_Z$ , used in the background parametrization (b). An example of the fit of the data with the signal assumption  $m_A = 150$  GeV and  $\tan \beta = 30$  at  $\sqrt{s} = 8$  TeV (c). For each plot the pull of the fit as a function of the muon invariant mass is shown.

$F_{bkg}$ , is:

$$F_{bkg} = N \cdot e^{\lambda x} \left[ \frac{f_Z}{N_{norm}^1} \cdot \frac{\Gamma_Z}{(x - m_Z)^2 + \frac{\Gamma_Z^2}{4}} + \frac{(1 - f_Z)}{N_{norm}^2} \cdot \frac{1}{x^2} \right] \quad (6.6)$$

where  $e^{\lambda x}$  describes the exponential part of the parton density function (PDF) and the  $N_{norm}^i$  terms are the integral of the corresponding functions. The parameters  $\Gamma_Z$  and  $m_Z$  are separately determined for Cat.1 and Cat.2 from the fit to the dimuon invariant mass distribution around the Z mass, performed in a separate

step. The fit to the Z peak is shown in Fig. 6.7 (b) for events that belong to Cat.1. The values of its free parameters,  $\Gamma_Z$  and  $m_Z$  are then kept constant in  $F_{bkg}$ .

### 6.4.3 Signal plus background description

The functions in sec.6.4.1,  $F_{sig}$  and in sec.6.4.2,  $F_{bkg}$ , respectively describe the hypotheses on the signal and the background shape. Their linear combination,  $F_{fit}$ , is then used to perform an unbinned fit to the data:

$$F_{fit} = (1 - f_{bkg}) \cdot F_{sig} + f_{bkg} \cdot F_{bkg}, \quad (6.7)$$

where  $f_{bkg}$  is a free parameter that quantifies the amount of background.

The goal of this fit is to find the amount of signal, which is  $1 - f_{bkg}$ , in the analysed data. It is executed keeping constants the parameters which describe the signal, previously obtained as explained in sec. 6.4.1, and also the parameters which describe the Z peak,  $\Gamma_Z$  and  $m_Z$ , determined in the separate fit shown in Fig. 6.7(b). Instead the parameters  $\lambda$  and  $f_Z$ , contained in the expression of  $F_{bkg}$  are left free to vary.

An example of this fit is shown in Fig. 6.7(c) for events that belong to Cat.1, for the signal assumption  $m_A = 150$  GeV and  $\tan \beta = 30$  at  $\sqrt{s} = 8$  TeV.

### 6.4.4 Systematic uncertainty of fit function

To compute the systematic uncertainty related to the function  $F_{fit}$ , an alternative fit procedure is followed. The entire mass range is divided in two parts: the *signal region*, where the signal mass is expected  $\pm 3\sigma$ , and the *side bands*, which is the rest of the mass range.

A new fit is performed with the background function (eq.6.6) just in the side bands, while the expected number of background events in the signal region is extrapolated ( $N_{bkg}$ ). This is done for all the  $m_A, \tan \beta$  points and compared to the number of background events in the signal region ( $N_{bkg}^{def}$ ) obtained when the default fit procedure is applied (eq.6.7). The quantity:

$$\frac{N_{bkg} - N_{bkg}^{def}}{N_{bkg}} \quad (6.8)$$

is then calculated and assigned as systematic uncertainty as reported in Tab. 6.2. Its value is lower than 12% for Cat.1 and 7% for Cat.2.

## 6.5 Limits calculation

As mentioned in the introduction to this chapter, to search for the MSSM Higgs bosons in the dimuon decay channel, a comparison is done between what is expected and what is observed. The expected value is constituted by the hypothesis of background only, while the observed comes out when the fit to the data with the  $F_{fit}$  function is done. This function represents the signal plus background hypothesis, and its  $f_{bkg}$  parameter returns the relative amount of background. The significance of possible deviations of  $f_{bkg}$  from unity is evaluated performing a statistical test using the *Asymptotic* CL algorithm [100], which takes into account systematic uncertainties as nuisance parameters. The outcome of this test is expressed in terms of Confidence Level (CL). Where the presence of background only is confirmed at 95% of probability, the signal is automatically excluded. Therefore, in absence of signal in data, the following results give an exclusion limit for MSSM neutral Higgs boson.

This test is done for each  $m_A$ - $\tan\beta$  point and the results are computed independently for the two categories and the two center-of-mass-energies.

The Confidence Level of the exclusion limit within  $m_h^{\max}$  scenario for Cat.1 and Cat.2 is shown in Fig. 6.8. The plots on the top are relative to the case  $\sqrt{s} = 7$  TeV, while those on the bottom are relative to  $\sqrt{s} = 8$  TeV. These three-dimensional plots show the CL values in a coloured scale as a function of  $m_A$  and  $\tan\beta$ .

These results can be projected in the two-dimensional ( $m_A$ - $\tan\beta$ ) plane, obtaining the exclusion limits of  $\tan\beta$  as a function of  $m_A$ . This is done taking for each  $m_A$  value the smallest  $\tan\beta$  value whose CL exceeds 95%, since the signal cross section is proportional to  $\tan\beta$ . This kind of plots are shown in the next paragraph where the combined results are presented.

The limit on the signal rate is then transformed into a limit on the production cross section times the decay branching ratio of the process  $\Phi \rightarrow \mu^+ \mu^-$  as a function of  $m_A$ , simply multiplying this rate for the predicted cross sections and decay branching ratios computed with FeynHiggs within  $m_h^{\max}$  scenario, as described in sec.6.3. These results obtained from the data of the two event categories are shown in Fig. 6.9 on the top for data collected at  $\sqrt{s} = 7$  TeV and on the bottom for data at  $\sqrt{s} = 8$  TeV.

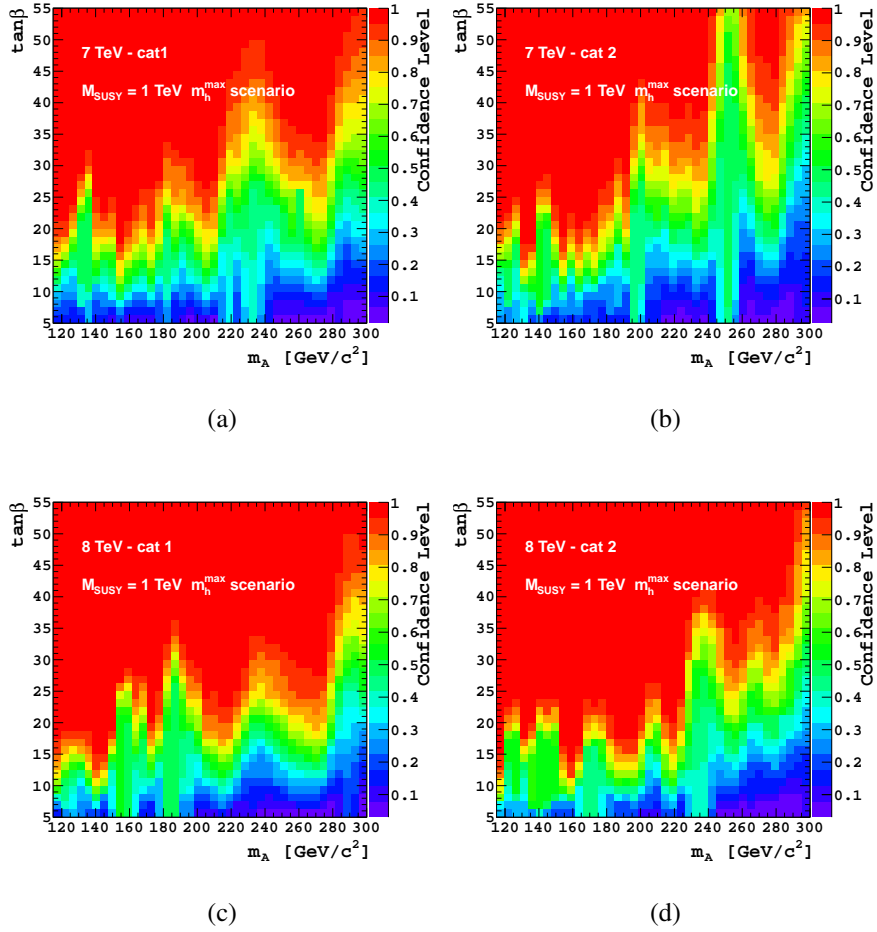


Figure 6.8: *CL of the exclusion limit in the  $(m_A, \tan \beta)$  plane for events collected at  $\sqrt{s} = 7 \text{ TeV}$  (a, b) and  $\sqrt{s} = 8 \text{ TeV}$  (c, d) separately for Cat.1 (a, c) and Cat.2 (b, d). The values of CL are given according to the coloured scale (on the right of the plot).*

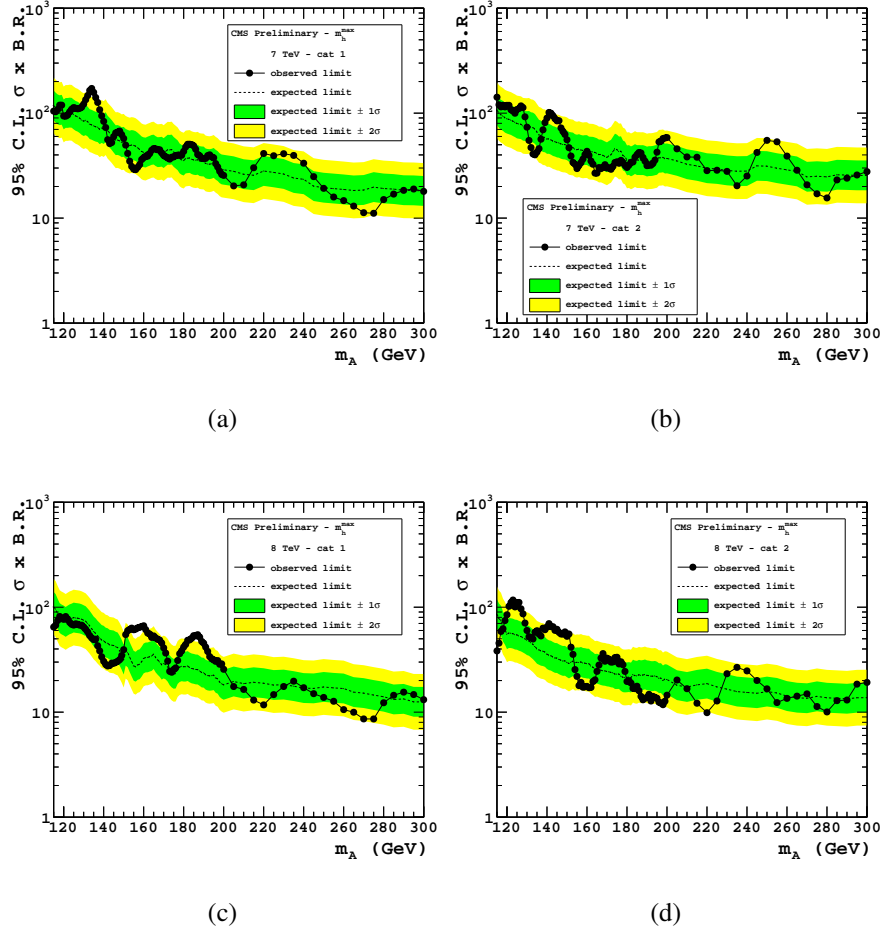


Figure 6.9: 95% CL limit on  $\sigma \times BR$  (fb) as a function of  $m_A$  for events at  $\sqrt{s} = 7$  TeV (a, b) and  $\sqrt{s} = 8$  TeV (c, d) separately for Cat.1 (a, c) and Cat.2 (b, d). The black points represent the observed background in data when a signal plus background hypothesis is done, whereas the dashed line is the expected background. The green and yellow bands represent the fluctuation ranges of  $\pm 1\sigma$  and  $\pm 2\sigma$  respectively ( $\sigma$  in this case is the standard deviation). Their width descends from the nuisance parameter.

### 6.5.1 Combined results within the $m_h^{\max}$ scenario

The results obtained within the  $m_h^{\max}$  scenario at  $\sqrt{s} = 7$  TeV and  $\sqrt{s} = 8$  TeV from the two event categories are respectively combined in order to achieve the highest sensitivity on the search of MSSM neutral Higgs boson in the dimuon decays.

The plots in Fig. 6.10 show the combination of Cat.1 and Cat.2 results for the case  $\sqrt{s} = 7$  and  $\sqrt{s} = 8$  TeV respectively. In both cases the CL of the exclusion limit as function of  $m_A$  and  $\tan\beta$  (a, d), the exclusion limit on  $\tan\beta$  as function of  $m_A$  (b, e), and the 95% CL of the limit on the production cross section times the decay branching ratio as a function of  $m_A$  (c, f) are presented.

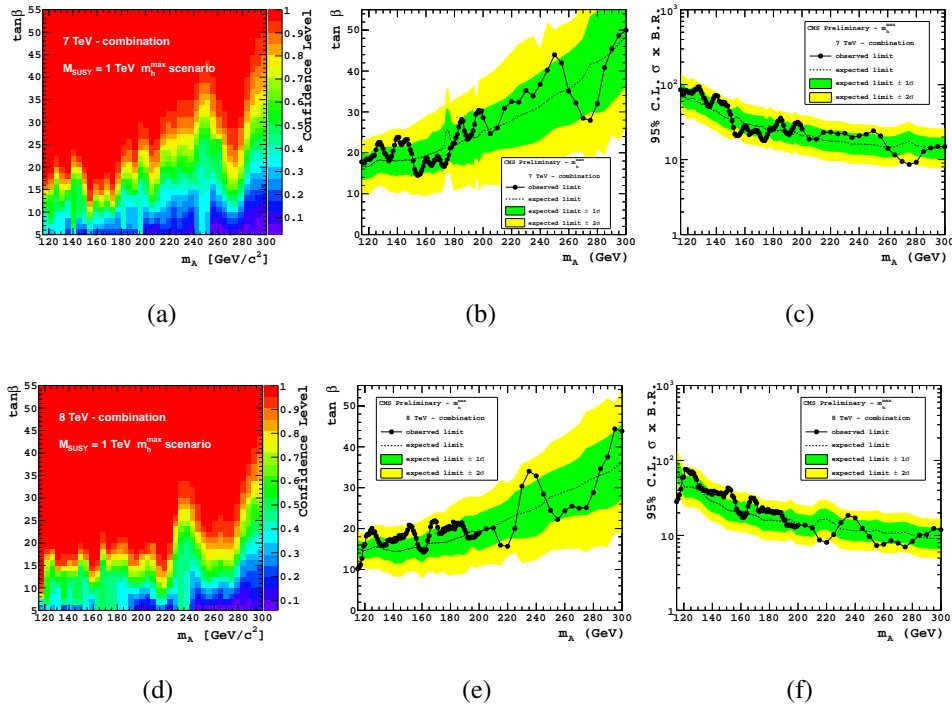


Figure 6.10: Results at  $\sqrt{s} = 7$  TeV (a, b, c) and  $\sqrt{s} = 8$  TeV (d, e, f) obtained by summing the two event categories: CL of the exclusion limit as function of  $m_A$  and  $\tan\beta$  (a, d); exclusion limit on  $\tan\beta$  as function of  $m_A$  (b, e) and 95% CL of the limit on  $\sigma \times BR$  (fb) as a function of  $m_A$  (c, f).

Figure 6.11 shows the same kind of plots for the combination of  $\sqrt{s} = 7$  and

$\sqrt{s} = 8$  TeV results for the events that belong to Cat.1 (top) and Cat.2 (bottom) respectively.

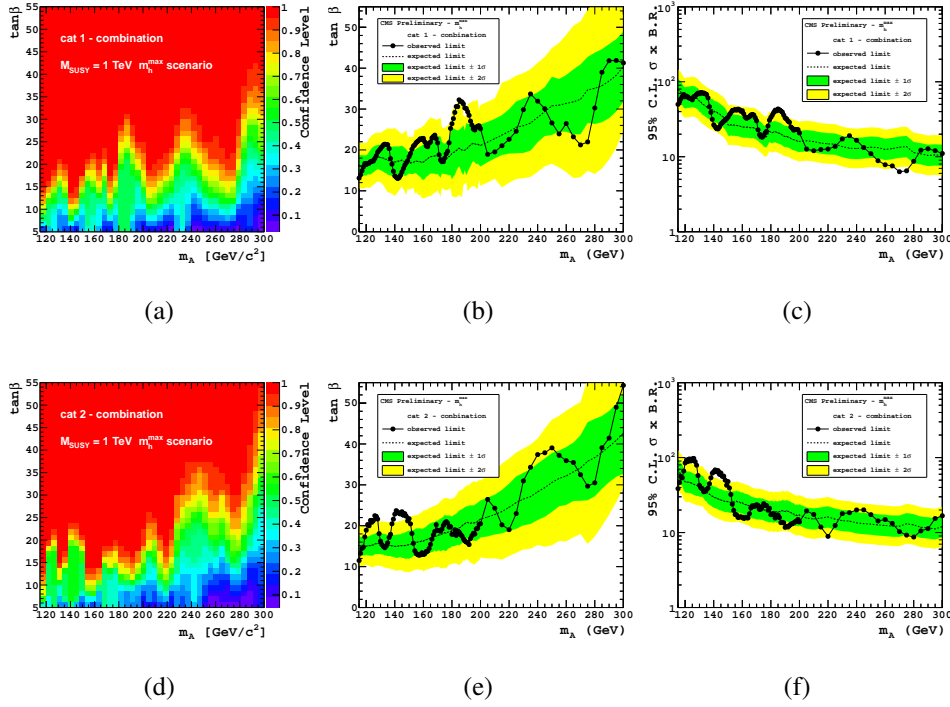
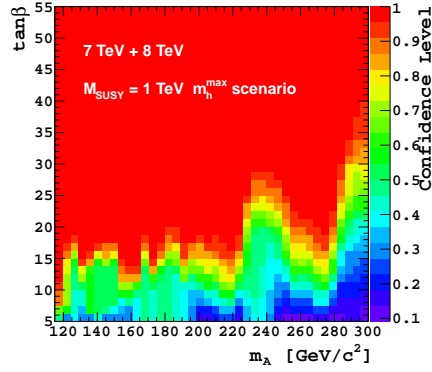


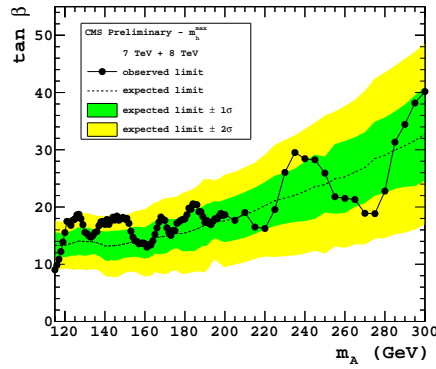
Figure 6.11: Results obtained combining the two centre-of-mass data for Cat.1 (a, b, c) and Cat.2 (d, e, f): CL of the exclusion limit as function of  $m_A$  and  $\tan\beta$  (a, d); exclusion limit on  $\tan\beta$  as function of  $m_A$  (b, e) and 95% CL of the limit on  $\sigma \times BR$  (fb) as a function of  $m_A$  (c, f).

In the end, figure 6.12 shows the results for the full combination of  $\sqrt{s} = 7$  and  $\sqrt{s} = 8$  TeV summing the two event categories.

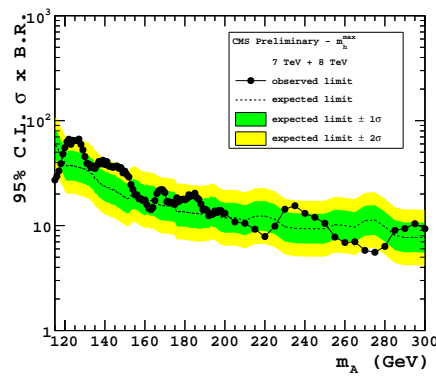
The plots (a, b) shown the results obtained point by point in the analysed part of the MSSM free parameter space. In order to summarize this detailed outcome, values of  $\tan\beta$  larger than 15 in the  $m_A$  range 115-200 GeV are excluded, as also are values of  $\tan\beta$  greater than 30 in the  $m_A$  range up to 300 GeV. The same range of values is reported in the plot (c) but in terms of cross section times branching ratio.



(a)



(b)



(c)

Figure 6.12: Results of the full combination of the data collected at  $\sqrt{s} = 7$  and  $\sqrt{s} = 8$  TeV summing Cat.1 and Cat.2: CL of the exclusion limit in the  $(m_A, \tan \beta)$  (a), 95% CL upper limit of  $\tan \beta$  as a function of  $m_A$  (b), and 95% CL limit on  $\sigma \times BR$  (fb) as a function of  $m_A$  (c).

### 6.5.2 Combined results within $m_h^{\text{mod}}$ scenarios

Concerning the results for the  $m_h^{\text{mod}+}$  and  $m_h^{\text{mod}-}$  scenarios, just the full combined measurements are presented. These results are obtained exploiting the same efficiencies, scale factors and systematic uncertainties used to compute results within the  $m_h^{\text{max}}$  scenario, but using the appropriate cross sections and decay branching ratios predicted for the MSSM modified scenarios.

The plots in the left part of Fig. 6.13 are relative to the  $m_h^{\text{mod}+}$  scenario, while the ones in the right part are relative to  $m_h^{\text{mod}-}$ . For both cases the CL of the exclusion limit in the  $(m_A, \tan\beta)$  plane (a,b), the 95% CL exclusion limit of  $\tan\beta$  as a function of  $m_A$  (c,d), and the 95% CL limit on the cross section times the decay branching ratio as a function of  $m_A$  (e,f). The results of both the modified scenario are very similar between them, as also with respect to the  $m_h^{\text{max}}$ . This was expected since the changes of Higgs cross sections, masses and widths in the three scenarios are very small.

## 6.6 Checks on the fit procedure

In order to check the goodness of the chosen fit function, further studies have been performed.

First, the entire fitting procedure, described in the previous paragraphs, has been applied to MC events simulated in collisions at  $\sqrt{s} = 7$  TeV. In this test not only the signal but also the background is taken from simulation. The invariant mass distributions, obtained after the event selection of the samples listed in Tab.5.4, are: weighted to correct for the data-MC discrepancy; summed according to the cross section of each process; and properly scaled according to the integrated luminosity of the real data collected at  $\sqrt{s} = 7$  TeV.

Final results are calculated: Fig. 6.14 shows the CL of the exclusion limit in the  $(m_A, \tan\beta)$  plane for simulated events at  $\sqrt{s} = 7$  TeV that belong to Cat.1 and Cat.2. Similarly the 95% CL exclusion limit in the  $(m_A, \tan\beta)$  plane is reported in Fig. 6.15. The results obtained using the MC background samples are consistent with the results obtained using the real data within two standard deviations. The fluctuations do not manifest systematic deviations as a function of  $m_A$ .

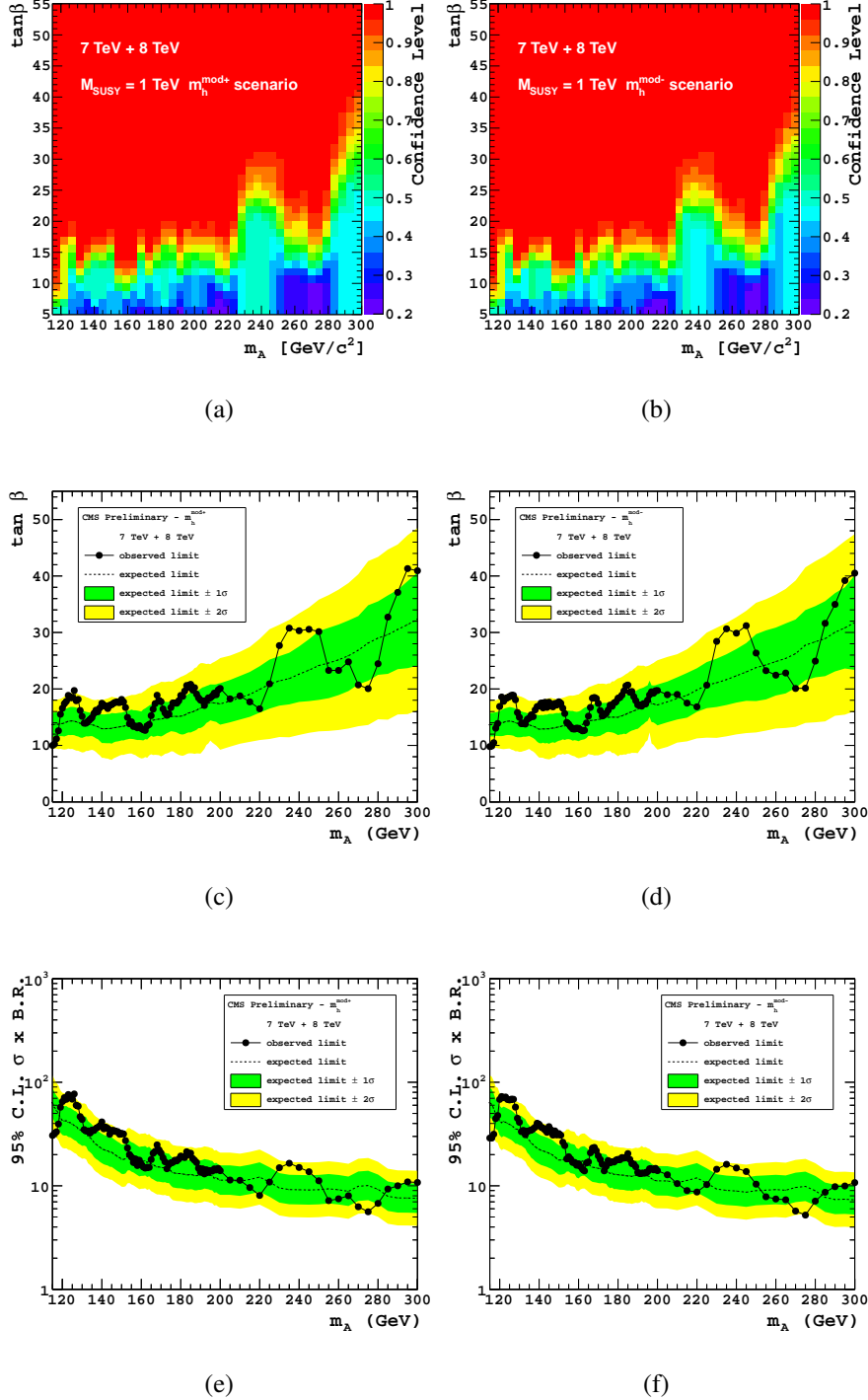


Figure 6.13: Results of the combination of the data collected at  $\sqrt{s} = 7 \text{ TeV}$  and  $\sqrt{s} = 8 \text{ TeV}$  summing Cat.1 and Cat.2 for the  $m_h^{\text{mod}+}$  scenario (a,c,e) and the  $m_h^{\text{mod}-}$  (b,d,f): CL of the exclusion limit in the  $(m_A, \tan\beta)$  plane (a,b), 95% CL excluded values of  $\tan\beta$  as a function of  $m_A$  (c,d) and 95% CL limit on  $\sigma \times BR$  (fb) as a function of  $m_A$  (e,f).

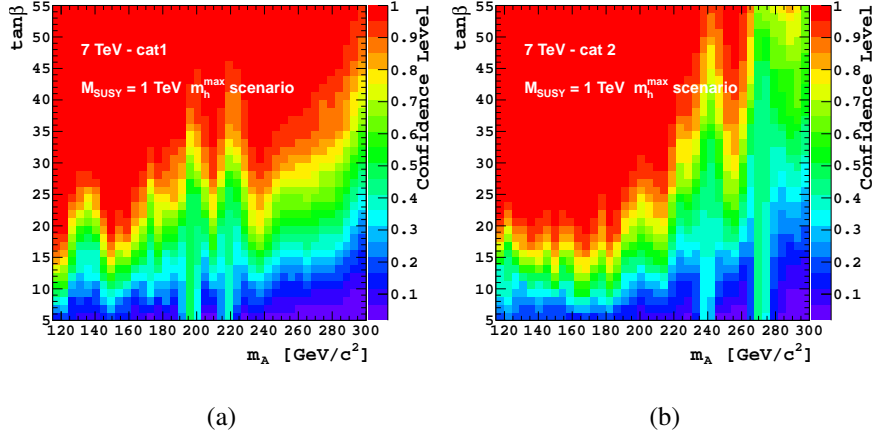


Figure 6.14: The CL of the exclusion limit in the  $(m_A, \tan \beta)$  plane for Cat.1 (left) and Cat.2 (right), for MC simulated events at  $\sqrt{s} = 7$  TeV. In this case the background is taken from simulated samples.

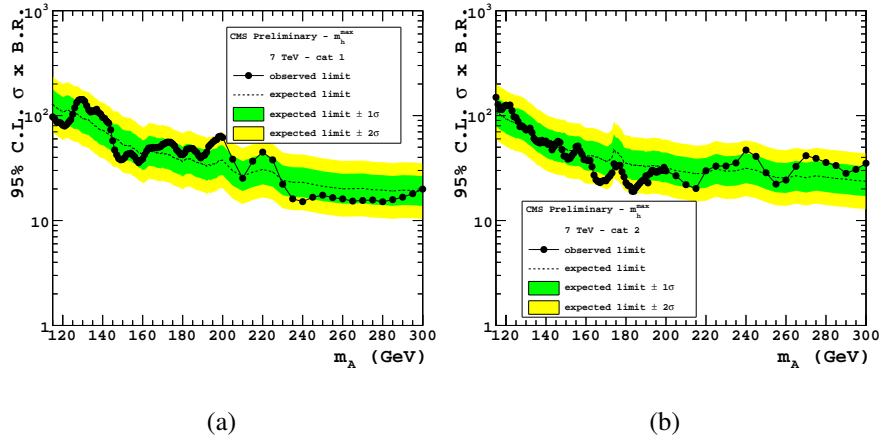


Figure 6.15: The 95 % CL limit on  $\sigma \times BR$  (fb) as a function of  $m_A$  obtained from MC simulated events of Cat.1 (left) and Cat.2 (right), for the case  $\sqrt{s} = 7$  TeV. In this case the background is taken from simulated samples.

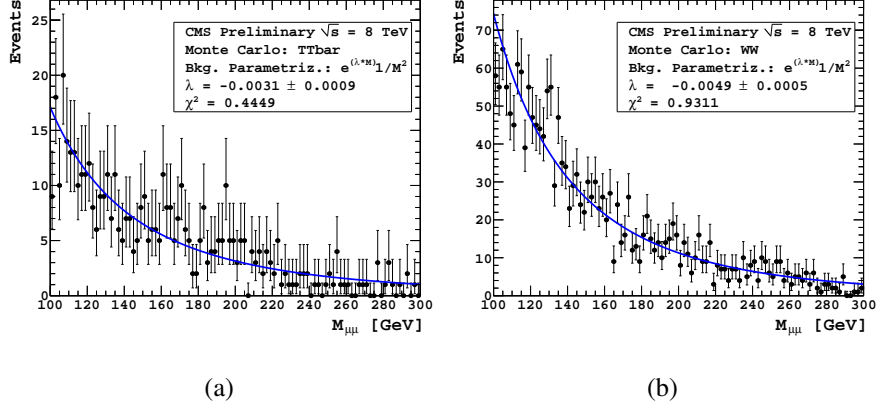


Figure 6.16: Fit to the  $t\bar{t}$  (a) and  $W^\pm W^\pm$  (b) components of the background obtained from simulation. The fit is performed dropping the Drell-Yan description in the function that describes the background.

A second test concerns the choice of the parametrization of the background shape, as expressed by formula 6.6. This is motivated by the large amount of Drell-Yan events in the data, which should be well described by the tail of the Breit-Wigner function. Therefore a test on simulated events has been performed to determine how the *non Drell-Yan* part of the function still reproduces the  $t\bar{t}$  and  $W^\pm W^\pm$  background components. When the Drell-Yan description is dropped in the background function the formula 6.6 becomes

$$F_{bkg} = N \cdot e^{\lambda x} \cdot \frac{1}{x^2} \quad (6.9)$$

The modified expression of  $F_{bkg}$ , where only  $\lambda$  parameter is free to vary, is used to fit the  $t\bar{t}$ , Fig. 6.16(a), and the  $W^\pm W^\pm$ , Fig. 6.16 (b), invariant mass distributions. Both figures show that the *non Drell-Yan* components of the background are properly described by the *non Drell-Yan* part of  $F_{bkg}$  function (eq.6.9).

A further check is performed by injecting in the data sample at  $\sqrt{s} = 8$  TeV an artificial signal, to test the capability of the analysis to detect it. This is done taking the h, H and A boson samples in two cases: one for  $m_A = 150$  GeV,  $\tan \beta = 30$  and the other for  $m_A = 125$  GeV,  $\tan \beta = 15$ . The cross sections predicted by the MSSM  $m_h^{\max}$  scenario are used to properly add the signal to data. Figure 6.17 shows the fit in both cases when the signal is injected in data, for

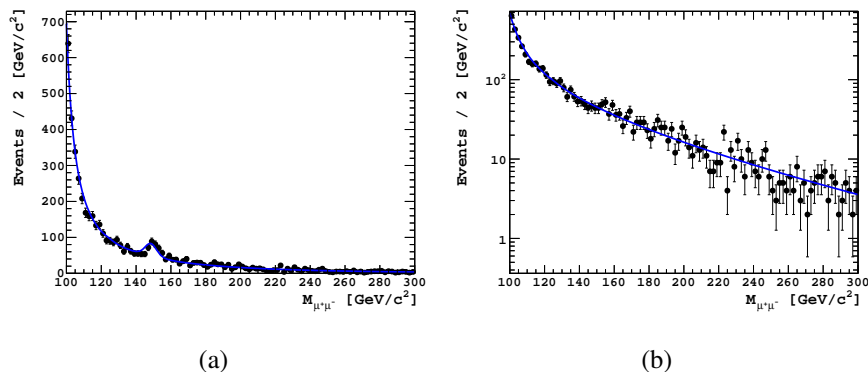
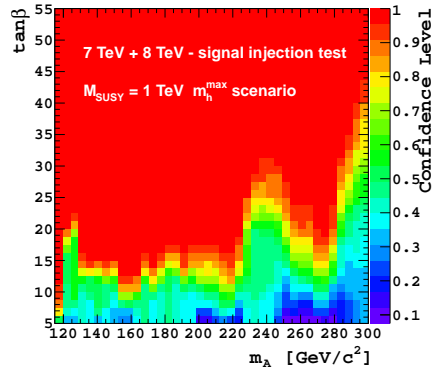


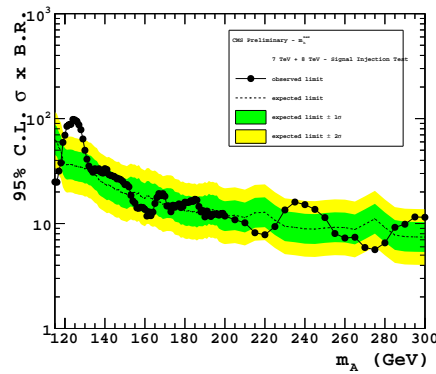
Figure 6.17: Fit to the data that belong to Cat.1 at  $\sqrt{s} = 8$  TeV when a simulated signal is injected in the sample. In a) the signal corresponds to the MSSM expectations for  $m_A = 150$  GeV and  $\tan \beta = 30$ , whereas in b) it is for  $m_A = 125$  GeV and  $\tan \beta = 15$ .

events that belong to Cat.1 at  $\sqrt{s} = 8$  TeV: in the first case (a) the signal cross section is high enough to make it clearly visible above the background, whereas in the second case (b) it is much weaker.

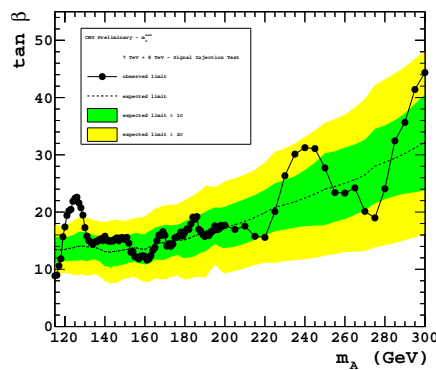
Results of the limit computation are shown in Fig. 6.6 just for the second case: the CL in the  $(m_A, \tan \beta)$  plane (a), the 95% CL limit on the cross section times the decay branching ratio (b), and the exclusion limit in the  $(m_A, \tan \beta)$  plane (c). Although the signal peak is practically invisible by eye in Fig. 6.17 (b), the fit procedure detects it as an excess over the background expectation of  $\approx 3\sigma$ .



(a)



(b)



(c)

Figure 6.18: Results of the data collected at  $\sqrt{s} = 8 \text{ TeV}$  when the MSSM Higgs signal at  $m_A = 125 \text{ GeV}$  and  $\tan \beta = 15$  is added. The CL is in the  $(m_A, \tan \beta)$  plane (a), the 95% CL limit on  $\sigma \times BR$  (fb) (b), and the 95% CL limit in the  $(m_A, \tan \beta)$  plane (c), where the presence of the injected signal is visible above the expected background.

## 6.7 Comparison with published results

The results presented in this thesis improve the limits found in previous  $\Phi \rightarrow \mu^+ \mu^-$  analyses performed by CMS [101] on  $5 \text{ fb}^{-1}$  of data collected in 2011 in p-p collision at  $\sqrt{s} = 7 \text{ TeV}$ , and ATLAS [102] on  $4.7 \text{ fb}^{-1}$  of data taken in the same period. This is because the larger statistics collected at higher center-of-mass-energy, allows more stringent limits to be set. Both the analyses interpret the data only within the  $m_h^{\text{max}}$  scenario.

The results published by the CMS collaboration are shown in Fig.6.19. These have been obtained within the  $m_h^{\text{max}}$  scenario, using a different data categorization with respect to the one described in sec.(5.2.6), but they are compatible with the results obtained in this thesis just for the part of 2011 data (Fig.6.10).

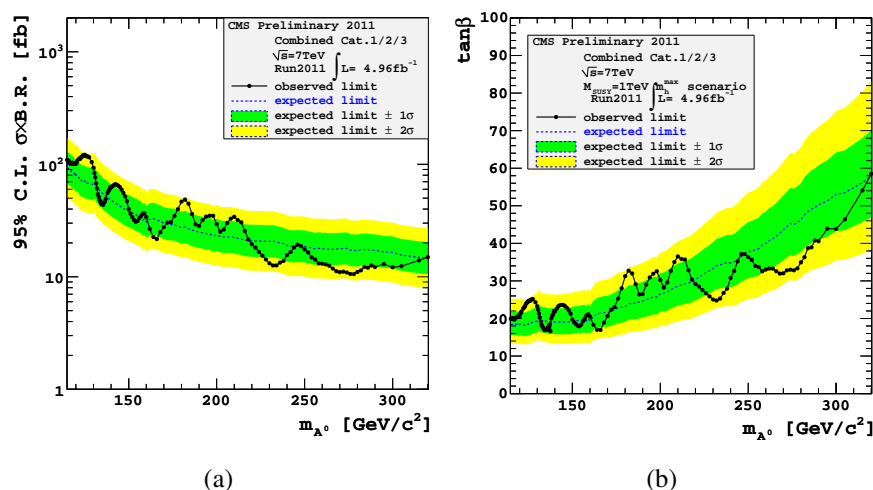


Figure 6.19: Results taken from [101]: combined exclusion limit for the MSSM  $\sigma \times \text{BR}$  (fb) at 95% CL (a) and its projection in the  $(m_A, \tan\beta)$  plane (b). The excluded regions are above the curves.

The results published by the ATLAS collaboration are shown in Fig.6.20, where curves relative to the  $\tau^+ \tau^-$  and the  $\mu^+ \mu^-$  results are superimposed. These have been obtained within the  $m_h^{\text{max}}$  scenario. Concerning the search in the dimuon final state, the same data categorization as the one described in sec.5.2.6 is used. The scan of  $(m_A, \tan\beta)$  plane is done with a larger granularity, given the worse dimuon channel resolution of the ATLAS detector. Anyway the results, displayed

separately for the two categories, are compatible with the ones obtained in this thesis (Fig.6.9). Neutral MSSM Higgs in  $\tau^+\tau^-$  decays has been also studied at

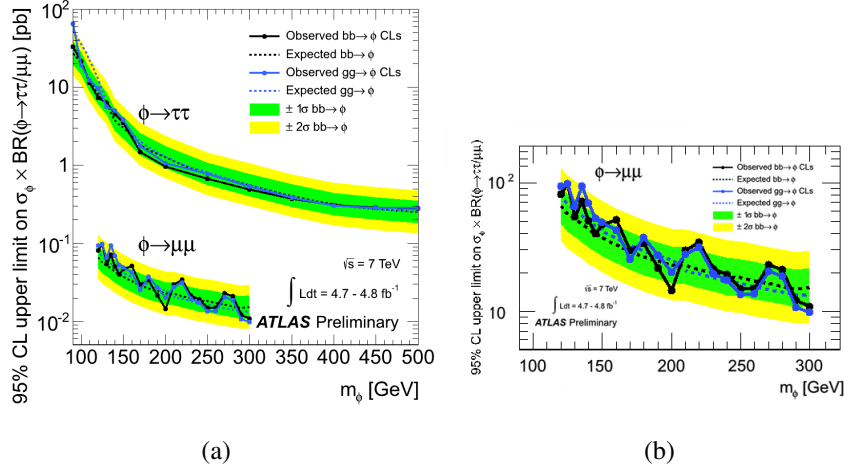


Figure 6.20: Results taken from [102]: in the plot (a) expected (dashed line) and observed (solid line) 95% CL limits on the cross section of gluon-fusion and b-associated production times decay branching ratio into  $\tau$  and  $\mu$  pairs, respectively, along with the  $\pm 1\sigma$  and  $\pm 2\sigma$  bands for the expected limit. The difference in the exclusion limits obtained for the gluon-fusion and the b-associated production modes is due to the different sensitivity from the b-tagged samples. The plot (b) reports an excerpt from (a) for the  $\mu\mu$  channel curves, where the scale on the y-axis is in the units (fb) used in this thesis.

CMS on the full data collected in 2011 and 2012. These results have also been non conclusive, but have set the most restrictive limit [103], thanks to higher decay branching ratio, which allows to reach a higher sensitivity. Although the  $\tau^+\tau^-$  is expected to be the discovery channel, only with the  $\mu^+\mu^-$  a resolution needed to measure the  $\tan\beta$  parameter can be reached.

The MSSM  $\Phi \rightarrow b\bar{b}$  has been also studied at CMS [104] only on the 2011 data collected at CMS in p-p collision at  $\sqrt{s} = 7$  TeV. Despite its highest branching ratio (90%), the sensitivity reached in this case is similar to the one of the  $\mu^+\mu^-$  channel, since the full-hadronic final state is very difficult to separate from the QCD background. Anyway the interest in this channel is to study the MSSM Higgs coupling to the b-quark.



# Conclusions

This Ph.D thesis describes the search for the neutral MSSM Higgs bosons A, h and H decaying to  $\mu^+\mu^-$  with the CMS detector, where the Higgs are produced in association with a  $b\bar{b}$ -pair or by the gluon-gluon fusion process. These are the processes with the highest cross section for a neutral MSSM Higgs at LHC.

The study of MSSM parameter space is conducted in the framework of the most conservative benchmark scenario,  $m_h^{max}$ , and its modified versions  $m_h^{mod+}$  and  $m_h^{mod-}$ , which are developed to account for the SM Higgs discovery with a mass of about 126 GeV. A scan of the  $m_A - \tan\beta$  plane is done in the  $\tan\beta$  range 5-55 for  $\tan\beta$  and  $m_A$  115-300 GeV.

The search is performed on the data collected at CMS in LHC p-p collisions at  $\sqrt{s} = 7$  TeV and  $\sqrt{s} = 8$  TeV, corresponding to an integrated luminosity of  $5.1 \text{ fb}^{-1}$  and  $19.4 \text{ fb}^{-1}$  respectively. Simulated samples are used only to study the signal, since the background is estimated entirely from the data.

As expected the main source of background arises from dimuon pairs produced in Drell-Yan processes and  $t\bar{t}$  decays. From the first comes the irreducible background characteristic of this analysis, constituted by the  $b\bar{b}Z$  events, while we are able to suppress events of type  $q\bar{q}Z$  (where  $q = u, d, s, c$ ) and also events from semileptonic decays of t-quark.

The dimuon final state has a very clean signature, and it has been easy to detect thanks to the excellent muon identification of CMS detector. The main focus of this analysis has been to reach a high sensitivity, given the very low branching ratio of this channel. This has been achieved performing on the selected dimuon events with low missing energy (to reduce the  $t\bar{t}$  background), a categorization based on the presence or the absence of a jet coming from b-quark. This enhances the signal sensitivity in case of b-associated production and gluon fusion respectively.

The statistical treatment of the data has been performed separately for each

category. No signal evidence has been found in both categories, and their results are combined to give the exclusion limits in the  $m_A$ - $\tan \beta$  plane.

Values of  $\tan \beta$  larger than 15 in the  $m_A$  range 115-200 GeV are excluded, as also are values of  $\tan \beta$  greater than 30 in the  $m_A$  range up to 300 GeV. There are no significant differences in the results obtained within the three different scenarios considered.

These results improve the limits found in previous searches for  $\Phi \rightarrow \mu^+ \mu^-$  performed by the CMS and the ATLAS collaborations on 2011 data, given the larger statistics collected at higher center-of-mass-energy allows more stringent limits to be set. Anyway the neutral MSSM Higgs discovery channel is the  $\tau^+ \tau^-$ , whose results have also been non conclusive, but have set a much more restrictive limit.

The LHC schedule plans to start the data-taking in 2015 with a center-of-mass-energy of about 13 or 14 GeV, and an instantaneous luminosity of  $1 \cdot 10^{34} \text{ cm}^{-2} \text{ s}^{-1}$ . If the plans will be confirmed, the same amount of statistics accumulated so far, will be collected in about a month of LHC run. This will allow to explore more accurately the MSSM parameter space, and in absence of MSSM Higgs discovery, to put more restrictive limits, and perhaps to completely exclude the model.

In case of Higgs discovery the  $\mu\mu$  channel, which is the only that fully reconstructs the final state, will make it possible the precision measurements, which in particular at CMS benefit of the high muon momentum resolution.

# Bibliography

- [1] C. Quigg B. W. Lee and H. B. Thacker. Weak interactions at very high energies: The role of the higgs boson mass. *Phys. Rev. D*, 16:1519–1531, 1977. <http://link.aps.org/doi/10.1103/PhysRevD.16.1519>.
- [2] J. Espinosa J. Casas and M. Quiros. Standard model stability bounds for new physics within lhc reach. *Phys.Lett.*, B382:374–382(hep-ph/9603227), 1996.
- [3] T. Hambye and K. Riesselmann. Matching conditions and higgs mass upper bounds revisited. *Phys.Rev.*, 1997. hep-ph/9610272.
- [4] J. Beringer et al. (Particle Data Group). 2012 review of particle physics and 2013 partial update for the 2014 edition. *Phys. Rev. D86, 010001 (2012)*, 2012.
- [5] L3 OPAL Collaborations ALEPH, DELPHI and LEP Working Group ifor Higgs Boson Searches. Search for the standard model higgs boson at lep. *Phys. Lett. B*, 565, 6, 2003.
- [6] T. Aaltonen et al. Combination of Tevatron searches for the standard model Higgs boson in the  $W^+W^-$  decay mode. *Phys.Rev.Lett.*, 104:061802, 2010.
- [7] D0 Collaboration CDF Collaboration and Higgs Working Group Tevatron New Physics. Updated combination of cdf and d0 searches for standard model higgs boson production with up to  $10.0 \text{ fb}^{-1}$  of data. <http://arxiv.org/abs/1207.0449>, 2012.

## BIBLIOGRAPHY

---

- [8] Georges Aad et al. Combined search for the Standard Model Higgs boson in  $pp$  collisions at  $\sqrt{s} = 7$  TeV with the ATLAS detector. *Phys.Rev.*, D86:032003, 2012.
- [9] Serguei Chatrchyan et al. Combined results of searches for the standard model Higgs boson in  $pp$  collisions at  $\sqrt{s} = 7$  TeV. *Phys.Lett.*, B710:26–48, 2012.
- [10] CDF and D0 Collaborations. Evidence for a particle produced in association with weak bosons and decaying to a bottom-antibottom quark pair in higgs boson searches at the tevatron. *Phys. Rev. Lett.*, 109, 2012.
- [11] Serguei Chatrchyan et al. Observation of a new boson with mass near 125 GeV in  $pp$  collisions at  $\sqrt{s} = 7$  and 8 TeV. *JHEP*, 1306:081, 2013.
- [12] LHC Higgs Cross Section Working Group. <https://twiki.cern.ch/twiki/bin/view/lhcphysics/crosssections>. *LHC Twiki*, 2013.
- [13] L. D. Landau. The moment of a 2-photon system. *Dokl. Akad. Nauk*, 60, 1948.
- [14] C. N. Yang. Selection rules for the dematerialization of a particle into two photons. *Phys. Rev.*, 77, 1950.
- [15] Serguei Chatrchyan et al. Search for neutral Higgs bosons decaying to  $\tau$  pairs in  $pp$  collisions at  $\sqrt{s} = 7$  TeV. *Phys.Lett.*, B713:68–90, 2012.
- [16] P.W. Higgs. Broken symmetries and the masses of gauge bosons. *Phys. Rev. Lett.*, 1964.
- [17] H.P. Nilles. Supersymmetry, supergravity and particle physics. *Phys. Reports*, 1984.
- [18] R. Arnowitt P. Nath and A.H. Chamseddine. *SuperGravity*. World Scientific, Singapore, 1984.
- [19] S.P. Martin. In perspectives on supersymmetry 2. *Applied N = 1*, 1984.

- [20] S. Weinberg. *The Quantum Theory of Fields, Volume III: Supersymmetry*. Cambridge University Press, Cambridge, 200.
- [21] L. Girardello and Marcus T. Grisaru. Soft Breaking of Supersymmetry. *Nucl.Phys.*, B194:65, 1982.
- [22] L.J. Hall and Lisa Randall. Weak scale effective supersymmetry. *Phys.Rev.Lett.*, 65:2939–2942, 1990.
- [23] Edward Witten. Dynamical Breaking of Supersymmetry. *Nucl.Phys.*, B188:513, 1981.
- [24] Savas Dimopoulos and Howard Georgi. Softly Broken Supersymmetry and SU(5). *Nucl.Phys.*, B193:150, 1981.
- [25] N. Sakai. Naturalness in Supersymmetric Guts. *Z.Phys.*, C11:153, 1981.
- [26] Leonard Susskind. The gauge hierarchy problem, technicolor, supersymmetry, and all that. (talk). *Phys.Rept.*, 104:181–193, 1984.
- [27] Frank Daniel Steffen. Dark Matter Candidates - Axions, Neutralinos, Gravitinos, and Axinos. *Eur.Phys.J.*, C59:557–588, 2009.
- [28] Howard E. Haber and Gordon L. Kane. The Search for Supersymmetry: Probing Physics Beyond the Standard Model. *Phys.Rept.*, 117:75–263, 1985.
- [29] R. Godbole M. Drees and P. Roy. Theory and phenomenology of sparticles. *World Scientific*, 2005.
- [30] Glennys R. Farrar and Pierre Fayet. Phenomenology of the Production, Decay, and Detection of New Hadronic States Associated with Supersymmetry. *Phys.Lett.*, B76:575–579, 1978.
- [31] Pierre Fayet. A Gauge Theory of Weak and Electromagnetic Interactions with Spontaneous Parity Breaking. *Nucl.Phys.*, B78:14, 1974.
- [32] Kenzo Inoue, Akira Kakuto, Hiromasa Komatsu, and Seiichiro Takeshita. Low-Energy Parameters and Particle Masses in a Supersymmetric Grand Unified Model. *Prog.Theor.Phys.*, 67:1889, 1982.

## BIBLIOGRAPHY

---

- [33] J.F. Gunion and Howard E. Haber. Higgs Bosons in Supersymmetric Models. 1. *Nucl.Phys.*, B272:1, 1986.
- [34] CERN. LHC design report. Technical report, 2004.
- [35] *LEP design report*. CERN, Geneva, 1984. Copies shelved as reports in LEP, PS and SPS libraries.
- [36] The TOTEM Collaboration. The totem experiment at the cern large hadron collider. *Journal of Instrumentation*, 3(08):S08007, 2008.
- [37] The TOTEM Collaboration. Luminosity-independent measurements of total, elastic and inelastic cross-sections at  $\sqrt{s} = 7$  TeV. Technical Report TOTEM-2012-004. CERN-PH-EP-2012-353, CERN, Geneva, Nov 2012.
- [38] The TOTEM Collaboration. Luminosity-independent measurement of the proton-proton total cross section at  $\sqrt{s} = 8$  TeV. *Phys. Rev. Lett.*, 111:012001, Jul 2013.
- [39] Eck et Al. *LHC computing Grid: Technical Design Report. Version 1.06 (20 Jun 2005)*. Technical Design Report LCG. CERN, Geneva, 2005.
- [40] Ludmila Cherkasova, Diwaker Gupta, Eygene Ryabinkin, Roman Kurakin, Vladimir Dobretsov, and Amin Vahdat. Optimizing Grid Site Manager Performance with Virtual Machines. In *Proceedings of the 3rd USENIX Workshop on Real Large Distributed Systems*, December 2006.
- [41] CMS Collaboration. The CMS experiment at the CERN LHC. *JINST*, 0803:S08004, 2008.
- [42] Aaron Dominguez. The cms pixel detector. Technical Report CMS-CR-2009-142. CERN-CMS-CR-2009-142, CERN, Geneva, Jun 2009.
- [43] R Bruneliere. Cms electromagnetic calorimeter performance and test beam results. *Nucl. Instrum. Methods Phys. Res., A*, 572(1):33–35, 2007.
- [44] UK. Cobham, Vector Fields Ltd. Tosca software. <http://www.vectorfields.com>.

- [45] The CMS Collaboration. The muon project: Technical design report. *CERN/LHCC 97-32*, 1997.
- [46] The CMS Collaboration. The tridas project technical design report, volume 1: The trigger systems. *CERN/LHCC 2000-038*, CMS TDR 6.1, 2000.
- [47] The CMS Collaboration. The tridas project technical design report, volume 2: Data acquisition and high-level trigger. *CERN/LHCC 2002- 26*, CMS TDR 6.2, 2002.
- [48] CMS Collaboration. The cms software framework cmssw. <http://cmsdoc.cern.ch/cms/cpt/Software/html/General/>.
- [49] J. Pumplin et al. New generation of parton distributions with uncertainties from global QCD analysis. *JHEP*, 07:12, 2002.
- [50] T. T.Sjostrand, S. Mrenna, and P.Z. Skands. Pythia 6.4 physics and manual. *JHEP*, 05:026, 2006.
- [51] D.J. Lange. The `evtgen` particle decay simulation package. *Nucl. Instrum. Meth.*, A462:152–155, 2001.
- [52] S. Frixione, P. Nason, and C. Oleari. Matching nlo qcd computations with parton shower simulations: the powheg method. 2007.
- [53] T. Stelzer and W.F. Long. Automatic generation of tree level helicity amplitudes. *Comput.Phys.Commun.*, 81:357–371, 1994.
- [54] S. Agostinelli et al. GEANT4: A simulation toolkit. *Nucl. Instrum. Meth.*, A506:250., 2003.
- [55] John Allison et al. GEANT4 developments and applications. *IEEE Trans. Nucl. Sci.*, 53:270, 2006.
- [56] W. Adam et al. Description and performance of the cms track and primary vertex reconstruction. CMS AN-11-172, 2011.
- [57] Susanna Cucciarelli, Marcin Konecki, Danek Kotlinski, and Teddy Todorov. Track reconstruction, primary vertex finding and seed generation

## BIBLIOGRAPHY

---

- with the pixel detector. Technical Report CERN-CMS-NOTE-2006-026, CERN, Geneva, Jan 2006.
- [58] M. Pioppi. Iterative Tracking. *CMS Internal Note*, 2007/065, 2008.
- [59] R. Fruhwirth. Application of Kalman filtering to track and vertex fitting. *Nucl.Instrum.Meth.*, A262:444–450, 1987.
- [60] Thomas Speer, Kirill Prokofiev, R Fruhwirth, Wolfgang Waltenberger, and Pascal Vanlaer. Vertex fitting in the cms tracker. *CMS NOTE*, 2006/032, 2006.
- [61] W. Erdmann. Offline Primary Vertex Reconstruction with Deterministic Annealing Clustering. *CMS Analysis Note*, 2011/014, 2011. [http://cms.cern.ch/icMS/jsp/openfile.jsp?type=IN&year=2008&files=IN2011\\_014.pdf](http://cms.cern.ch/icMS/jsp/openfile.jsp?type=IN&year=2008&files=IN2011_014.pdf).
- [62] Rose K. Deterministic Annealing for Clustering, Compression, Classification, Regression and related Optimisation Problems. *Proceedings of the IEEE*, Vol. 86, Issue 11, 1998.
- [63] R Fruhwirth, Wolfgang Waltenberger, and Pascal Vanlaer. Adaptive vertex fitting. *CMS NOTE*, 2007/008, 2007. <https://cdsweb.cern.ch/record/1027031>.
- [64] Ting Miao, N Leioatts, Hans Wenzel, and Francisco Yumiceva. Beam position determination using tracks. *CMS NOTE*, 2007/021, 2007. <https://cdsweb.cern.ch/record/1061285>.
- [65] Serguei et al Chatrchyan. Performance of CMS Muon Reconstruction in Cosmic-Ray Events. *JINST*, 5:T03022, 2010.
- [66] CMS Collaboration. Cms physics tdr: Volume 1, detector performance and software. *CERN/LHCC 2006-001*, 2006.
- [67] Daniele Trocino. *Muon Reconstruction and Momentum Scale Calibration and Their Application to Standard Model Higgs Searches with the CMS Experiment*. PhD thesis, Università degli Studi di Torino, 2010.

- [68] S. Chatrchyan et al. Performance of the cms drift tube chambers with cosmic rays. *JINST*, 5:T03015, 2010.
- [69] S. Chatrchyan et al. Performance of the cms chatode strip chambers with cosmic rays. *JINST*, 5:T03018, 2010.
- [70] S. Chatrchyan et al. Performance study of the cms barrel resistive plate chambers with cosmic rays. *JINST*, 5:T03017, 2010.
- [71] Matteo Cacciari, Gavin P. Salam, and Gregory Soyez. The Anti-k(t) jet clustering algorithm. *JHEP*, 0804:063, 2008.
- [72] CMS Collaboration. Particle-Flow Event Reconstruction in CMS and Performance for Jets, Taus, and MET. 2009. CMS-PAS-PFT-09-001.
- [73] CMS Collaboration. Commissioning of the Particle-Flow reconstruction in Minimum-Bias and Jet Events from pp Collisions at 7 TeV. 2010. CMS-PAS-PFT-10-002.
- [74] R. Adolphi et al. The CMS experiment at the CERN LHC. *JINST*, 3:S08004, 2008.
- [75] E. James et al. Muon identification in cms. *CMS NOTE*, 2006/010, 2006. <https://cdsweb.cern.ch/record/927395>.
- [76] CMS Collaboration. Particle-flow commissioning with muons and electrons from J/Psi and W events at 7 TeV. 2010. CMS-PAS-PFT-10-003.
- [77] CMS Collaboration. Commissioning of the Particle-flow Event Reconstruction with the first LHC collisions recorded in the CMS detector. Technical report, 2010. CMS-PAS-PFT-10-001.
- [78] W Adam, R Frühwirth, A Strandlie, and T Todorov. Reconstruction of Electron Tracks With the Gaussian-Sum Filter. Technical report, CERN, Geneva, Mar 2003. CMS-RN-2003-001.
- [79] CMS Collaboration. Particle-Flow Event Reconstruction in CMS and Performance for Jets, Taus, and MET. Technical report, CERN, 2009. Geneva, Apr 2009. CMS-PAS-PFT-09-001.

## BIBLIOGRAPHY

---

- [80] CMS Collaboration. b-Jet Identification in the CMS Experiment. Technical report, 2012. CMS-PAS-BTV-11-004.
- [81] Marcela S. Carena, S. Heinemeyer, C.E.M. Wagner, and G. Weiglein. Suggestions for benchmark scenarios for MSSM Higgs boson searches at hadron colliders. *Eur.Phys.J.*, C26:601–607, 2003.
- [82] Edward Boos, Abdelhak Djouadi, and Alexander Nikitenko. Detection of the neutral MSSM Higgs bosons in the intense coupling regime at the LHC. *Phys.Lett.*, B578:384–393, 2004.
- [83] M. Carena, S. Heinemeyer, O. Stal, C.E.M. Wagner, and G. Weiglein. MSSM Higgs Boson Searches at the LHC: Benchmark Scenarios after the Discovery of a Higgs-like Particle. 2013.
- [84] S. Heinemeyer, W. Hollik, and G. Weiglein. Constraints on tan Beta in the MSSM from the upper bound on the mass of the lightest Higgs boson. *JHEP*, 0006:009, 2000.
- [85] S. Heinemeyer, W. Hollik, and G. Weiglein. FeynHiggs: A Program for the calculation of the masses of the neutral CP even Higgs bosons in the MSSM. *Comput.Phys.Commun.*, 124:76–89, 2000.
- [86] T. Hahn, S. Heinemeyer, W. Hollik, H. Rzehak, and G. Weiglein. FeynHiggs: A program for the calculation of MSSM Higgs-boson observables - Version 2.6.5. *Comput.Phys.Commun.*, 180:1426–1427, 2009.
- [87] CMS Collaboration. 2012 pileup information. Technical report. <https://twiki.cern.ch/twiki/bin/viewauth/CMS/PdmVPileUpDescription>.
- [88] Robert V. Harlander and William B. Kilgore. Higgs boson production in bottom quark fusion at next-to-next-to leading order. *Phys.Rev.*, D68:013001, 2003.
- [89] T. Gehrmann. Tools for NNLO QCD Calculations. *eConf*, C0705302:LOOP05, 2007.

- [90] CMS Collaboration. Pileup reweighting utilities. <https://twiki.cern.ch/twiki/bin/viewauth/CMS/PileupMCReweightingUtilities>.
- [91] CMS Collaboration. Commissioning of the Particle-Flow reconstruction in Minimum-Bias and Jet Events from pp Collisions at 7 TeV. Technical report, 2010. CMS-PAS-PFT-10-002.
- [92] CMS Collaboration. Muscfit: muon momentum scale calibration and momentum resolution fit. Technical report. <https://twiki.cern.ch/twiki/bin/view/CMS/MuonScaleCalib>.
- [93] Matteo Cacciari, Gavin P. Salam, and Gregory Soyez. The Anti-k(t) jet clustering algorithm. *JHEP*, 0804:063, 2008.
- [94] CMS Collaboration. Jet identification in high pile-up environment. Technical report. <https://twiki.cern.ch/twiki/bin/viewauth/CMS/PileupJetID>.
- [95] CMS Collaboration. Reference muon id and isolation efficiencies. <https://twiki.cern.ch/twiki/bin/view/CMS/MuonReferenceEffs>.
- [96] CMS Collaboration. 2012 data and MC (moriond 2013 prescription). Technical report. [https://twiki.cern.ch/twiki/bin/viewauth/CMS/BtagPOG?skin=drupal#2012\\_Data\\_and\\_MC\\_Moriond13\\_presc](https://twiki.cern.ch/twiki/bin/viewauth/CMS/BtagPOG?skin=drupal#2012_Data_and_MC_Moriond13_presc).
- [97] CMS Collaboration. Jet Performance in pp Collisions at 7 TeV. Technical report, 2010. CMS-PAS-JME-10-003.
- [98] CMS Collaboration. CMS luminosity based on pixel cluster counting: Summer 2012 update. CMS Physics Analysis Summary CMS-PAS-LUM-12-001, 2012. <http://cdsweb.cern.ch/record/1482193>.
- [99] Michiel Botje, Jon Butterworth, Amanda Cooper-Sarkar, Albert de Roeck, Joel Feltse, et al. The PDF4LHC Working Group Interim Recommendations. Technical report, 2011.

## BIBLIOGRAPHY

---

- [100] Glen Cowan, Kyle Cranmer, Eilam Gross, and Ofer Vitells. Asymptotic formulae for likelihood-based tests of new physics. *Eur.Phys.J.*, C71:1554, 2011.
- [101] Search for Neutral MSSM Higgs Bosons in the  $\mu^+\mu^-$  final state with the CMS experiment in pp Collisions at  $\sqrt{s} = 7$  TeV. Technical Report CMS-PAS-HIG-12-011, CERN, Geneva, 2012.
- [102] Georges Aad et al. Search for the neutral Higgs bosons of the Minimal Supersymmetric Standard Model in  $pp$  collisions at  $\sqrt{s} = 7$  TeV with the ATLAS detector. *JHEP*, 1302:095, 2013.
- [103] Higgs to  $\tau\tau$  (MSSM). Technical Report CMS-PAS-HIG-13-021, CERN, Geneva, 2013.
- [104] Serguei Chatrchyan et al. Search for a Higgs boson decaying into a b-quark pair and produced in association with b quarks in proton-proton collisions at 7 TeV. *Phys.Lett.*, B722:207–232, 2013.